MOTT TRANSITION IN STRONGLY CORRELATED MATERIALS: A REALISTIC MODELING USING LDA+DMFT

BY SAHANA MURTHY

A dissertation submitted to the
Graduate School—New Brunswick
Rutgers, The State University of New Jersey
in partial fulfillment of the requirements
for the degree of
Doctor of Philosophy
Graduate Program in Physics and Astronomy
Written under the direction of
Professor Gabriel Kotliar
and approved by

ABSTRACT OF THE DISSERTATION

Mott transition in strongly correlated materials: a

realistic modeling using LDA+DMFT

by Sahana Murthy

Dissertation Director: Professor Gabriel Kotliar

We study aspects of the Mott metal-insulator transition in simple models and in real

materials. We first investigate the density-driven Mott transition in the degenerate

Hubbard model within the framework of dynamical mean-field theory (DMFT). We

demonstrate the divergence of compressibility near the finite temperature transition

endpoint using quantum Monte Carlo simulations. We show that our results are relevant

to the α - γ transition in Cerium.

In the latter part of the thesis, we use a combination of density functional methods

with local density approximation (LDA) and many body techniques such as DMFT to

realistically model two materials with strong correlations. We compute the band struc-

ture and spectra of $YbRh_2Si_2$ which has an antiferromagnetic ground state. $YbRh_2Si_2$

is known to have a strong anisotropy in its magnetic response with respect to its crys-

tal structure. We determine magnetic anisotropy energy of YbRh₂Si₂ from its total

energy. Using LDA+DMFT methods we calculate the spectra and equilibrium volume

of Americium. We show that on applying pressure, a Mott metal-insulator transition

takes place in Americium which is in accordance with experimental studies.

ii

Acknowledgements

I am grateful to my advisor Gabi Kotliar for guidance during my thesis. Thank you for teaching me good ways of doing research. Special thanks to Sergej Savrasov who has been greatly instrumental in bringing this thesis to a close.

I am very grateful to Viktor Oudovenko who miraculously managed to solve every problem I ran into with my program codes. Thanks to Xi Dai and Harald Jeschke for many useful discussions. I am thankful to R. Chitra and Marcelo Rozenberg who have considerably helped me out of my confusion with physics.

I would like to thank Bob Bartynski, David Harrington, Andy Millis, and Karin Rabe for acting as members of my Ph.D. committee. I would like to thank Jolie Cizewski for her support as graduate director.

Many thanks to my graduate student friends in physics, Carlos Bolech, David Brookes, Marcello Civelli, Andreas Deppeler, Bruno El-Bennich, Masud Haque, Jaewook Joo, Venky Kancharla, Sergei Pankov, Indranil Paul, Nayana Shah, Bala Subramanian and Antonina Toropova for the times spent together, discussing physics, the meaning of life and other eclectic ideas.

To Kathy Dimeo, thank you for taking care of all administrative issues so efficiently that my day-to-day life at Rutgers seemed quite uncomplicated.

I would like to say a special thanks to Baki Brahmia and Peter Lindenfeld for giving me the opportunity to teach physics in a particularly stimulating and enriching setting. Many thanks go to Eugenia Etkina for helping me become a better teacher. To the students, staff and graduate fellows of Bunting-Cobb, my gratitude for providing a wonderful environment at the residence hall. This was what I called home for three years.

To the many friends I made at Rutgers, thanks for making my staying at Rutgers

a pleasant experience.

To Amma, Appa and Sameera, thanks for being there for me, always. Finally, my warmest love and eternal thanks to my husband Pradeep Sarin, whose unwavering support and practical yet creative advice sustained me through graduate school.

Table of Contents

A۱	ostra	\mathbf{ct}		ii		
A	acknowledgements					
Li	st of	Tables	s	iii		
Li	st of	Figure	es	ix		
1.	Intr	oducti	ion	1		
2.	Fini	ite tem	perature Mott transition in the degenerate Hubbard model	5		
	2.1.	The M	lott transition	5		
	2.2.	The H	Subbard model	9		
	2.3.	Dynan	nical mean-field equations	9		
		2.3.1.	Hirsch-Fye Quantum Monte Carlo algorithm	1		
		2.3.2.	Implementation	13		
	2.4.	Result	s	15		
		2.4.1.	Effect of doping	L5		
		2.4.2.	Coexistence between metallic and insulating phases	6		
		2.4.3.	Convergence of solutions	21		
		2.4.4.	Compressibility divergence	22		
	2.5.	Phase	diagram	23		
	2.6.	Discus	sion	25		
	2.7.	Summ	ary	30		
3.	Den	sity F	unctional Theory, LDA, LDA+U and LDA+DMFT 3	31		
	3.1.	Densit	y functional theory	31		

		3.1.1.	LDA	31
		3.1.2.	LDA+U	33
		3.1.3.	LDA+DMFT method	36
	3.2.	Struct	ure of the LMTART program	39
	3.3.	DMFT	C Loop	42
		3.3.1.	Impurity solver: Hubbard-I method	46
	3.4.	Prepar	ring control files for LMTART	48
		3.4.1.	<i>INI</i> file	49
		3.4.2.	STR file	50
		3.4.3.	Modifications for anti-ferromagnetic solution	53
		3.4.4.	HUB file	54
4.	Elec	ctronic	structure and properties of f -band materials: YbRh ₂ Si ₂ .	60
	4.1.		uction	60
	4.2.		rties of $YbRh_2Si_2$	61
	4.3.	_	structure calculation of $YbRh_2Si_2$	62
	1.0.	4.3.1.	LDA calculation	63
		4.3.2.	LDA+U calculation	66
		4.3.3.	Effect of the double counting term:	70
		4.3.4.	Comparison with other methods involving the double-counting	
		1.0.1.	term	71
		4.3.5.	Effects of pressure	75
		4.3.6.	Anti-ferromagnetic solution	76
	4.4.	Magne	etic Anisotropy Energy	78
	4.5.	Summ	ary and Conclusions	82
5 .	Elec	tronic	structure and properties of f -band materials: Americium	85
	5.1.	Introd	uction	85
	5.2.	LDA	and LDA+U band structure calculation of Americium	90
		5.2.1.	Effect of the double counting term	99

1 /:	Vita				
Re	References				
6.	Sun	nmary	and conclusions	129	
	5.4.	Summ	ary and Conclusions	128	
		5.3.3.	LDA+DMFT Results	113	
		5.3.2.	Tight-binding calculation	106	
		5.3.1.	Hubbard-1 method	104	
	5.3.	LDA+	DMFT method	104	
		5.2.2.	Volume behavior	100	

List of Tables

3.1.	Input file nio.ini	51
3.2.	Input file nio.str	52
3.3.	Input file nio.ini for anti-ferromagnetic NiO	54
3.4.	Input structure file nio.str for the anti-ferromagnetic case	55
3.5.	Input hub file nio.hub	58
3.6.	Partial occupancies for Ni in nio.hub	59
4.1.	Input file ybrh2si2.str	63
4.2.	Input file ybrh2si2.ini	64
4.3.	Input file ybrh2si2.hub	65
4.4.	Input file ybrh2si2.str	78
5.1.	Input file am.str	90
5.2.	Input file am.ini	91
5.3.	Input file am.hub	92
5.4.	Equilibrium volumes for Am in \mathring{A}^3	100

List of Figures

2.1.	Left: Temperature versus pressure phase diagram of $\kappa\text{-}(\text{BEDT}-\text{TTF})_2\text{Cu}[1]$	$N(CN)_2Cl$
	for different crystals. The grey circle near 200 kBar represents the crit-	
	ical point. Right: relative sound velocity (w.r.t. its value at 90K) as	
	a function of temperature at various pressures. From D. Fournier et.	
	al. [28]	6
2.2.	Relative volume as a function of pressure in cerium. From Beecroft and	
	Swenson [30]	6
2.3.	Phase diagram of Hubbard model at the particle-hole symmetric point	
	$\mu = U/2$. The solid lines denote $U_{c1}(T)(\text{left})$ and $U_{c1}(T)(\text{right})$. The	
	dashed line denotes the first order transition line. The black circle at the	
	top is the position of the second-order transition (U_{MIT}, T_{MIT})	8
2.4.	Hirsch-Fye Quantum Monte Carlo algorithm	14
2.5.	n_f vs. μ curves in the half-filled case for a single band with $\beta=1/T=$	
	$32, \Delta \tau = 0.5, D = 1$. The interaction has a value $U = 1.5$ (left) and	
	U = 3.2 (right)	16
2.6.	n_f vs. μ curves at $\beta = 8$	17
2.7.	Coexisting solutions for U=2.44, $\beta=64$ in the single band case	18
2.8.	Imaginary part of Green's functions for U=2.44, $\beta=64$	18
2.9.	Left: Occupation number for various values of β . Right: Occupation	
	number for $\beta = 64$ metallic and insulating solution	19
2.10.	Particle occupation n function of μ for different temperatures in the 2-	
	band model at U=3.0. The top panel shows curves with $T > T_{MIT}$ and	
	in the bottom panel we have $T < T_{MIT}$	20

2.11.	Left: Metallic seed obtained from U=2.8. Right: Insulating seed obtained	
	from U=3.5	21
2.12.	Metallic and insulating Green's function for $U=3.0$, $\beta=40({\rm left})$ and	
	$\beta = 64 (right) \dots \dots$	21
2.13.	Convergence of metallic (left) and insulating (right) Green's function	22
2.14.	1-band model, U=4.0. Top: Compressibility as a function of chemical	
	potential. Bottom: Inverse compressibility $\kappa^{-1} = (dn/d\mu)^{-1}$ at U=4.0	
	in the 1-band model as a function of T. The solid line is the function	
	$\kappa^{-1} \sim (T - T_C)^b$ with $b \sim 0.47$	23
2.15.	Left: Inverse compressibility $\kappa^{-1} = (dn/d\mu)^{-1}$ at U=2.46 in the 1-band	
	model. The solid line is the function $\kappa^{-1} \sim (T - T_C)^b$ with $b \sim 0.33$.	
	Right: κ^{-1} at a constant doping $n=1.003$ as a function of T in the	
	2-band model. The solid line is a fit to a power law using the functional	
	form $\kappa \approx (T - T_c)^b$ with the power $b \sim 1/3$. The intercept with the	
	T -axis gives our estimate for $T_c = 0.0288$	24
2.16.	Schematic phase diagram for the 1-band Hubbard model. The cross	
	sections are on the $T-\mu$ plane for different values of U with U increasing	
	towards the top of the figure. The peaks are symmetric about $\mu=U/2$.	
	μ_{c1} and U_{c1} are the chemical potential and interaction respectively below	
	which the insulating solution does not survive. μ_{c2} and U_{c2} are those	
	above which the metallic solution does not exist. The black circle denotes	
	the second order transition point (U_{MIT}, T_{MIT}) at $n = 1$. The shaded	
	regions denote the coexistence region between metallic and insulating	
	phases	26
2.17.	Phase diagram for U=4.0. The black circles denote are obtained from	
	QMC simulations. The dashed and the dotted lines denote μ_{c1} and μ_{c2}	
	lines respectively.	27

2.18.	Critical slowing down observed in the vicinity of μ_{c1} and μ_{c2} for the	
	1-band model at $U=4.0, \beta=64$. The inverse number of iterations	
	required for the metallic solution to converge goes to zero as we near	
	μ_{c2} and those of the insulating solution to converge goes to zero as we	
	approach μ_{c1} . The arrows indicate the directions in which the boundaries	
	were approached	28
2.19.	Schematic phase diagram for the 2-band case. There is an asymmetry in	
	the triangular peaks as compared to the 1-band case. The cross sections	
	are on the $T-\mu$ plane for different values of U as before. μ_{c1} and U_{c1}	
	are the chemical potential and interaction respectively below which the	
	insulating solution does not survive. μ_{c2} and U_{c2} are the chemical po-	
	tential and interaction above which the metallic solution does not exist.	
	U_{MIT} is the value of the interaction at which the metal-insulator tran-	
	sition takes place. The shaded portions are the regions of coexistence	
	between the metallic and the insulating solutions	29
3.1.	Flow diagram for LDA+DMFT scheme	43
3.2.	Unit cell for NiO and translation vectors	53
3.3.	Unit cell for anti-ferromagnetic case	55
4.1.	Body centered tetragonal crystal structure for $YbRh_2Si_2$	62
4.2.	Energy bands of $YbRh_2Si_2$ – Full Potential (left) and Atomic Sphere Ap-	
	proximation(right). The colored regions in are the fat bands for Yb:4f	67
4.3.	Energy bands of $YbRh_2Si_2$. The colored regions in are the fat bands for	
	Yb:5d (left) and Rh(4d) and Si:3p(right)	67
4.4.	Energy bands of Yb: $4fz(x^2-y^2)$	68
4.5.	Energy bands of Yb:LDA+U, U=2,4,6,8eV	69
4.6.	Position of center of $4f$ -bands of Yb as a function of the interaction U .	70
4.7.	Position of center of $4f$ -band as a function of the double-counting term	
	\bar{U} for U=4eV (top) and U=6eV(bottom)	72
4.8.	Energy bands(left) and DOS(right) of Yb:4f, LDA+U, U=4eV,	73

4.9.	Energy bands(left) and DOS(right) of Yb:4f, LDA+U, U=6eV	73
4.10.	Location of the 4f-bands in various schemes. The original double-counting	
	where $U = \bar{U}$ and the one used by Mazin et.al [54] as described above do	
	not predict a magnetic ground state. The empirical method described in	
	section 4.3.3 does predict the correct ground state	75
4.11.	Dependence of magnetic moment on relative volume	76
4.12.	Application of pressure on the magnetic solution	77
4.13.	Energy bands of Yb in the anti-ferromagnetic case. Top: Bands of Yb-1	
	atom. Bottom: Bands of Yb-2 atom	79
4.14.	χ vs T (from Trovarelli $\it et.al.$ [59])	83
4.15.	from Trovarelli et.al. [58]	83
4.16.	Magnetization as a function of external magnetic field (along z-axis)	84
5.1.	Volumes of actinide elements	86
5.2.	Left: Photoemission spectra of Am by Naegele [60]. Right: Relative	
	volume of americium as a function of pressure obtained by Lindbaum et .	
	al. [62]	86
5.3.	Four phases of Americium (Lindbaum et. al [62])	88
5.4.	Energy bands of Am in LDA+U, no spin-orbit coupling. The colored	
	regions are the fat bands of Am:5f	93
5.5.	Density of states of Am in LDA+U, no spin-orbit coupling. The black	
	curve is the total DOS and the red curve is the partial 5f-DOS	94
5.6.	Energy bands of Am in LDA+U, with spin-orbit coupling. The colored	
	regions are the fat bands of Am:5f. Note the initial separation (for $U=0$)	
	between the filled and empty states, which is due to spin-orbit coupling	95
5.7.	Density of states in LDA+U, no spin-orbit coupling. Note the initial	
	separation (for $U=0$) between the filled and empty states, which is due	
	to spin-orbit coupling. The black curve is the total DOS and the red	
	curve is the partial 5f-DOS	96

5.8.	Position of center of the Am $5f$ -band as a function of the interaction	
	strength	97
5.9.	Gap between spin-up and spin-dn electrons as a function of the interaction	98
5.10.	Occupancy of Am $5f\mbox{-band}$ as a function of the interaction strength $U\;$.	98
5.11.	Effect of U_{dc} : Position of the center of the f -band as a function of the	
	U_{dc} , with U kept at $4eV$	99
5.12.	Total energy (-61011 Ry) as a function of relative volume V/V_0 for various	
	values of interaction $U(\text{in eV})$	101
5.13.	Input file $lmt.am$ for treating f -electrons as core	102
5.14.	Energy bands of Am treating 5f electrons as core	103
5.15.	DOS of Am treating 5f electrons as core	103
5.16.	Comparison of DOS : LDA and Tight binding methods	107
5.17.	Comparison of DOS : LDA and Tight binding methods	108
5.18.	Comparison of DOS : LDA and Tight binding methods	109
5.19.	Comparison of DOS : LDA and Tight binding methods	110
5.20.	Impurity level (w.r.t E_F) as a function of relative volume	111
5.21.	Tight binding hoppings as a function of relative volume	111
5.22.	Am: Density of States as a function of U for the tight-binding model $\ \ .$	112
5.23.	Energy vs. relative volume	113
5.24.	Pressure vs. relative volume	114
5.25.	Am DOS in LDA	115
5.26.	Am DOS in LDA	116
5.27.	Am DOS in LDA	117
5.28.	Am DOS in LDA+DMFT: $U=U_{DC}=4.5eV$	119
5.29.	Am DOS in LDA+DMFT: $U = U_{DC} = 4.5 eV$	120
5.30.	Am DOS in LDA+DMFT: $U=U_{DC}=4.5eV$	121
5.31.	Am DOS in LDA+DMFT: $U = 4.5eV, U_{DC} = 4.1eV$	122
5.32.	Am DOS in LDA+DMFT: $U = 4.5eV, U_{DC} = 4.1eV$	123
5 33	Am DOS in LDA+DMFT: $U = 4.5 eV U_{DG} = 4.1 eV$	194

5.34. Density of states at Fermi level in LDA and LDA+DMFT	125
5.35. Ratio of 5f-DOS over total DOS	126
5.36. Position of center of 5f-band	127

Chapter 1

Introduction

The understanding of the structure and properties of materials, the relationship between their phases and the mechanism that gives rise to transitions between the phases have been the focus of a number of theoretical and computational investigations in solid state physics. There have been two main approaches that have contributed to progress in determining the structure and properties of materials: studies of model Hamiltonians and first-principles or ab-initio calculations. We can learn aspects of universal behavior of systems by studying simple models. For example, critical exponents of measurable quantities such as heat capacity and susceptibility derived from the Ising model are applicable to a wide variety of systems. On the other hand, non-universal features require detailed modeling that involve particulars such as atomic charge and crystal structure. This thesis deals with the realistic modeling of strongly correlated materials using tools from both the approaches.

Model Hamiltonians have proved to be very useful in understanding materials with strong correlation effects. These are materials in which there is a competition between the kinetic energy and the interaction energy of electrons. Strong correlation effects arise due to partially filled d and f shells in the atoms constituting the materials. Strongly correlated materials exhibit interesting physical properties such as high temperature superconductivity, anomalous behavior in resistivity, specific heat and transport properties. Examples of strong correlation effects are seen in high temperature superconductors such as copper oxides, Uranium and Cerium based heavy fermion systems, colossal magnetoresistance materials such as manganites and carbon based compounds such as bucky balls and carbon nanotubes.

The Mott-Hubbard metal-insulator transition [1] is another important effect induced

by strong correlations. It has been observed in V_2O_3 [2], pyrites such as $Ni(Se,S)_2$ [3], and layered organic conductors [4]. It is a difficult problem to treat theoretically since the electron kinetic energy and interaction energy are of the same order. Since there is no natural small parameter, standard perturbative techniques fail. The dynamical mean-field theory (DMFT) [5] is a framework in which both localized bands in the insulating phase and quasi-particle bands in the metallic phase are treated on an equal footing. It is exact in the limit of infinite dimensions. In particular, DMFT studies of the Hubbard model have been successful in understanding some universal aspects of the physics of the Mott transition such as high temperature behavior near Mott endpoint [], phase diagram at integer occupation [] and transfer of spectral weight near the transition [6, 7]. However, the main drawback of studying models is that physical quantities such as interaction strength and doping need to be treated as parameters.

A different approach to studying electronic structure of solids is based on first-principles (or ab-initio) techniques. There are no empirically adjustable parameters here. The input to these calculations consists only of atomic charges and crystal structures, hence a detailed modeling of the solid is possible. The most widely used tool in ab-initio calculations is Density Functional Theory [8,9], especially in the Local Density Approximation (LDA) or Generalized Gradient Approximation (GGA) [10]. Density functional methods have been tremendously successful in treating weakly correlated materials such as simple metals and semi-conductors. They provide a simple conceptual picture of the ground state and correctly predict excitation spectra and transport properties in such materials. However, these methods often fail to capture the correct physics in strongly correlated materials.

In recent years, a combination of Local Density Approximation and dynamical meanfield theory (LDA+DMFT) has been successfully used to study strongly correlated materials [11, 12]. In this approach, the light s, p (sometimes d) electrons which have extended wave functions are treated by LDA. The localized d (or f) electrons are treated in the DMFT framework. This method can be used to calculate excitation spectra and total energy as well as correlation functions. Theoretically, the LDA+DMFT method can be constructed from an effective action point of view [13] where the free energy is a functional of the local Green's function and the density. Other extensions to LDA have also been tried: LDA+U [14–16], which has been shown to be a static limit of LDA+DMFT [17] and LDA+GW [18,19] which is a perturbative calculation starting from LDA spectra.

LDA+DMFT has proved to be a powerful tool for the realistic modeling of strongly correlated electron systems. There have been various successes: Phase diagram of plutonium [20], α - γ transition in the 4f electron system Cerium [21, 22], optical and transport properties of La_{1-x}Sr_xTiO₃ [23,24], Mott Hubbard metal-insulator transition in V₂O₃ [25] to name a few. This thesis is an attempt to understand the structure and properties of two strongly correlated materials using the above methods, with a focus on the metal-insulator Mott transition.

This thesis is organized as follows:

In chapter 2 we begin with the physical ideas behind the Mott transition. We introduce the Hubbard model. We go through the mechanism behind dynamical mean-field theory and its mapping to the impurity model. We then describe one of various ways to solve for the properties of the impurity model. This is the quantum Monte Carlo technique, which is exact, but computationally difficult for accessing low temperatures. Studying the behavior of the system as a function of various parameters, we look into the details of the finite temperature doping driven Mott transition. We concentrate on the behavior of the charge compressibility near the transition.

Chapter 3 serves two purposes. In the first part, we briefly review density functional theory from an effective action point of view. We discuss existing density functional methods that go beyond the standard LDA technique, and can be used when strong correlations are present. These are the LDA+U and LDA+DMFT methods. We outline the numerical implementation of another impurity solver for the DMFT loop, the so-called Hubbard-1 approximation, which we will employ in a later calculation. The latter part of 3 is devoted to the details of our computation scheme. We describe the various input files that are required in the computer program.

We then turn to applications of the above methods to real materials in the lanthanide and actinide series. In chapter 4 we study the ground state and magnetic properties of a heavy fermion compound YbRh₂Si₂. We also propose a procedure in the LDA+U implementation, that improves results for the ground state properties. The theoretical tools we discussed, the physical concepts behind the Mott transition and the insights we gained into the details of the band structure calculation all come together in chapter 5. We use the LDA+DMFT technique, with the Hubbard-1 impurity solver, to investigate the structure, equilibrium volume, and details of the Mott transition in elemental Americium.

We conclude in chapter 6 with a summary of the thesis, and directions for future work.

Chapter 2

Finite temperature Mott transition in the degenerate Hubbard model

The Mott transition is a metal-insulator transition that is driven by electron-electron interactions [1]. It occurs when the ratio of the electron interaction strength to the bandwidth is increased. Experimentally, this phenomenon is realized in many compounds such as V_20_3 [2], $Ni(Se,S)_2$ [3,26] and the family of organic conductors κ -BEDT [4,27]. On the theoretical side, the Hubbard model is among the first, and perhaps the simplest model that can capture the essential physics of the transition. In recent years, tremendous theoretical progress has been made in understanding the Mott transition by applying the dynamical mean-field theory (DMFT) [5] to the Hubbard model. In this chapter, we study finite temperature aspects of the doping driven Mott transition in the Hubbard model, and the behavior of the compressibility near the Mott endpoint within the DMFT approach.

2.1 The Mott transition

Experimental evidence

The classical system in which a Mott transition is observed is V_2O_3 doped with Cr or Ti [2]. The transition can be driven by varying pressure, chemical potential (or doping) and temperature. Recently, a first order metal-insulator transition was observed in the organic superconductor κ -(BEDT – TTF)₂Cu[N(CN)₂Cl, as a function of hydrostatic pressure [28]. The study shows a large softening of sound velocity of the material near the critical point. The sound velocity is proportional to the square root of compressibility, hence a sharp decrease in the velocity points to a divergence in the compressibility.

Fig. 2.1 shows the phase diagram and the dip in sound velocity in this system.

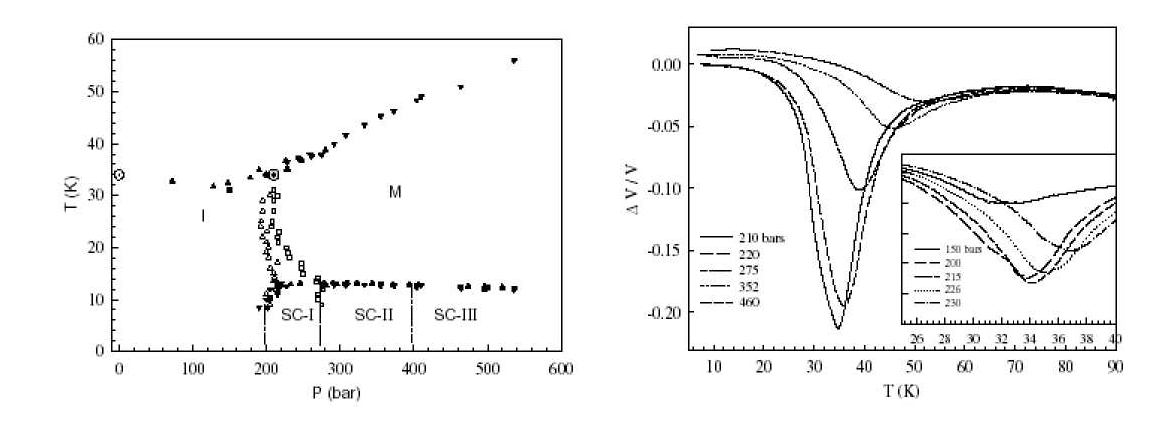


Figure 2.1: Left: Temperature versus pressure phase diagram of κ -(BEDT – TTF)₂Cu[N(CN)₂Cl for different crystals. The grey circle near 200 kBar represents the critical point. Right: relative sound velocity (w.r.t. its value at 90K) as a function of temperature at various pressures. From D. Fournier *et. al.* [28].

It has been suggested by B. Johansson [29] that the Mott transition concept is also relevant to lanthanide and actinide materials. The α - γ transition in Cerium shows certain universal features that are common to other systems in which a metal-insulator transition is observed. For example, Beecroft and Swenson [30] measured a large decrease in the compressibility in the transition from the insulating low-pressure phase (γ -Ce) to the metallic high-pressure phase (α -Ce). Fig. 2.2 shows the pressure-volume isotherms for the α - γ transition in Ce.

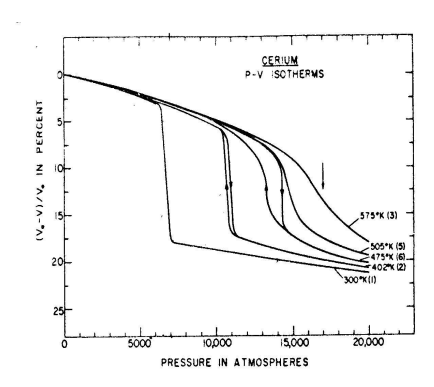


Figure 2.2: Relative volume as a function of pressure in cerium. From Beecroft and Swenson [30]

Theoretical understanding

From a theoretical point of view, the electronic structure of solids has been well understood in two limits. When the overlap between electron orbitals is large, a wave-like description is relevant, and band theory accounts for most of the properties of the solid. At the other end, when the electron orbitals are far apart, a real-space description in terms of localized atomic wave-functions is valid.

Strongly correlated materials fall away from either of these limits. Strong correlation effects arise due to the dual character of the electron: wave-like and particle-like. In other words, there is a competition between the kinetic energy and the electron-electron interaction energy. One of the earliest models that was proposed to capture the effects of strong correlations in d and f-band materials was the Hubbard model [31]. However, it has been solved exactly only in one dimension, where there cannot be a finite temperature phase transition.

Standard methods such as perturbation theory fail in the strong correlation problem since a method that can simultaneously treat itinerant and localized nature of electrons is required. One such framework that can describe both metallic (itinerant) and insulating (localized) phases is dynamical mean-field theory [5]. DMFT can be regarded as the quantum analog of the classical mean-field theory for magnetism. The essence of the method is to replace the interactions of an electron at a lattice site with its neighbors by an effective interaction with an average field. This effective field represents the dynamic state of the neighbors.

In the DMFT framework, the metal-insulator transition (MIT) can be interpreted as arising from bifurcation points of a functional of the local Green's function. The case of the correlation driven MIT at half-filling, is now well understood. At temperature T=0 there are two bifurcation points, one denoted by $U_{c1}(T=0)$ where the insulating solution disappears, and the other denoted by $U_{c2}(T=0)$ where the metallic solution disappears [32]. It was found that in the U-T phase diagram of the frustrated Hubbard model, there is a region where two mean-field solutions, one metallic-like and one insulating-like can be obtained. This region is delimited by the $U_{c1}(T)$ and $U_{c2}(T)$ lines

as shown in Fig. 2.3. Within the region there is a first-order MIT line [33,34] that ends in a finite temperature second-order critical point (U_{MIT}, T_{MIT}) with a rapid variation of the susceptibility connected to the double occupancy [6,35]. At higher temperatures the $U_{c2}(T)$ and $U_{c1}(T)$ lines become crossover lines.

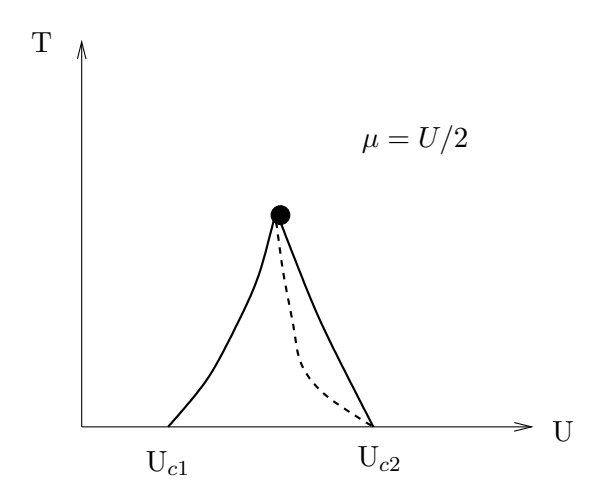


Figure 2.3: Phase diagram of Hubbard model at the particle-hole symmetric point $\mu = U/2$. The solid lines denote $U_{c1}(T)(\text{left})$ and $U_{c1}(T)(\text{right})$. The dashed line denotes the first order transition line. The black circle at the top is the position of the second-order transition (U_{MIT}, T_{MIT}) .

The doping driven MIT at zero temperature was studied in [36]. It was shown that there are two solutions in an area bound by the curves $\mu_{c1}(U)$, where the insulating solution disappears, and $\mu_{c2}(U)$, where the metallic state disappears. The finite temperature aspects of the doping driven Mott transition will be the subject of this chapter. We will concentrate on the paramagnetic phase, and will not consider effects of long range order.

We will also discuss the behavior of the charge compressibility near the Mott endpoint at finite temperatures. The compressibility is known to diverge at the density driven MIT in two dimensions at T=0 [37]. This behavior has also been observed on other models of correlated electron systems such as the t-J model indicating that this phenomenon is quite general [38]. Simple models of the Mott transition, such as the Gutzwiller approximation or the slave-boson approach predict a finite compressibility [39]. It is important to understand the physical origin of this result, and to see if it is realized in the DMFT solution of the Hubbard model. The previously investigated bifurcation points within the DMFT, have either a finite charge compressibility, such as in the T=0 density driven Mott transition, or a vanishing charge compressibility, as in the T=0 correlation driven transition.

2.2 The Hubbard model

We begin with a general Hubbard Hamiltonian that has m-band degeneracy. Since we will be working in the grand canonical ensemble, we introduce a chemical potential in the Hamiltonian, given by:

$$H = -\sum_{\{i,m,\sigma\}} t_{ij}^{mm'} c_{im\sigma}^{\dagger} c_{im\sigma} + \frac{1}{2} \sum_{i,m,m'\sigma} U n_{im\sigma} n_{im'-\sigma} + \frac{1}{2} \sum_{i,m\neq m'\sigma} U n_{im\sigma} n_{im'\sigma} - \mu \sum_{im\sigma} n_{im\sigma}$$

$$(2.1)$$

Here $c_{im\sigma}^{\dagger}$ creates an electron in a state localized at site i with orbital index m and spin $\sigma = \uparrow, \downarrow$. The first term describes the hopping between nearest neighbor sites $\langle ij \rangle$ where the hopping integral t has been assumed to be independent of the site indices. The parameter U is the on-site Coulomb repulsion, namely, the energy cost associated with having a double occupancy on each site. $n_{im\sigma} = c_{im\sigma}^{\dagger} c_{im\sigma}$ is the particle occupation number. t and U have been assumed to be independent of the band indices. This model is particle-hole symmetric when $\mu = \frac{(2m-1)U}{2}$.

2.3 Dynamical mean-field equations

The central idea of this method is to map a lattice model with many degrees of freedom, such as the Hubbard model in Eqn. (2.1), onto a one-site impurity model with fewer degrees of freedom [5]. This is supplemented by a self-consistency condition that determines the effective bath (effect of the other degrees of freedom) with which the impurity interacts. This approach can be shown to be exact in the limit of infinite dimensions $d \to \infty$, or large lattice coordination number z, with an appropriate scaling of parameters [40].

We consider the Hubbard model in (2.1) on a Bethe lattice with large connectivity z. A semi-circular density of states $\rho_o(\epsilon) = (\frac{1}{2\pi t^2})\sqrt{4t^2 - \epsilon^2}$ is obtained where D=2t is

the half-bandwidth. In this case, we can write the effective action for this model as:

$$S_{eff} = \int_{0}^{\beta} d\tau \int_{0}^{\beta} d\tau' \sum_{\langle ij\rangle, m, \sigma} c_{im\sigma}^{\dagger}(\tau) \mathcal{G}_{0m\sigma}^{-1}(\tau - \tau') c_{jm\sigma}(\tau')$$

$$+ \frac{U}{2} \int_{0}^{\beta} d\tau \left(\sum_{i, m, m', \sigma} n_{im\sigma} n_{im'-\sigma} + \sum_{i, m \neq m', \sigma} n_{im\sigma} n_{im'\sigma} \right)$$
(2.2)

In the $d \to \infty$ limit the above lattice model is mapped on to the degenerate Anderson impurity model.

$$H_{AM} = H_0 + H_I \tag{2.3}$$

$$H_0 = \sum_{k \ge 2, m, \sigma} \epsilon_{km} c_{km\sigma}^{\dagger} c_{km\sigma} + \sum_{k \ge 2, m, \sigma} (V_{km} c_{km\sigma}^{\dagger} f_m + h.c) + \sum_{m} (E^f + (2m - 1)/2U) n_{m\sigma}$$
(2.4)

$$H_I = U \sum_{m < m', \sigma} \left\{ n_{m\sigma} n_{m'\sigma} - \frac{1}{2} (n_{m\sigma} + n_{m'\sigma}) \right\}$$

$$(2.5)$$

The Weiss function \mathcal{G}_{0m} in Eqn. (2.2) is given by a self-consistency condition

$$\mathcal{G}_{0m}^{-1}(i\omega_n) = i\omega_n + \mu - t^2 G_m(i\omega_n)$$
(2.6)

Here $G(i\omega_n)$ is the local Green's function for the impurity. The conduction orbitals have index k=2,N and the impurity f-orbital corresponds to k=1. c_{km} and c_{km}^{\dagger} are the band electron annihilation and creation operators, V_{km} is the hybridization between the band and the impurity electrons. $n_m = f^{\dagger}_m f_m$ is the occupation number for the impurity electrons and E^f is the f-level energy.

In terms of the hybridization function $\Delta_m(i\omega) = \sum_k \frac{V_{km}^2}{i\omega - \epsilon_{km}}$ the DMFT equation for the Bethe lattice can be written as

$$t^2 G_m(i\omega)[\Delta] = \Delta_m(i\omega) \tag{2.7}$$

The coupled problem of finding the impurity Green's function G and the Weiss field G_0 is solved iteratively until required convergence is reached. Impurity models have been intensely studied for the past few decades, and a number of analytical and numerical tools exist to tackle them. In the next section, we focus on one numerical method: the Quantum Monte Carlo (QMC) algorithm by Hirsch and Fye [41], to obtain the Green's function G.

2.3.1 Hirsch-Fye Quantum Monte Carlo algorithm

We discretize the time interval $[0,\beta]$ into L slices of length $\Delta \tau$ such that

$$\Delta \tau_l = l \Delta \tau$$
, $l = 1, 2, \dots, L$ and $\beta = L \Delta \tau$.

The partition function is

$$Z = Tr \exp\{-\beta H\} = Tr \Pi \exp\{-\Delta \tau (H_0 + H_I)\}$$
(2.8)

Using the Trotter formula, the discretized partition function is

$$Z \simeq Z^{\Delta \tau} = Tr\Pi \exp\{-\Delta \tau H_0\} \exp\{-\Delta \tau H_I\}$$
 (2.9)

The discretized Green's function is

$$G_{m,k_1,k_2}^{\Delta\tau}(\tau_{l_1}\tau_{l_2}) = \left\langle T(c_{mk_1}(\tau_{l_1})c_{mk_2}^{\dagger}(\tau_{l_2}) \right\rangle$$

$$\frac{1}{Z^{\Delta\tau}} Tr e^{-\beta H} c_{mk_1}(\tau_{l_1})c_{mk_2}^{\dagger}(\tau_{l_2})$$
(2.10)

for $l_1 > l_2$. We then use a discrete Hubbard-Stratonovich transformation to decouple the quartic interaction in H_I [42].

$$\exp\left[-\Delta \tau U \left(n_m n_{m'} - \frac{1}{2}(n_m + n_{m'})\right)\right] = \frac{1}{2} \sum_{S_{mm'} = \pm 1} \exp\left[\lambda S_{mm'}(n_m - n'_m)\right] \quad (2.11)$$

where $\cosh \lambda = \exp(\Delta \tau U/2)$ and $S_{mm'}(\tau_l)$ are auxiliary Ising-like fields at each time slice. This transformation renders H_{AM} quadratic in $S_{mm'}\{\tau_l\}$.

Using (2.11) we write the partition function as

$$Z^{\Delta\tau}[\{S_{mm'}\}] = Tr_{\{S_{mm'}\}} \prod_{m} \det O_m[\{S_{mm'}\}]$$
 (2.12)

Here $O[\{S_{mm'}\}]$ is a $NL \times NL$ (N being the number of conduction orbitals, and L being the number of time slices) matrix defined as

$$(O_m)_{l,l} = I$$

$$(O_m)_{l,l-1} = -e^{(-\Delta \tau H_{0m})} e^{(V_{l-1}^m)(1-2\delta_{l,1})}$$

$$(O_m)_{l,l'} = 0 \quad \text{otherwise}$$
(2.13)

with
$$V_m^l = \lambda \sum_{m \neq m'} S_{mm'}(\tau_l) |m\rangle\langle m|$$
 for $m < m'$.

For the auxiliary spin dependent Green's function, we have

$$G_m^{\Delta \tau}[\{S_{mm'}\}] = O_m^{-1}[\{S_{mm'}\}] \equiv G_m$$
 (2.14)

We then get a relation between Green's functions for two different configurations.

$$G_m^{-1} = A_m G_m (2.15)$$

where
$$A_m = 1 + (1 - G_m)(e^{V'_m - V_m} - 1).$$
 (2.16)

This is a $L \times L$ matrix equation.

If we now make only one local change in the field at one time slice such that two configurations differ by a single spin

$$S_{mm'} \to S'_{mm'}$$
 for $m > m'$
 $\to -S'_{mm'}$ for $m < m'$

the above equations are simplified. $\exp\{V'_m - V_m\}$ has only one non-zero diagonal element at the l-th part of the matrix O. $A^{-1}_{lk}=0$ for $l\neq k$ and $\det A_m=A_m{}^{ll}=1+(1-G_m{}^{ll})(\exp\{V'^l{}_m-V_m{}^l\}-1)$.

We would also need to calculate the Boltzmann ratio of two different configurations which for a single spin flip is given by :

$$R = \prod_{m} R_{m}$$

$$R_{m} = \frac{\det(O'_{m})}{\det(O_{m})} = \det\left[I - (G_{m}^{ll} - I)\left(\exp\{V'_{m} - V_{m}\} - I\right)\right]$$
(2.17)

Again, for a single spin flip, this simplifies to

$$R_m = R_m R_{m'}$$

$$R_m = 1 - [G_m^f(l, l) - 1][\exp(-2\lambda S_{mm'} - 1)]$$

$$R_{m'} = 1 - [G_{m'}^f(l, l) - 1][\exp(2\lambda S_{mm'} - 1)]$$

The f-Green's function simplifies to :

$$G_m^{f}(l_1, l_2) = G_m^{f}(l_1, l_2) + [G_m^{f}(l_1, l) - \delta_1][\exp(-2\lambda S_{mm'} - 1)] \frac{1}{R_m} G_m^{f}(l, l_2)$$
 (2.18)

$$G_{m'}^{f}(l_1, l_2) = G_{m'}^{f}(l_1, l_2) + [G_{m'}^{f}(l_1, l) - \delta_{l1}][\exp(2\lambda S_{mm'} - 1)] \frac{1}{R_{m'}} G_{m'}^{f}(l, l_2)$$
 (2.19)

The physical Green's function is then calculated as an average of the spin-dependent Green's functions.

$$G_m^{physical} = \frac{1}{Z} \sum_{S_{mm'}} G_m[\{S_{mm'}\}](\tau_l) \det O_m[\{S_{mm'}\}]$$
 (2.20)

2.3.2 Implementation

The practical implementation of the above procedure involves the following steps:

- We start with a guess for \mathcal{G}_{0m} and an arbitrary configuration of spins.
- In the first iteration we invert the matrix O_m to obtain $G_m\{S_{mm'}(\tau_l)\}$.
- For the subsequent iterations we change the configuration using a single spin-flip. We calculate the ratio R. If R is greater than a random number (between 0 and 1) chosen we accept the flip and calculate $G_m\{S_{mm'}(\tau_l)\}$. Otherwise we generate the next configuration.
- Every 100 iterations we start the spin configuration chain again by equating all auxiliary spins to zero and calculating the inverse of O_m . This is done to check that the precision has not degraded.
- We then use the self-consistency condition

$$\mathcal{G}_{0m}^{-1}(i\omega_n) = i\omega_n + \mu - t^2 G_m(i\omega_n)$$

to calculate the new Weiss field $\mathcal{G}_{0m}(new)$

- The $\mathcal{G}_{0m}(new)$ thus calculated is fed back into the QMC algorithm in the next step of the iteration.
- This process is iterated till G_m and \mathcal{G}_{0m} converge.

HIRSCH-FYE QMC ALGORITHM

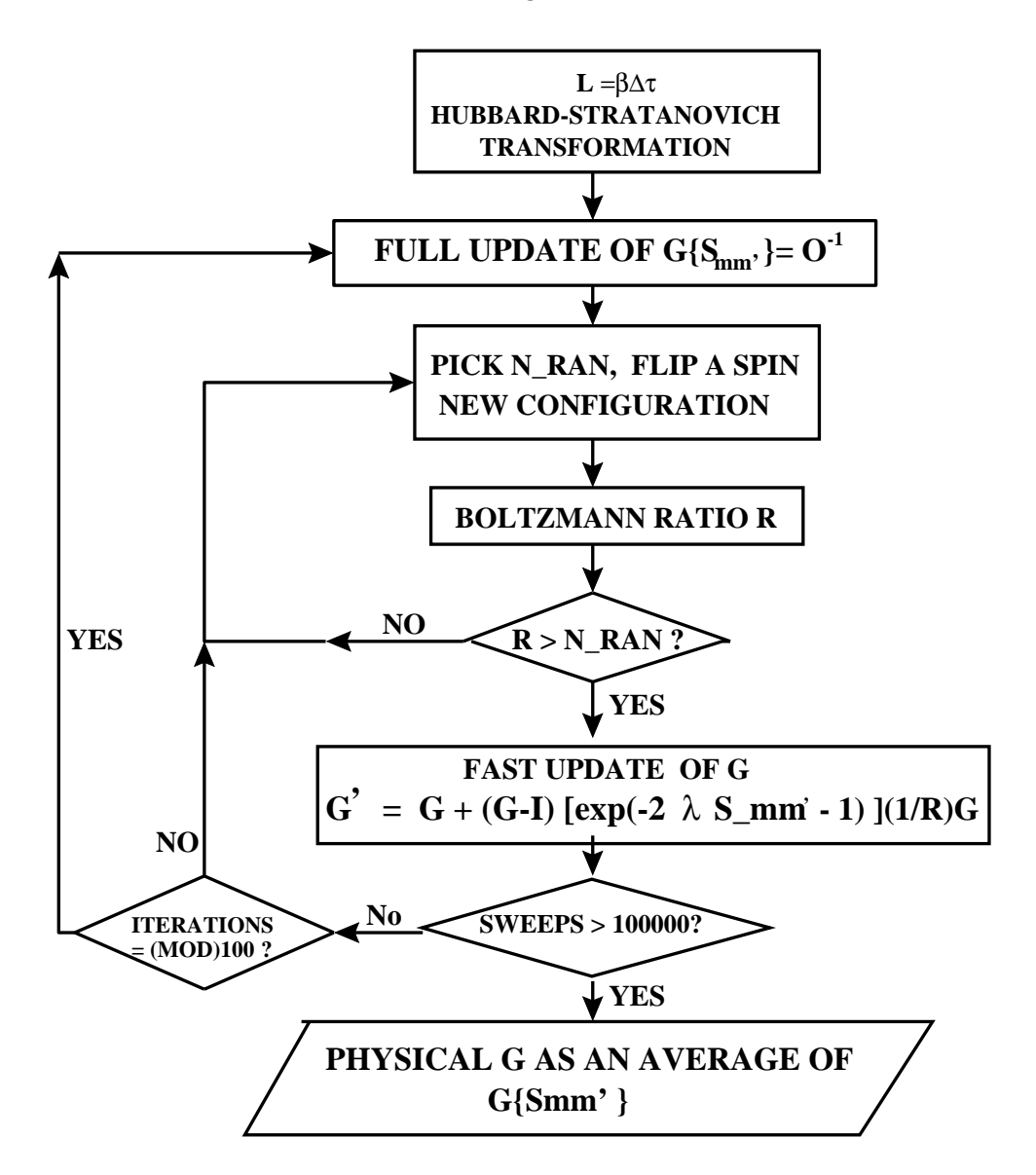


Figure 2.4: Hirsch-Fye Quantum Monte Carlo algorithm

2.4 Results

We use the Hirsch-Fye QMC algorithm to obtain the impurity Green's function and iteratively solve the DMFT equations (2.3)-(2.6). Different phases can be obtained depending on the values of the interaction parameters in the Hamiltonian (Eqn. 2.1). In this section, we investigate the finite temperature aspects of the doping driven metalinsulator transition.

2.4.1 Effect of doping

The total occupation number for the impurity electrons is computed from the Green's function. After the QMC runs stabilize, the full Green's function $G(i\omega)$ is checked to see whether we have metallic or insulating behavior. Curves of the impurity occupation number n_f are plotted against the chemical potential μ .

$$G_{m}(\tau_{i},0) = + \left\langle T\left(c_{m}(\tau_{i})c_{m}^{\dagger}(0)\right)\right\rangle$$

$$G_{m}(0^{+}) \longrightarrow c_{m}(0)c_{m}^{\dagger}(0)$$

$$= 1 - c_{m}^{\dagger}(0)c_{m}(0)$$

$$= 1 - n_{m}$$

$$(2.21)$$

$$n_f^m = 1 - G_m(0^+) (2.23)$$

We concentrate on the paramagnetic case where $n_{\uparrow}=n_{\downarrow}$ for a given band index m. We plot the average occupation number n_f as a function of the chemical potential μ for various values of the interaction U. For the 1-band model, $\Delta \tau = 0.5$ for the 2-band model, $\Delta \tau = 0.25$. all energies are in units of half-bandwidth D=1.

The graph of occupation number n_f versus the chemical potential μ at T=1/32 and U=1.5 for the 1-band model is shown in Fig. 2.5 (left) and that for U=3.2 is shown in Fig. 2.5 (right). For smaller values of the interaction U the occupation number is a smooth function of μ , that is, the system has metallic-like behavior. As U is increased, a gap opens up in the n_f - μ curve near half-filling, indicating the insulating-like behavior of the system. Due to particle-hole symmetry in the 1-band model, we use a shifted chemical potential $\tilde{\mu} = \mu - \frac{U}{2}$.

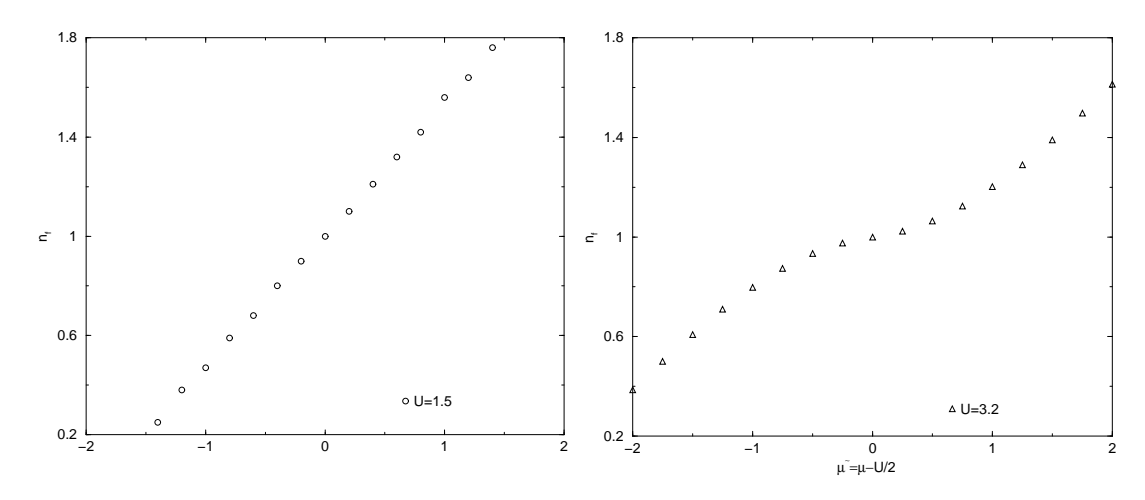


Figure 2.5: n_f vs. μ curves in the half-filled case for a single band with $\beta = 1/T = 32, \Delta \tau = 0.5, D = 1$. The interaction has a value U = 1.5 (left) and U = 3.2 (right).

The 2-band results are shown in Fig. 2.6. We concentrate on the region near $n_f = 1$ at T = 1/8. At this high temperature only one solution exists. However, as T is decreased, we see a flat portion in the n_f - μ curve at which the occupation number remains close to 1 over a range of μ .

2.4.2 Coexistence between metallic and insulating phases

Coexistence in the 1-band model

In the region of intermediate U, at sufficiently low temperatures, we expect the metallic and and insulating solutions to exist simultaneously. As we start doping the system a little, the two phases should still coexist. However at high doping we expect the insulating phase to become unstable and disappear. The existence of two phases should result in two simultaneous values for n_f at the same chemical potential. The n_f versus μ curve in Fig. 2.7 shows this coexistence at U=2.44 and $\beta=1/T=64$ in the 1-band model. At $\tilde{\mu}=0$, both the metallic and the insulating solutions are seen. Away from half-filling, the two solutions give different values of n_f . When the doping becomes large, only the metallic solution survives.

In Fig. 2.7, to obtain the two different values of the occupation number, we start

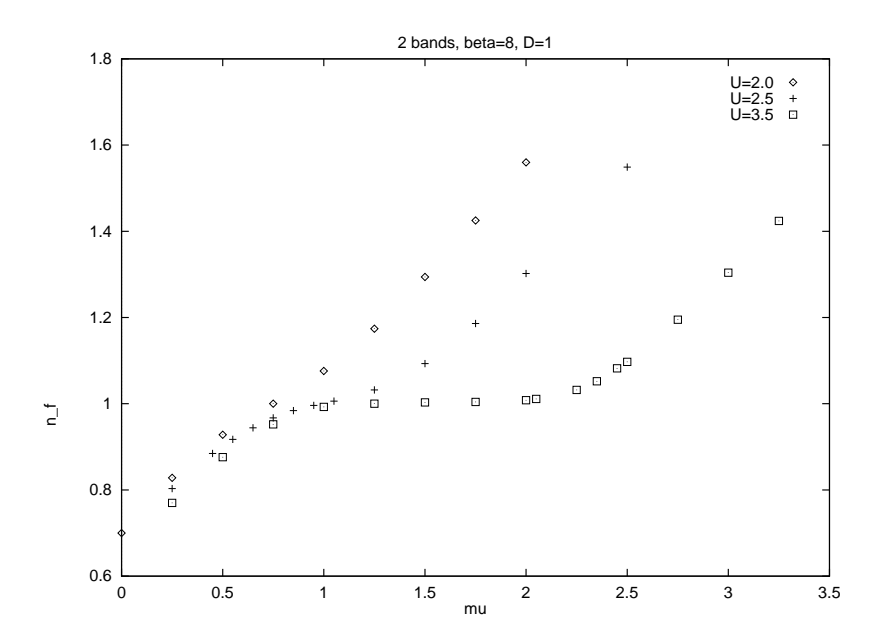


Figure 2.6: n_f vs. μ curves at $\beta = 8$

from two different initial guesses or seeds in the QMC algorithm. The occupation number represented by circles (metallic behavior) are calculated by using a seed from low U. We first start at high doping in a metallic state and continuously evolve towards integer filling. The solution always remains metallic. To obtain the other solution, represented by triangles, we begin with the insulating solution at $\tilde{\mu}=0, n=1$ using a seed from high U and gradually increase the doping. This state is essentially incompressible as n almost remains constant while increasing μ . This can be continuously followed as μ is increased, until the eventual jump of n towards the unique solution present at the higher values of μ . This procedure is later used to determine the location of the coexisting region [43] in the phase diagram. The Green's functions corresponding to these values of n_f are distinct and are shown in Fig. 2.8.

As we increase the interaction to U=4.0 we find that at $\tilde{\mu}=0$ and $T=1/\beta=1/64$ only the insulating solution survives (Fig. 2.9. If we start from a large (hole) doping where only the metallic solution survives and decrease the magnitude of the chemical potential, we find that the metallic solution disappears at a value of the chemical potential $\mu \approx 1.07$. At the same time, if we start at $\tilde{\mu}=0$ where $n_f=1$ and increase the magnitude of doping, the insulating solution disappears at a chemical potential

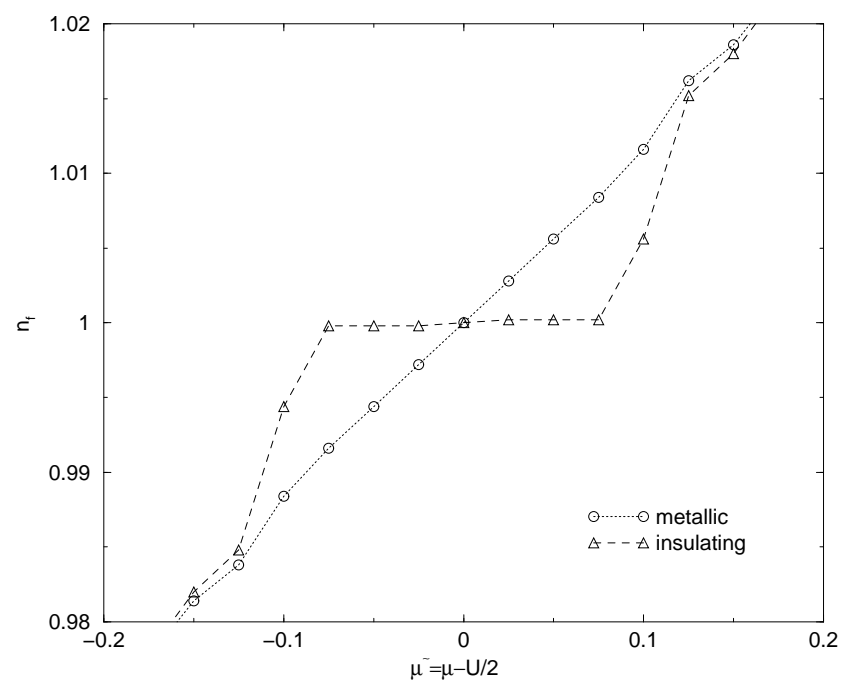


Figure 2.7: Coexisting solutions for U=2.44, $\beta=64$ in the single band case.

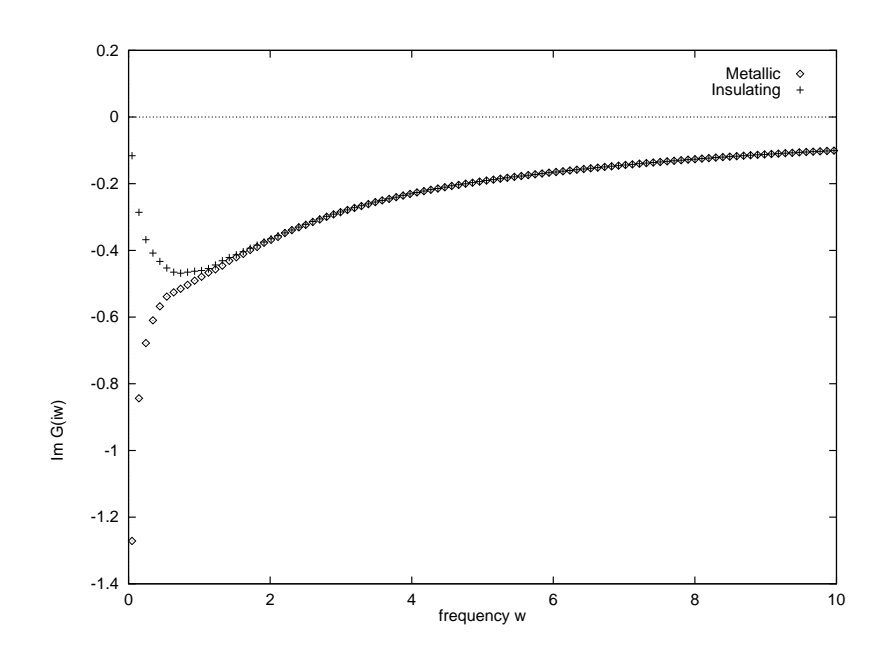


Figure 2.8: Imaginary part of Green's functions for U=2.44, $\beta=64$

 $\mu \approx 1.03$. However at a higher temperature $T = 1/\beta = 1/40$ no coexistence between metallic and insulating solutions is seen.

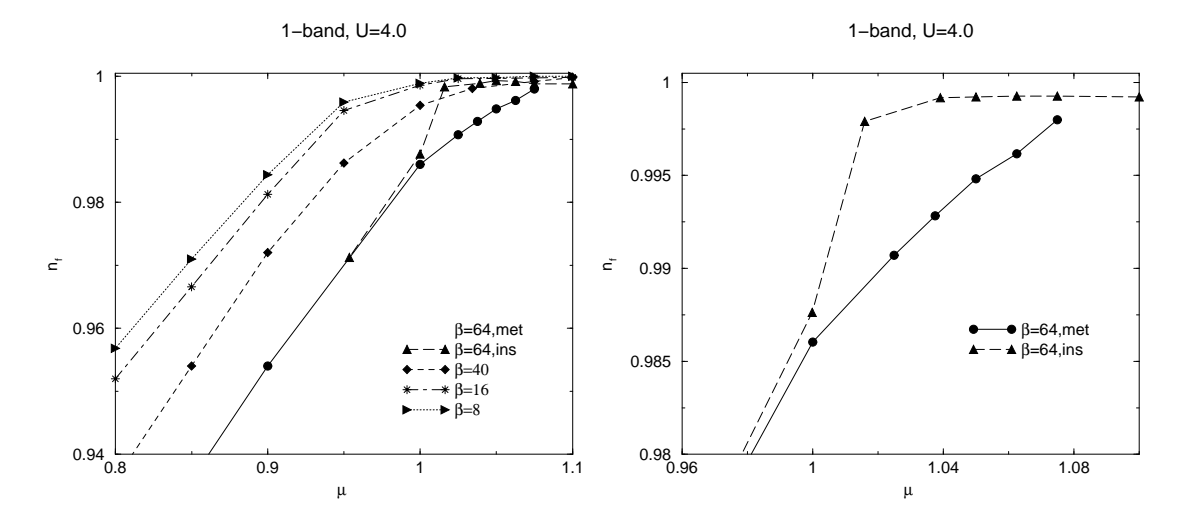


Figure 2.9: Left: Occupation number for various values of β . Right: Occupation number for $\beta = 64$ metallic and insulating solution

Coexistence in the 2-band model

We find coexisting metallic and the insulating solutions near $n_f = 1$ at T = 1/40. In Fig. 2.10 we see the n_f versus. μ curves in the 2-band case for U = 3.0 at various temperatures. As T is decreased, we see that the curves begin to acquire a sigmoidal shape, which is a hallmark of the approach to a second-order critical point in Landau theory of phase transitions.

As discussed in the 1-band case, we followed a careful procedure to obtain coexisting solutions. At T=1/40 two different solutions were found at the same chemical potential $\mu=1.2$. The metallic solution (the circles in Fig. 2.10) was obtained using as starting point, the solution for U=2.8 and the insulating solution (the triangles in the n versus μ curve in Fig. 2.10) was obtained by using the Green's function at U=3.5 as the seed (Fig. 2.11). Using these solutions the n_f versus. μ curve slightly away from $n_f=1$ was obtained. The insulating solution disappeared for increased doping and away from $n_f=1$.

We then study the nature of the solutions as the temperature is raised. Each of the metallic and the insulating solutions at T=1/40 was used as a seed to determine the solution at higher temperatures. It was found that the metallic solution disappeared as the temperature was raised (to T=1/32) near $n_f<1$ but the insulating solution survived. However at $\mu=1.25$ for which $n_f>1$ it was found that both solutions survived till T=1/32. As the temperature was further raised, no coexistence was seen. The Green's function for the two phases at $\mu=1.2$ for T=1/40 and T=1/64 are shown in Fig. 2.12.

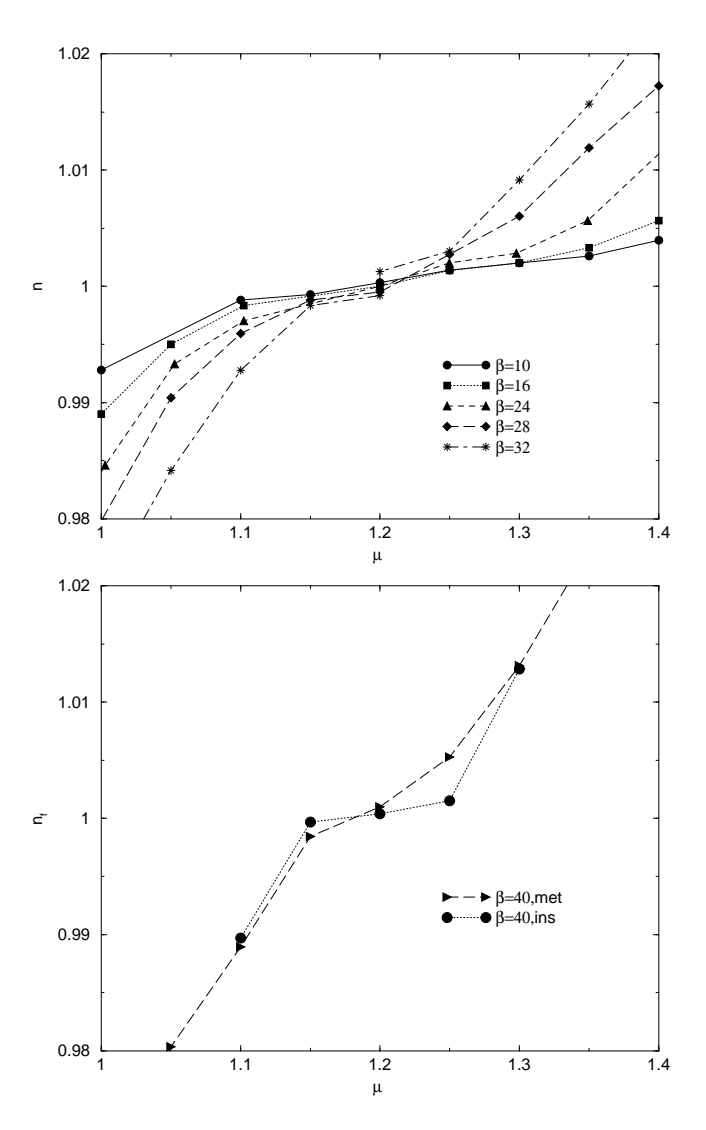


Figure 2.10: Particle occupation n function of μ for different temperatures in the 2-band model at U=3.0. The top panel shows curves with $T > T_{MIT}$ and in the bottom panel we have $T < T_{MIT}$.

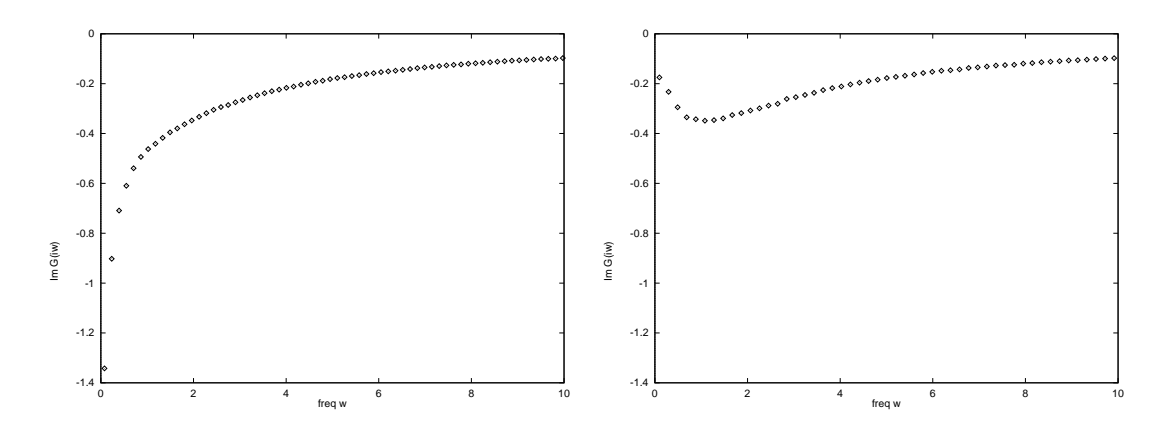


Figure 2.11: Left: Metallic seed obtained from U=2.8. Right: Insulating seed obtained from U=3.5

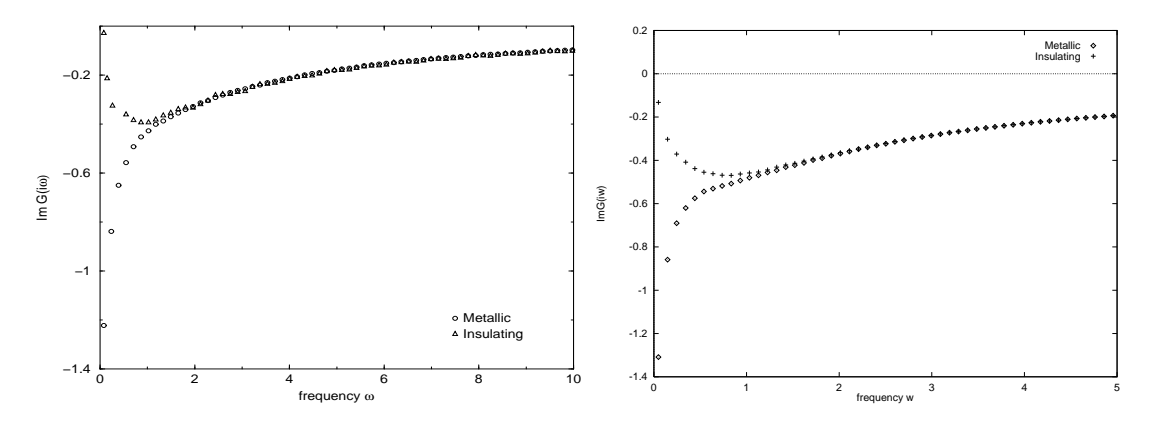


Figure 2.12: Metallic and insulating Green's function for U=3.0 , $\beta=40({\rm left})$ and $\beta=64({\rm right})$

2.4.3 Convergence of solutions

We present a few technical details regarding the stability of the solutions, especially near a phase boundary. To determine the convergence of the self-consistent solutions, we examined the difference in the imaginary part of the self energy at the first Matsubara frequency $Im\Sigma(\omega)$ as $\omega \to 0$ between two successive iterations i. The iterations were halted when this difference $||Im\Sigma^{i+1}(\omega \to 0) - Im\Sigma^{i}(\omega \to 0)||$ became smaller than a threshold.

If we are away from the coexistence region, the solution converges in 12–15 iterations

when the initial guess is close to the solution. At a lower value of U where there is only one solution, the Green's function converges in ~ 20 iterations even with an initial guess far from the true solution. Each DMFT iteration consists of 100000 Monte Carlo sweeps. However, close to the coexistence region, the number of iterations required for convergence becomes large. At the boundaries of the region, the number of iterations is expected to become very large due to critical slowing down.

The convergence of the metallic Green's function in Fig. 2.12 at $U = 3.0, \mu = 1.225$ starting from the metallic seed is shown in Fig. 2.13(left). The convergence of the insulating Green's function in Fig.2.12 is shown in Fig. 2.13(right).

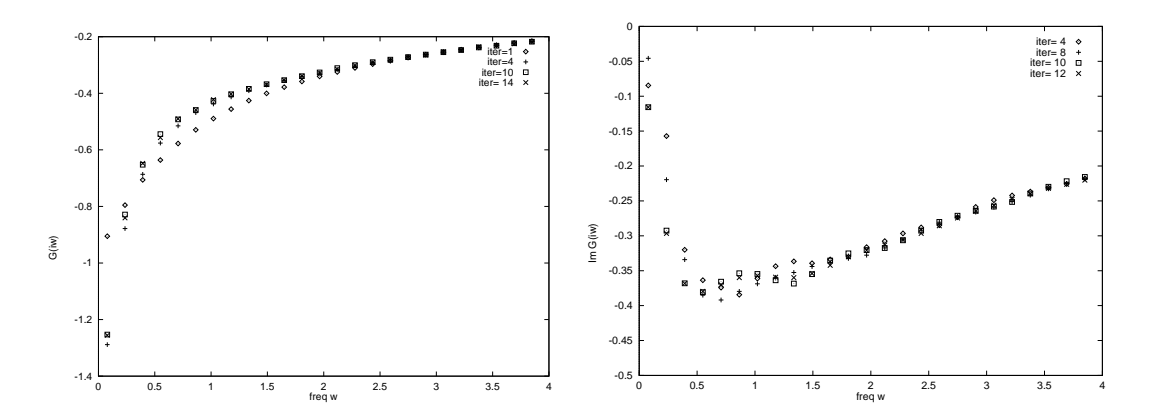


Figure 2.13: Convergence of metallic (left) and insulating (right) Green's function

2.4.4 Compressibility divergence

From the n_f - μ curves, we compute the numerical derivative of the particle number with respect to chemical potential, which is proportional to the compressibility. In the case of the finite temperature doping driven MIT, we observe a divergence in compressibility as we approach the second order transition point [44].

Fig. 2.14 shows the behavior of $\kappa = \Delta n/\Delta \mu$ as a function of μ and T for U=4.0 in the 1-band model. We can see that near $\mu = 1.07$, which we identify as μ_{c1} , κ increases rapidly indicating a divergence near the phase boundary where the insulating solution disappears. (Figs. 2.15 shows that as temperature is decreased κ^{-1} decreases rapidly indicating a divergent compressibility as we pass through the MIT. The data for κ^{-1}

as a function of T was fitted to a power law. It was found that a power law type of behavior $\kappa^{-1} \sim (T - T_c)^b$ with $b \sim 0.33$ for U = 2.44. matches the data.

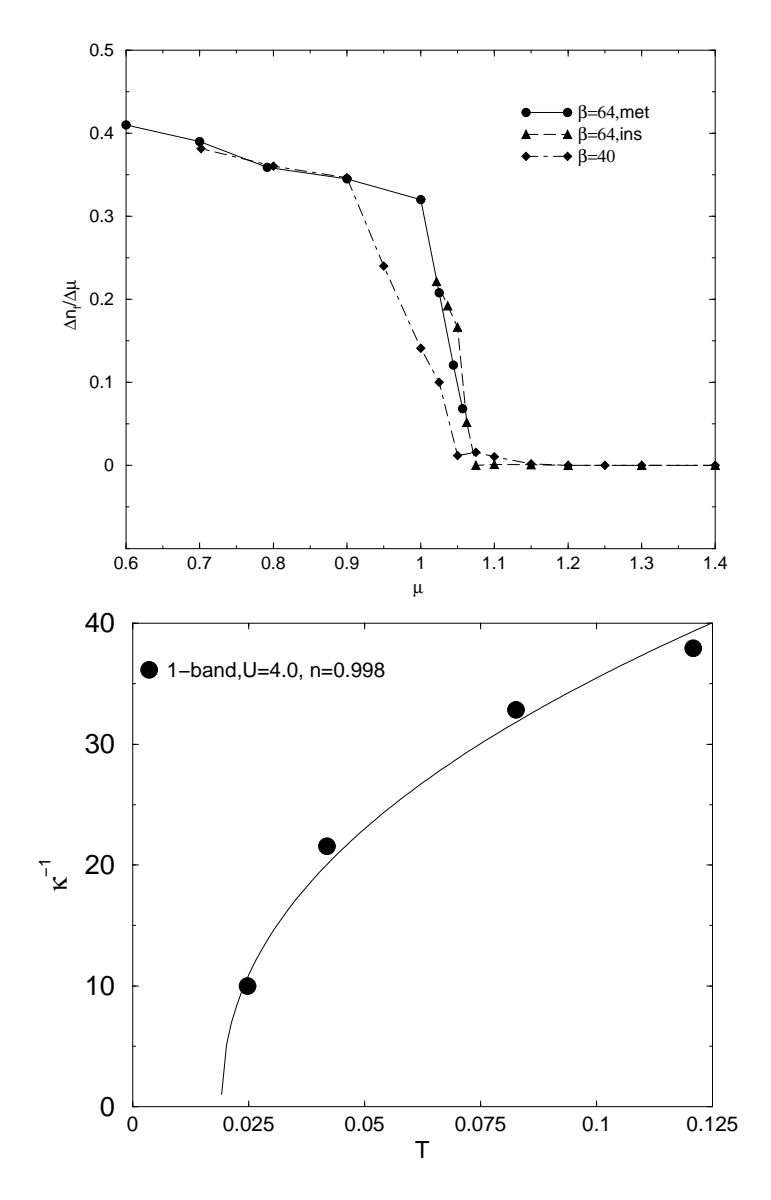


Figure 2.14: 1-band model, U=4.0. Top: Compressibility as a function of chemical potential. Bottom: Inverse compressibility $\kappa^{-1}=(dn/d\mu)^{-1}$ at U=4.0 in the 1-band model as a function of T. The solid line is the function $\kappa^{-1}\sim (T-T_C)^b$ with $b\sim 0.47$

2.5 Phase diagram

From the above numerical results we propose a schematic phase diagram for the Hubbard model, which for the 1-band case is shown in Fig. 2.16. The regions of

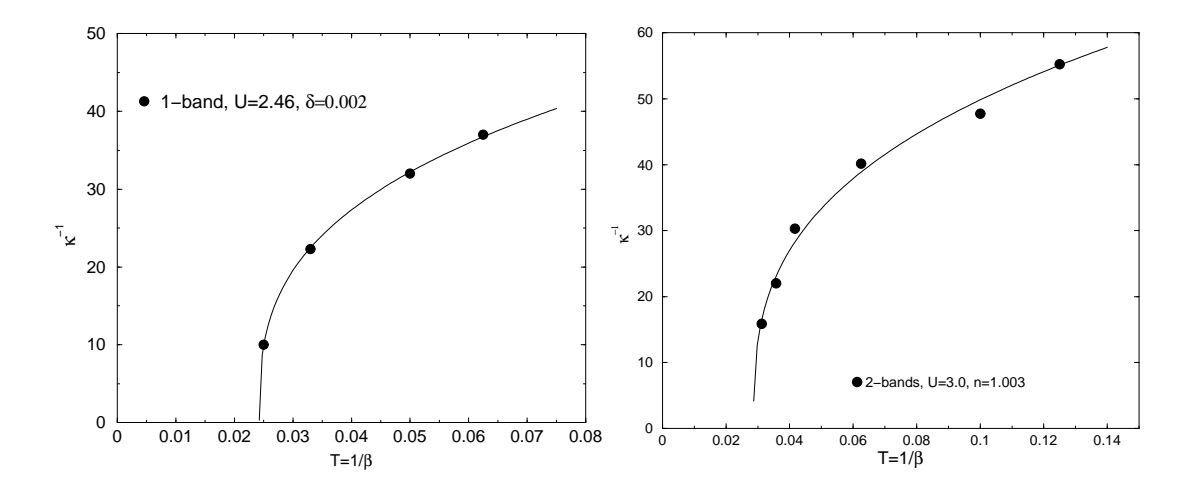


Figure 2.15: Left: Inverse compressibility $\kappa^{-1} = (dn/d\mu)^{-1}$ at U=2.46 in the 1-band model. The solid line is the function $\kappa^{-1} \sim (T - T_C)^b$ with $b \sim 0.33$. Right: κ^{-1} at a constant doping n = 1.003 as a function of T in the 2-band model. The solid line is a fit to a power law using the functional form $\kappa \approx (T - T_c)^b$ with the power $b \sim 1/3$. The intercept with the T-axis gives our estimate for $T_c = 0.0288$.

coexisting solutions are shown as cross sections of constant U in the (U, T, μ) parameter space. The μ -axis starts at zero doping, thus n=1 on the (U,T)-plane where $\tilde{\mu}=0$, which for the 1-band model is $\tilde{\mu}=\mu-U/2$. At larger values of U, the regions of coexisting solutions are two triangles, one for n<1 and the other for n>1. In the 1-band model, these triangular peaks are symmetric about $\mu=U/2$. These triangles are delimited by the $\mu_{c1}(T)$ and $\mu_{c2}(T)$ lines which correspond to the disappearance of the insulating and the metallic solutions respectively. As U decreases, the triangular regions approach each other and fully merge at $U=U_{MIT}$. Further lowering U makes the single triangular region diminish until $U=U_{c1}(T=0)$ where it vanishes.

The coexistence region in Fig. 2.7 curve at U=2.44 and $\beta=1/T=64$ near $\tilde{\mu}=0$ correspond to the region in Fig. 2.16 where $U_{MIT} < U < U_{c2}$. For the parameters in Fig. 2.7, we see that the metallic state exists all the way down to zero doping at $\tilde{\mu}=0$. This implies that for $U_{MIT} < U < U_{c2}$, the $\mu_{c2}(T)$ line does not go all the way to T=0 in contrast to the case when $U > U_{c2}$ (Fig. 2.9).

The interaction U = 4.0 is greater than U_{c2} in the 1-band model. Using our results for U = 4.0 and those obtained in [45], we can map out the part of the phase diagram

in Fig. 2.16 that corresponds to the parameter space where $U > U_{c2}$ and n < 1. In this case, at zero doping, only the insulating solution survives at low temperatures. The results are shown in Fig. 2.17.

The disappearance of the metallic or the insulating solutions is captured by the critical slowing down of the solutions as shown in Fig. 2.18. As we approach the phase boundaries of the coexistence region, it is seen that the number of QMC iterations required for the solutions to converge increase. In Fig. 2.18 it is seen that starting with the metallic solution at low doping, if we increase μ , the number of iterations needed for the metallic solution to converge diverges, indicating that we are near the μ_{c2} boundary. Similarly starting with the insulating solution near half-filling, if we decrease μ , i.e go far away from half-filling the number of iterations required for the convergence of the insulating solution diverges. This indicates that we are close to the μ_{c1} boundary.

The phase diagram for the 2-band model shown in Fig. 2.19. is qualitatively similar to the 1-band model except that the pairs of triangles at a given U do not have the same height due to absence of particle-hole symmetry. The n_f - μ curves in Fig. 2.10 correspond to the region in the phase diagram where $U_{MIT} < U_{<}U_{c2}$. As T is decreased, the curves show a crossover from small to large compressibility.

2.6 Discussion

A common feature that emerges from the model is that, in the regions where two mean-field solutions exist, the system has two different values of n for given T and μ . Furthermore, these two solutions have different free energies and the actual thermodynamic state of the system is that of minimum energy. Hence a jump in particle number is predicted at a first order line. The determination of this line implies a precise calculation of the free energy, which is technically difficult, and outside the scope of this work.

In the T- μ -U phase diagram, the two mean-field solutions exist within the triangular regions. A first order transition exists where the free energies cross. At finite T, this

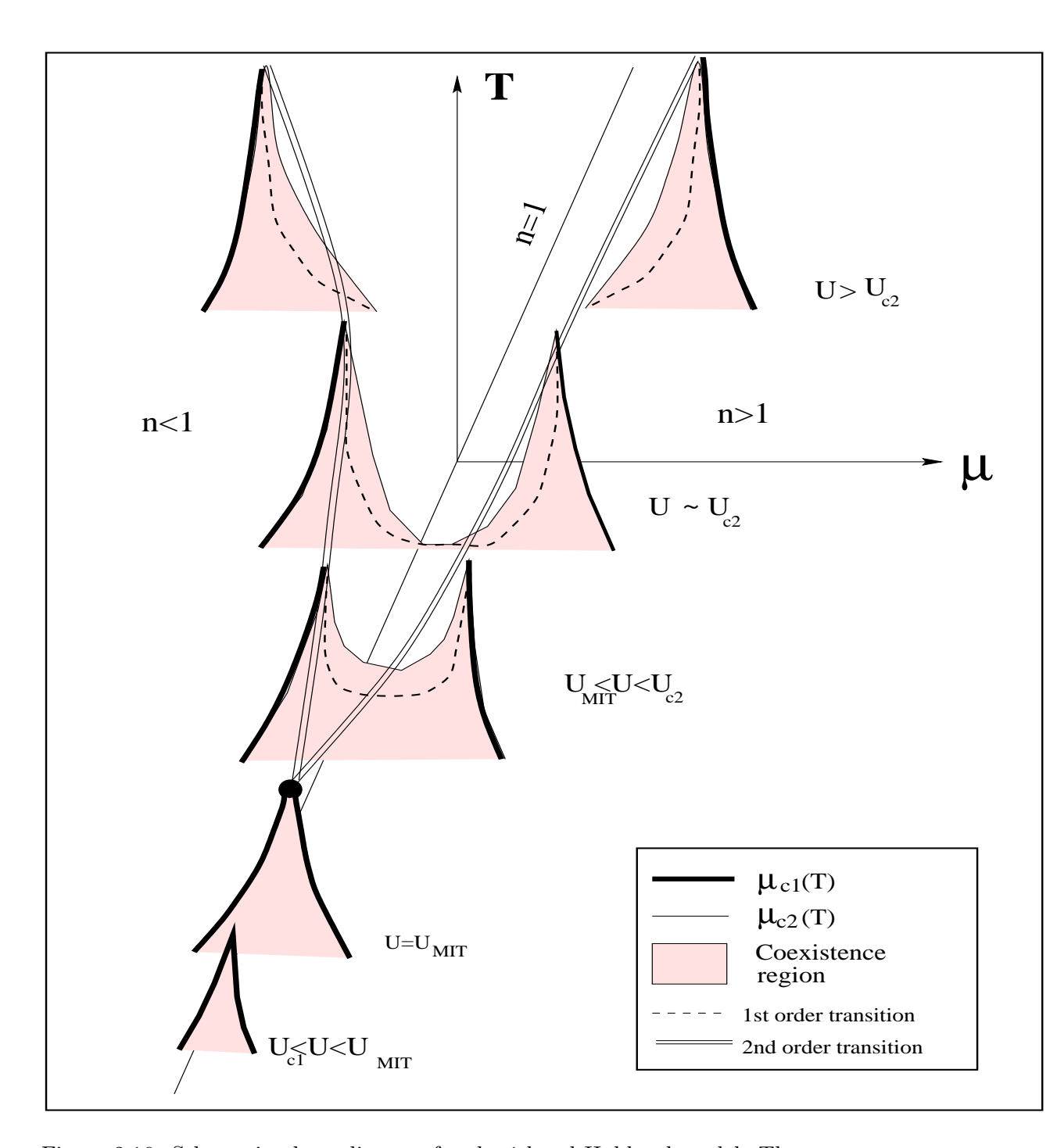


Figure 2.16: Schematic phase diagram for the 1-band Hubbard model. The cross sections are on the $T-\mu$ plane for different values of U with U increasing towards the top of the figure. The peaks are symmetric about $\mu=U/2$. μ_{c1} and U_{c1} are the chemical potential and interaction respectively below which the insulating solution does not survive. μ_{c2} and U_{c2} are those above which the metallic solution does not exist. The black circle denotes the second order transition point (U_{MIT}, T_{MIT}) at n=1. The shaded regions denote the coexistence region between metallic and insulating phases.

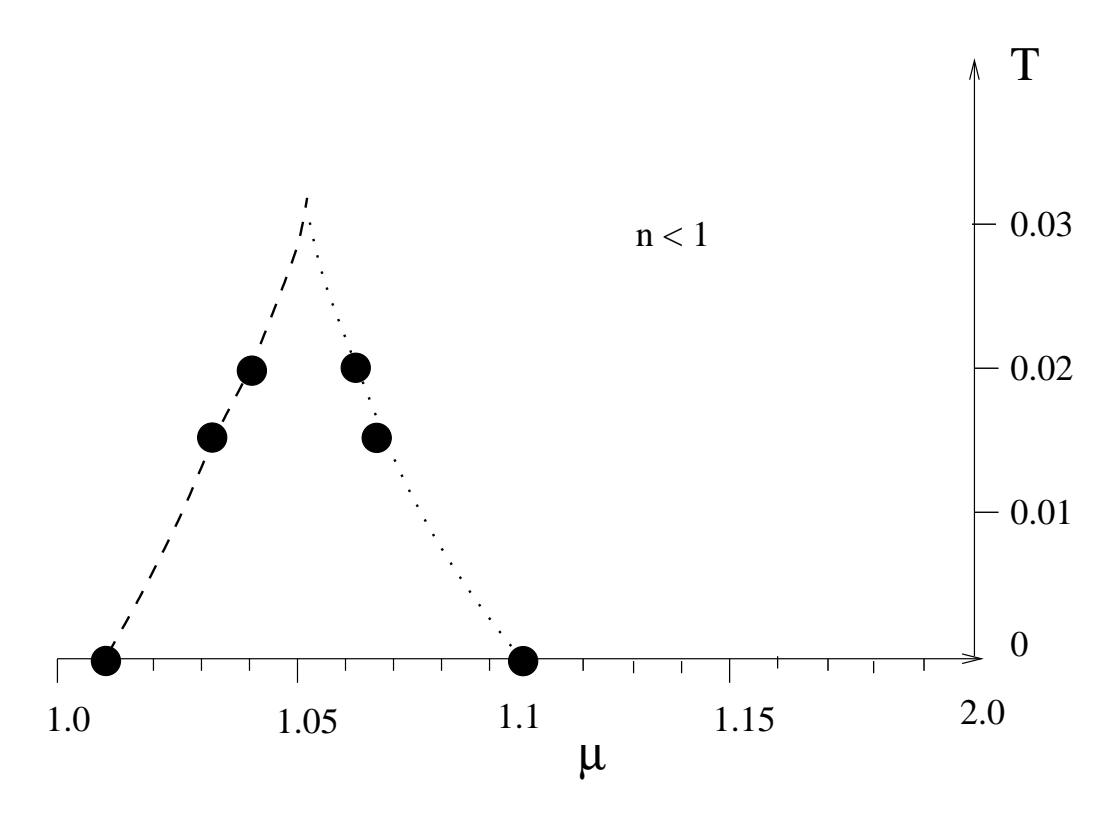


Figure 2.17: Phase diagram for U=4.0. The black circles denote are obtained from QMC simulations. The dashed and the dotted lines denote μ_{c1} and μ_{c2} lines respectively.

leads to a first order transition surface between an insulating and a metallic-like state. The intersections of this surface with the constant U cross sections are first order lines that we denote by dashed lines in Fig. 2.16. At T=0 within the coexistence regions, i.e. the base of the triangles, the metallic state is always stable, thus one can cross the first-order surface towards the insulator by either increasing T or changing the chemical potential.

At finite T, the two solutions merge where the triangular regions end. Hence there is a line of second order transitions where the first order surface ends (thick double-line in Fig. 2.16. The doping is small but non-zero along this line except at $U = U_{MIT}$. Our numerical results show a divergence of compressibility on this line of second order transitions. The idea of divergent compressibility at the Mott endpoint has been shown to arise from general Landau theory arguments [46].

From the experimental viewpoint, we believe that our results highlight important

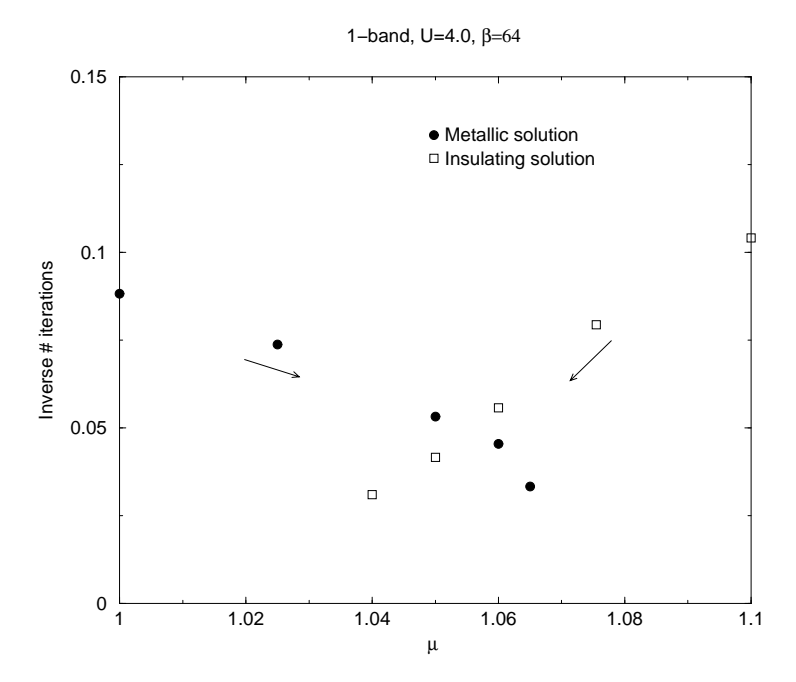


Figure 2.18: Critical slowing down observed in the vicinity of μ_{c1} and μ_{c2} for the 1-band model at $U=4.0, \beta=64$. The inverse number of iterations required for the metallic solution to converge goes to zero as we near μ_{c2} and those of the insulating solution to converge goes to zero as we approach μ_{c1} . The arrows indicate the directions in which the boundaries were approached.

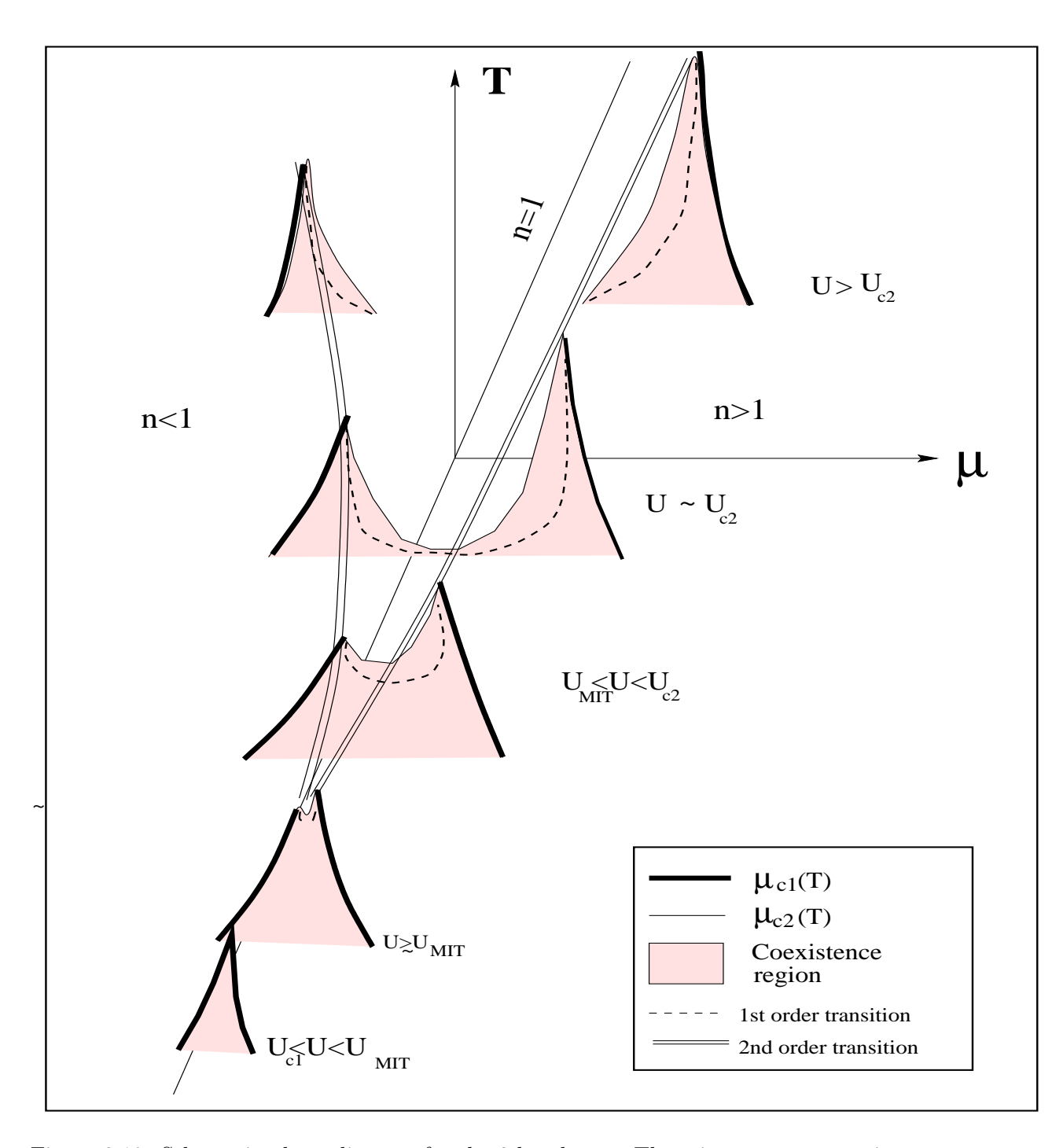


Figure 2.19: Schematic phase diagram for the 2-band case. There is an asymmetry in the triangular peaks as compared to the 1-band case. The cross sections are on the $T-\mu$ plane for different values of U as before. μ_{c1} and U_{c1} are the chemical potential and interaction respectively below which the insulating solution does not survive. μ_{c2} and U_{c2} are the chemical potential and interaction above which the metallic solution does not exist. U_{MIT} is the value of the interaction at which the metal-insulator transition takes place. The shaded portions are the regions of coexistence between the metallic and the insulating solutions.

aspects in the α - γ transition in Ce. The divergence of compressibility in the Ce α - γ transition has an electronic origin and can be understood from model calculations. The decrease in compressibility that we found during the transition from the insulating to the metallic phase is similar to what has been measured by Beecroft and Swenson [30].

2.7 Summary

We have shown that within the dynamical mean-field theory of the Hubbard model, there is a region where the paramagnetic metallic and paramagnetic insulating phases coexist. We have explored the coexistence region for the 1-band Hubbard model both at the particle-hole symmetric point and away from it. For the 2-band Hubbard model we have studied the region in phase space near the occupation number $n_f = 1$. We calculated the compressibility from the n_f versus μ curve. We find numerical evidence for a divergent compressibility near the finite temperature Mott endpoint. Based on our numerical studies we have proposed a phase diagram for the doped 1- and 2-band Hubbard model. Our results are relevant to the Ce α - γ transition.

Chapter 3

Density Functional Theory, LDA, LDA+U and LDA+DMFT

In this chapter, we first briefly review the density functional theory (DFT) local density approximation (LDA). We then discuss methods that go beyond the LDA to tackle strongly correlated systems: LDA+U and LDA+DMFT. We also discuss the structure of the LMTART program that is based on DFT methods.

3.1 Density functional theory

3.1.1 LDA

Density functional theory is a powerful tool to study weakly interacting systems. It is the basis of the LDA and the LDA+U methods which are used to calculate the band structures of materials. A brief description of DFT from the effective action point of view is presented here [8], [9], [47].

Consider a fermionic system that is coupled to an external source J(x). The Hamiltonian is

$$H = H_0 + \int dx^3 \psi^{\dagger}(\mathbf{x}) J(\mathbf{x}) \psi(\mathbf{x})$$
 (3.1)

where H_0 is the Hamiltonian without the source. The partition function is

$$Z = \exp[-W[J]] = \int D[\psi\psi^{\dagger}] \exp - \int dt L$$
 (3.2)

where L is the Lagrangian.

For the system consists of electrons moving in a crystal potential $V_c(x)$ and interacting via Coulomb interactions V, in the presence of an external source J coupled to

the electron density, the partition function is

$$Z = \int D[\psi\psi^{\dagger}] \exp\left[-\int dx \psi^{\dagger}(x) \left[\partial_{\tau} - \frac{\nabla^{2}}{2m}\right] dx dx' \psi^{\dagger}(x) \psi^{\dagger}(x') V(x - x') \psi(x') \psi(x) - J(x) \psi^{\dagger}(x) \psi(x)\right]$$

$$(3.3)$$

Here $x = (\mathbf{x}, \tau)$ denotes the space–imaginary time coordinates. By performing a Legendre transform of Γ we can eliminate the potential in favor of the density ρ .

$$\Gamma[\rho] = W[J] - \int J(x)\rho(\mathbf{x}) \tag{3.4}$$

The minimum of this functional gives the true density and the total energy.

To construct approximations to the functional Γ it is very useful to introduce the Kohn–Sham potential, V_{KS} , which is defined as the potential such that when added to the non–interacting kinetic energy, it produces the given density in a reference system of non–interacting particles . i.e.

$$\rho(\mathbf{r}) = T \sum_{\sigma} \sum_{i\omega_n} \langle \sigma \mathbf{r} \left| (i\omega_n + \nabla^2/2 - V_{KS})^{-1} \right| \sigma \mathbf{r} \rangle e^{i\omega_0 +}$$
(3.5)

The exact functional can now be viewed as a functional of two variables

$$\Gamma(\rho, V_{KS}) = -T \sum_{i\omega_n} tr \log[i\omega_n + \nabla^2/2 - V_{KS}] - \int V_{KS}(\mathbf{r})\rho(\mathbf{r})d\mathbf{r} + \frac{1}{2} \int \frac{\rho(\mathbf{r})\rho(\mathbf{r}')}{|\mathbf{r} - \mathbf{r}'|} d\mathbf{r} d\mathbf{r}' + \int V_{ext}(\mathbf{r})\rho(\mathbf{r})d\mathbf{r} + E_{xc}[\rho]$$
(3.6)

 $\Gamma(\rho)$ is obtained by substituting $V_{KS}(\rho)$ obtained by solving eqn.(3.5) (which makes eqn.(3.6) stationary) into $\Gamma(\rho, V_{KS})$. $E_{xc}[\rho]$ is the exchange–correlation energy which is a functional of the density and not of the external potential.

Extremizing eqn. (3.6) with respect to ρ gives

$$V_{KS}(\mathbf{r})[\rho] = \int \frac{\rho(\mathbf{r}')d\mathbf{r}'}{|\mathbf{r} - \mathbf{r}'|} + V_{xc}(\mathbf{r})[\rho] + V_{ext}(\mathbf{r})[\rho]$$
(3.7)

where $V_{xc}(\mathbf{r})$ is the exchange-correlation potential obtained as

$$\frac{\delta E_{xc}}{\delta \rho(\mathbf{r})} \equiv V_{xc}(\mathbf{r}) \tag{3.8}$$

If we restrict ourselves to zero–temperature and interpret the Fermi functions as step functions. Eqn. (3.5) can be rewritten as

$$[-\nabla^2/2 + V_{KS}(\mathbf{r})]\psi_{\mathbf{k}j}(\mathbf{r}) = \epsilon_{\mathbf{k}j}\psi_{\mathbf{k}j}(\mathbf{r})$$
(3.9)

$$\rho(\mathbf{r}) = \sum_{\mathbf{k}j} f(\epsilon_{\mathbf{k}j}) \psi_{\mathbf{k}j}^*(\mathbf{r}) \psi_{\mathbf{k}j}(\mathbf{r})$$
(3.10)

and V_{KS} is given as an explicit function of the density.

The total energy of the crystal is given as

$$E_{tot} = \sum_{\mathbf{k}j} f(\epsilon_{\mathbf{k}j}) \epsilon_{\mathbf{k}j} + \frac{1}{2} \int \frac{\rho(\mathbf{r})\rho(\mathbf{r}')}{|\mathbf{r} - \mathbf{r}'|} d\mathbf{r} d\mathbf{r}' + \int V_{ext}(\mathbf{r})\rho(\mathbf{r}) d\mathbf{r} + \int \epsilon_{xc} [\rho(\mathbf{r})]\rho(\mathbf{r}) d\mathbf{r} + E_{dc}$$
(3.11)

where

$$E_{dc} = -\int V_{KS}(\mathbf{r})\rho(\mathbf{r})d\mathbf{r}$$
(3.12)

simply subtracts the interaction energy from the Kohn–Sham eigenvalues which are explicitly included in the Hartree and exchange–correlation term to avoid double counting.

Since $E_{xc}[\rho]$ is not known explicitly, this method is useful only because of successful approximations to the exchange energy. In the Local Density Approximation (LDA) the exchange energy functional is assumed to be local:

$$E_{xc}[\rho] = \int \epsilon_{xc}[\rho(\mathbf{r})]\rho(\mathbf{r})d\mathbf{r}$$
(3.13)

with $\epsilon_{xc}[\rho(\mathbf{r})]$ being the energy density of the uniform electron gas.

Here $\rho(\mathbf{r})$ is uniquely expressed in terms of the orbitals $\psi_{\mathbf{k}j}(\mathbf{r})$. In order to truncate the DFT, we introduce a finite basis set $\chi_{\alpha}^{\mathbf{k}}(\mathbf{r})$ and expand

$$\psi_{\mathbf{k}j}(\mathbf{r}) = \sum_{\alpha} \chi_{\alpha}^{\mathbf{k}}(\mathbf{r}) A_{\alpha}^{\mathbf{k}j} \tag{3.14}$$

keeping a finite set of α . This truncation restricts the active part of the multiplicative operator associated with the potential V_{KS} to have a form

$$\hat{V} = \sum_{\mathbf{k}} |\chi_{\alpha}^{\mathbf{k}}\rangle V_{\alpha\beta} \langle \chi_{\alpha}^{\mathbf{k}}| \tag{3.15}$$

For a known potential V_{KS} this construction can be done once and for all. However, since V_{KS} depends on the density, the basis $|\chi_{\alpha}^{\mathbf{k}}\rangle$ is adapted iteratively to the self-consistent solution.

3.1.2 LDA+U

The LDA method is not very successful when strong electron correlations are present as the electrons are localized due to the interactions. The LDA+U method [14], [15]

is a technique that is proposed when strong correlations are present in the system. For simplicity we will deal with spin unrestricted formalism so that the total energy is invariant with respect to orientation. This allows us to choose a specific quantization axis.

We introduce a set of localized orbitals $\phi_a(\mathbf{r} - \mathbf{R})$ which are used to build an occupancy matrix. If ϕ_a are identified with the correlated electrons, we can represent the correlated part of the electron density by

$$n_{ab}^{\sigma} = \sum_{\mathbf{k}j} f(\epsilon_{\mathbf{k}j\sigma}) \int \psi_{\mathbf{k}j\sigma}^{*}(\mathbf{r}) \phi_{a}(\mathbf{r}) d\mathbf{r} \int \psi_{\mathbf{k}j\sigma}(\mathbf{r}') \phi_{b}^{*}(\mathbf{r}') d\mathbf{r}'$$
(3.16)

The total energy is now a functional of $\rho(\mathbf{r})$ and of n_{ab}^{σ} . The LDA+U functional is

$$\Gamma_{LDA+U}[n_{ab}^{\sigma}, \lambda_{ab}^{\sigma}, V_{KS}^{\sigma}, \rho^{\sigma}] = -T \sum_{i\omega_{n}} tr \log[i\omega_{n} + \nabla^{2}/2 - V_{KS}^{\sigma} - \sum_{ab} \lambda_{ab}^{\sigma} \phi_{a}(\mathbf{r}) \phi_{b}^{*}(\mathbf{r}')]$$

$$- \sum_{\sigma} \int V_{KS}^{\sigma}(\mathbf{r}) \rho^{\sigma}(\mathbf{r}) d - \sum_{\sigma} \sum_{ab} \lambda_{ab}^{\sigma} n_{ab}^{\sigma} + \frac{1}{2} \int \frac{\rho(\mathbf{r}) \rho(\mathbf{r}')}{|\mathbf{r} - \mathbf{r}'|} d\mathbf{r} d\mathbf{r}'$$

$$+ E_{xc}^{LDA}[\rho^{\sigma}] + E^{Model}[n^{\sigma}] - E_{dc}[n^{\sigma}]$$
(3.17)

where λ_{ab}^{σ} are Lagrange multipliers.

$$E^{Model}[n^{\sigma}] = \frac{1}{2} \sum_{\sigma} \sum_{abcd} U_{abcd} n_{ab}^{\sigma} n_{cd}^{-\sigma} + \frac{1}{2} \sum_{\sigma} \sum_{abcd} (U_{abcd} - J_{abcd}) n_{ab}^{\sigma} n_{cd}^{\sigma}$$
(3.18)

is the contribution from the Coulomb energy in the shell of correlated electrons. $E_{dc}[n^{\sigma}]$ is the double-counting term which is subtracted as part of the energy in E^{Model} has been taken into account in the LDA part.

The form of the double counting term [14] used here is

$$E_{dc} = \frac{1}{2}\bar{U}\bar{n}(\bar{n}-1) - \frac{1}{2}\bar{J}[\bar{n}^{\uparrow}(\bar{n}^{\uparrow}-1) + \bar{n}^{\downarrow}(\bar{n}^{\downarrow}-1)]. \tag{3.19}$$

where

$$\bar{U} = \frac{1}{(2l+1)^2} \sum_{ab} \langle ab | \frac{1}{r} | ab \rangle \tag{3.20}$$

$$\bar{J} = \bar{U} - \frac{1}{2l(2l+1)} \sum_{ab} (\langle ab | \frac{1}{r} | ab \rangle - \langle ab | \frac{1}{r} | ba \rangle)$$
(3.21)

Here $\bar{n}^{\sigma} = \sum_{a} n_{aa}^{\sigma}$, and $\bar{n} = \bar{n}^{\uparrow} + \bar{n}^{\downarrow}$.

We get the self-consistency equations by extremizing the functional with respect to V_{KS} .

$$\rho^{\sigma}(\mathbf{r}) = T \sum_{i\omega_n} \left\langle \mathbf{r} \left| \left[i\omega_n + \nabla^2/2 - V_{KS}^{\sigma} - \sum_{ab} \lambda_{ab}^{\sigma} \phi_a(\mathbf{r}) \phi_b^*(\mathbf{r}') \right]^{-1} \right| \mathbf{r} \right\rangle e^{i\omega_n 0^+} = \sum_{\mathbf{k}j} f(\epsilon_{\mathbf{k}j\sigma}) |\psi_{\mathbf{k}j\sigma}(\mathbf{r})|^2$$
(3.22)

with

$$[-\nabla^2/2 + V_{KS}^{\sigma} + \sum_{ab} \lambda_{ab}^{\sigma} \phi_a(\mathbf{r}) \phi_b^*(\mathbf{r}')] \psi_{\mathbf{k}j\sigma} = \epsilon_{\mathbf{k}j\sigma} \psi_{\mathbf{k}j\sigma}$$
(3.23)

 V_{KS}^{σ} is obtained by extremizing the functional w.r.t. $\rho(\mathbf{x})$:

$$V_{KS}(\mathbf{r})[\rho] = \int \frac{\rho(\mathbf{r}')d\mathbf{r}'}{|\mathbf{r} - \mathbf{r}'|} + V_{xc}(\mathbf{r})[\rho] + V_{ext}(\mathbf{r})[\rho]$$
(3.24)

We get the correction to the potential λ_{ab}^{σ} by extremizing the functional w.r.t. n_{ab}^{σ}

$$\lambda_{ab}^{\sigma} = \sum_{cd} U_{abcd} n_{cd}^{-\sigma} + \sum_{cd} (U_{abcd} - J_{abcd}) n_{cd}^{\sigma} - \frac{dE_{dc}[n^{\sigma}]}{dn_{ab}^{\sigma}}$$
(3.25)

The double counting term generates the correction to the potential in the form:

$$\lambda_{ab}^{\sigma} = \sum_{cd} U_{abcd} n_{cd}^{-\sigma} + \sum_{cd} (U_{abcd} - J_{abcd}) n_{cd}^{\sigma} - \bar{U}(\bar{n} - \frac{1}{2}) + J(\bar{n}^{\sigma} - \frac{1}{2})$$
 (3.26)

The interaction matrices are defined as:

$$U_{abcd} = \langle ac | \frac{1}{r} | bd \rangle = \int_{a}^{*} \phi_{a}(\mathbf{r}) \phi_{c}^{*}(\mathbf{r}') v_{C}(\mathbf{r} - \mathbf{r}') \phi_{b}(\mathbf{r}) \phi_{d}(\mathbf{r}') d\mathbf{r} d\mathbf{r}'$$
(3.27)

$$J_{abcd} = \langle ac | \frac{1}{r} | db \rangle = \int_{a}^{*} \phi(\mathbf{r}) \phi_{c}^{*}(\mathbf{r}') v_{C}(\mathbf{r} - \mathbf{r}') \phi_{d}(\mathbf{r}) \phi_{b}(\mathbf{r}') d\mathbf{r} d\mathbf{r}'$$
(3.28)

where $\phi(\mathbf{r})$ are the set of projectors and $v_c(\mathbf{r} - \mathbf{r}')$ is the Coulomb interaction that has to take into account the effects of screening by conduction electrons.

These matrices are expressed in terms of Slater integrals. Representing $\phi_{lm}(\mathbf{r}) = \phi_l(r)i^lY_{lm}(\hat{r})$ and for $a \equiv lm, b \equiv lk, c \equiv l'm', d \equiv l'k'$ we can express U and J as

$$\langle lml'm'|\frac{1}{r}|lkl'k'\rangle = \sum_{l''=0,2,\dots}^{\min(2l,2l')} \frac{4\pi}{2l''+1} F_{ll'}^{(u)l''vv} C_{lklm}^{l''m''=m-k} C_{l'm'l'k'}^{l''m''=k'-m'} \delta_{k'-m',m-k}$$
(3.29)

$$\langle lml'm'|\frac{1}{r}|l'k'lk\rangle = \sum_{l''=0.2}^{\min(2l,2l')} \frac{4\pi}{2l''+1} F_{ll'}^{(j)l''} C_{l'k'lm}^{l''m''=m-k'} C_{l'm'lk}^{l''m''=k-m'} \delta_{m-k',k-m'}$$
(3.30)

where the quantities $F^{(u)}$ and $F^{(j)}$ are given by the following radial integrals

$$F_{ll'}^{(u)l''} = \int \frac{r^{l''}}{r'^{l''+1}} \phi_l^2(r) \phi_{l'}^2(r') dr dr'$$
(3.31)

$$F_{ll'}^{(j)l''} = \int \frac{r^{l''}}{r'^{l''+1}} \phi_l(r) \phi_{l'}(r) \phi_l(r') \phi_{l'}(r') dr dr'$$
(3.32)

If l=l', $F^{(u)}$ and $F^{(j)}$ are equal and are reduced to constants. For d-electrons, there are three constants $F^{(0)}$, $F^{(2)}$, $F^{(4)}$ and for f-electrons, there are four constants $F^{(0)}$, $F^{(2)}$, $F^{(4)}$, $F^{(6)}$. The Slater integrals can be linked to U and J via $U=F^{(0)}$ and $J=(F^{(2)}+F^{(4)})/14$ for d-electrons with $F^{(2)}/F^{(4)}=0.625$. For f-electrons, $U=F^{(0)}$ and $J=(286F^{(2)}+194F^{(4)}+250F^{(6)})/6435$.

3.1.3 LDA+DMFT method

In the LDA+U method, the Coulomb interaction in eqn.(3.18) are treated in a Hartree-Fock approximation, thus it fails to describe the many body nature of the electron-electron interaction in strongly correlated materials. Also, in the LDA+U method, we do a Legendre transformation with respect to a part of the density, which lacks a clear physical significance. A method that has been developed to treat correlated materials, is LDA combined with the Dynamical Mean-Field Theory (DMFT). The DMFT has been an extremely successful method to treat model Hamiltonians that describe materials with strong correlations. However, the model Hamiltonians used have parameters. By combining LDA+DMFT, we would like to introduce microscopic details to the approach and make the calculation first-principles [47].

The following section contains a brief description of the LDA+DMFT method from an effective action point of view [13,48].

In DMFT, we deal with functionals of the local Green's function, which is a well defined object. We start with the LDA+DMFT functional $\Gamma_{LDA+DMFT}$ (ρ, V_{KS}, χ, A)

which has the form

$$\Gamma_{LDA+DMFT}(\rho, V_{KS}, \chi, A) = -T \sum_{i\omega_n} tr \log[i\omega_n + \nabla^2/2 - V_{KS} - \Sigma_{ab}(i\omega_n)\phi_a(\mathbf{r})\phi_b^*(\mathbf{r}')] - \int V_{KS}(\mathbf{r})\rho(\mathbf{r})d\mathbf{r} - \sum_{i\omega_n} \sum_{ab} \Sigma_{ab}(i\omega_n)A_{ba}(i\omega_n) + \int V_{ext}(\mathbf{r})\rho(\mathbf{r})d\mathbf{r} + \frac{1}{2} \int \frac{\rho(\mathbf{r})\rho(\mathbf{r}')}{|\mathbf{r} - \mathbf{r}'|}d\mathbf{r}d\mathbf{r}' + E_{xc}^{LDA}[\rho] + \sum_{j} \Phi[A_{ab}(j, i\omega)] + \Phi_{DC}$$
(3.33)

 Φ is the sum of all two–particle irreducible graphs constructed with the local part of the interaction—and Φ_{DC} is taken to have the same form as in LDA+U method as described later.

In a fixed tight–binding basis, $-\nabla^2 + V_{KS}$ reduces to $H^{TB}(\mathbf{k})$. The functional $\Gamma_{LDA+DMFT}$ for a fixed density and truncated to a finite basis set takes the form of the DMFT functional

$$\Gamma[A[\Delta], \chi[\Delta]] =$$

$$W_0[\Delta] - Tr \log A - \sum_{\mathbf{k}} \sum_{i\omega_n} Tr \log[i\omega_n - \epsilon(\mathbf{k}) - \chi] - \sum_{i\omega_n} [\chi - i\omega_n + \bar{\epsilon} + \Delta] A \quad (3.34)$$

Its minimization leads to the set of equations with Kohn–Sham potential as in the LDA method, and

$$\Sigma_{ab}(i\omega_n) = \frac{\delta\Phi}{\delta A_{ab}(i\omega_n)} + \epsilon_{ab}^{DC}$$
(3.35)

which identifies Σ as a self–energy of a generalized Anderson impurity model in a bath characterized by a matrix of levels

$$\epsilon_{ab}^{0} = \epsilon_{ab}^{DC} + \sum_{\mathbf{k}} H_{ab}^{TB}(\mathbf{k}) \tag{3.36}$$

and a hybridization function $\Delta_{ab}(i\omega_n)$ obeying a self-consistency condition

$$i\omega O_{ab} - \epsilon_{ab}^0 - \Delta_{ab}(i\omega_n) = \Sigma_{ab}(i\omega_n) + \left[\sum_k (i\omega_n O - \epsilon^0 - t(\mathbf{k}) - \Sigma(i\omega_n))^{-1}\right]^{-1}$$
(3.37)

Finally, minimizing eqn.(3.33) with respect to V_{KS} indicates that $\rho(\mathbf{r})$ should be computed as

$$\rho(\mathbf{r}) = T \sum_{i\omega_n} \left\langle \mathbf{r} \left| \left[i\omega_n + \nabla^2/2 - V_{KS} - \sum_{ab} \Sigma_{ab}(i\omega_n) \phi_a(\mathbf{r}) \phi_b^*(\mathbf{r}') \right]^{-1} \right| \mathbf{r} \right\rangle e^{i\omega_n 0^+}$$
 (3.38)

which as indicated before, when truncating in a fixed set of orbitals becomes

$$\rho(\mathbf{r}) = T \sum_{i\omega_n} \chi_{\alpha}(\mathbf{r}) \left[(i\omega_n - H^{TB}(\mathbf{k}) - \Sigma(i\omega_n)) \right]^{-1} \chi_{\beta}^*(\mathbf{r})$$
(3.39)

We express the functional in terms of the Weiss field, i.e. the hybridization function that added to the atom produces the exact spectral function. This allows us to eliminate the functional Φ . We can express the LDA+DMFT functional as:

$$\Gamma_{LDA+DMFT}(\rho, V_{KS}, \chi, A, \Delta) = -Tr \log[i\omega_n + \nabla^2/2 - V_{KS} - \Sigma_{ab}(i\omega_n, \mathbf{r}, \mathbf{r}')(\chi)] - \int V_{KS}(\mathbf{r})\rho(\mathbf{r})d\mathbf{r} - \sum_{i\omega_n} \sum_{ab} tr[\Sigma_{ab}(i\omega_n)A_{ba}(i\omega_n)] + \int V_{ext}(\mathbf{r})\rho(\mathbf{r})d\mathbf{r} + \frac{1}{2} \int \frac{\rho(\mathbf{r})\rho(\mathbf{r}')}{|\mathbf{r} - \mathbf{r}'|} d\mathbf{r} d\mathbf{r}' + E_{xc}^{LDA}[\rho] + \Phi_{DC} + W_{at}[\Delta[A]] - Tr \Delta[A]A - Tr \log A + Tr A_{at}^{-1} A$$
(3.40)

Here

$$\Sigma_{ab}(i\omega_n, \mathbf{r}, \mathbf{r}')(\chi) = \frac{1}{N_s} \sum_{\alpha\beta R_n R_l R_q} \chi_{\alpha}(\mathbf{r} - \mathbf{R}_p) O^{-1}(R_p - R_l)_{\alpha c} \chi_{cc"}(i\omega_n) O^{-1}(R_l - R_q)_{c\beta} \chi_{\beta}^*(\mathbf{r} - \mathbf{R}_q)$$

where N_s is the number of lattice sites and $W_{at}[\Delta]$ is simply the free energy of the atom (described by the atomic Hamiltonian h_{at}) in the presence of a hybridization field.

$$S_{at}[\Delta] = \int_{\tau,\tau'} \sum_{i,\sigma} c_{i\sigma}^{+l}(\tau) \left[\delta(\tau - \tau') \frac{\partial}{\partial \tau'} + \Delta^{lm}(\tau - \tau') \right] c_{i\sigma}^{m}(\tau') + \int d\tau h_{at}$$
 (3.41)

$$W_{at}[\Delta] = -\log \int dc^{+} dc \ e^{-S_{at}[\Delta] - \sum_{ab} \int_{ab} \Delta(\tau, \tau') c_{a}^{+}(\tau) c_{b}(\tau') d\tau d\tau'}$$

$$(3.42)$$

$$\Phi_{dc}^{Model} = \frac{1}{2} \bar{U} \bar{n} (\bar{n} - 1) - \frac{1}{2} \bar{J} [\bar{n}^{\uparrow} (\bar{n}^{\uparrow} - 1) + \bar{n}^{\downarrow} (\bar{n}^{\downarrow} - 1)]. \tag{3.43}$$

with U and J as defined in eqns. (3.20) and (3.21).

Here $\bar{n}^{\sigma} = \sum_{a} n_{aa}^{\sigma}$, and $\bar{n} = \bar{n}^{\uparrow} + \bar{n}^{\downarrow}$. n in this case should be viewed as a functional of the local Greens function $n = trA = T\sum_{\omega_n,a} e^{i\omega_n} A(i\omega_n)_{aa}$

This generates the correction to the potential in the form:

$$\lambda_{ab}^{\sigma} = \sum_{cd} U_{abcd} n_{cd}^{-\sigma} + \sum_{cd} (U_{abcd} - J_{abcd}) n_{cd}^{\sigma} - \bar{U}(\bar{n} - \frac{1}{2}) + J(\bar{n}^{\sigma} - \frac{1}{2})$$
 (3.44)

To solve the impurity model, various techniques such as Quantum Monte Carlo, Gutzwiller method or approximations such as the Hubbard-I method can be used.

3.2 Structure of the LMTART program

In this section we shall describe the overall structure and details of certain parts of the LMTART program, which is based on the equations in section 3.1.

The LMTART package contains Fortran 90 programs which can be grouped according to the function they perform. Furthermore, the programs are named such that the first three letters of the program name in each group are the same. The names of the programs in the LMTART package can be thought of as having two parts such as: $abc_-*.f$ where the first part abc_- denotes the group it can be classified into, and the second part (denoted by the wildcard character *) is different for each program in the group. We first provide a list (alphabetical) that contains a description of the various programs grouped according to the task they perform. Following that, Fig. 3.1 shows an overview of the schematic flow diagram of the LDA+DMFT implementation.

Programs with the name:

• bnd_*.f

Form the core of the solution to the generalized eigenvalue problem in the LMTO method. This includes preparing Hamiltonian matrix and overlap matrix (after factoring in contributions due to the spin-orbit coupling), calculating eigenvalues and eigenvectors, and preparing wave functions. Also calculating the fat-bands when required.

- chi_*.f

 Calculate the susceptibility.
- dmf_*.f
 Implement DMFT loop. Solve impurity model to find Green's function. Execute
 DMFT self-consistency condition.
- frc_*.f

 Calculate total energy and band energy in LDA, and various contributions to force by computing the derivative of total energy w.r.t. nuclear displacements.
- ftb_*.f

Calculate Hamiltonian, overlap matrices and all physical quantities such as total energy, in the tight-binding scheme.

In particular, see *ftb_ftbands.f* which is the control module to solve the eigenvalue problem using the tight-binding method.

• hop_*.f

Read hopping integrals from HOPFILE, prepare hopping matrix, tight-binding hopping integrals are calculated by integrating over Brillouin zone, also calculate screened structure constants.

• hub_*.f

Read HUBFILE which contains Slater integrals necessary for constructing U-matrix for the LDA+U method, compute potential in the LDA+U scheme from Hubbard-U parameters, calculate occupation matrices needed for LDA+U method.

• ini_*.f

Control the initial procedures to be performed before the main solution of the eigenvalue problem begins.

- ini_get*.f: read data for various physical quantities, e.g. ini_getchi.f reads
 susceptibility data, ini_getbnd.f reads fatband data.
- ini_make*.f: controls initial calculation of crystal group, k-mesh.
- ini_read*.f: reads data, parameters from initial files defined by the user.
- In particular, see ini_channels.f: Allocation of different channels inside the program, i.e. describes the channel numbers for all the input and output files.

• lib_*.f

Contain libraries to perform standard mathematical operations such as computing spline approximations, evaluating spherical and cubic harmonics, calculating derivatives, computing Pade coefficients etc.

• man_*.f

This set of files form the main control module and contain information on which

subroutines will be implemented depending on which options are given by the user.

- man_main.f: Main module of the entire program. Reads inputs, directs to either ASA self-consistent method or PLW full potential self-consistent method or Tight-binding method.
- man_lmtscf.f: Main control module for self-consistency stream calls various routines depending on options given by the user.
- man_ftbscf.f: Main control module for tight-binding stream, calls various programs depending on options given by user.
- man_artout.f: writes outputs.
- opt_*.f
 Calculate optical matrix elements and optical properties.
- pot_*.f
 Calculate Coulomb potential, exchange-correlation energy and potential, multipoles.
- $qmc_*.f$ Contain routines for Quantum Monte Carlo solution of the impurity model.
- rho_*.f
 Implement operations with charge density files: e.g. renormalizing core density, admixture in scf loop, Broyden mixing.
- $sgm_*.f$ Perform calculations and implement procedures involving self-energy.
- str_.f
 Prepare structure constants and derivatives, generate sites within a sphere, generate vectors in direct and reciprocal space.

• ttr_*.f

Calculate weight functions using tetrahedron method, search for Fermi energy, calculate velocities inside tetrahedron.

Fig. 3.1 shows the schematic flow diagram of the LDA+DMFT implementation.

3.3 DMFT Loop

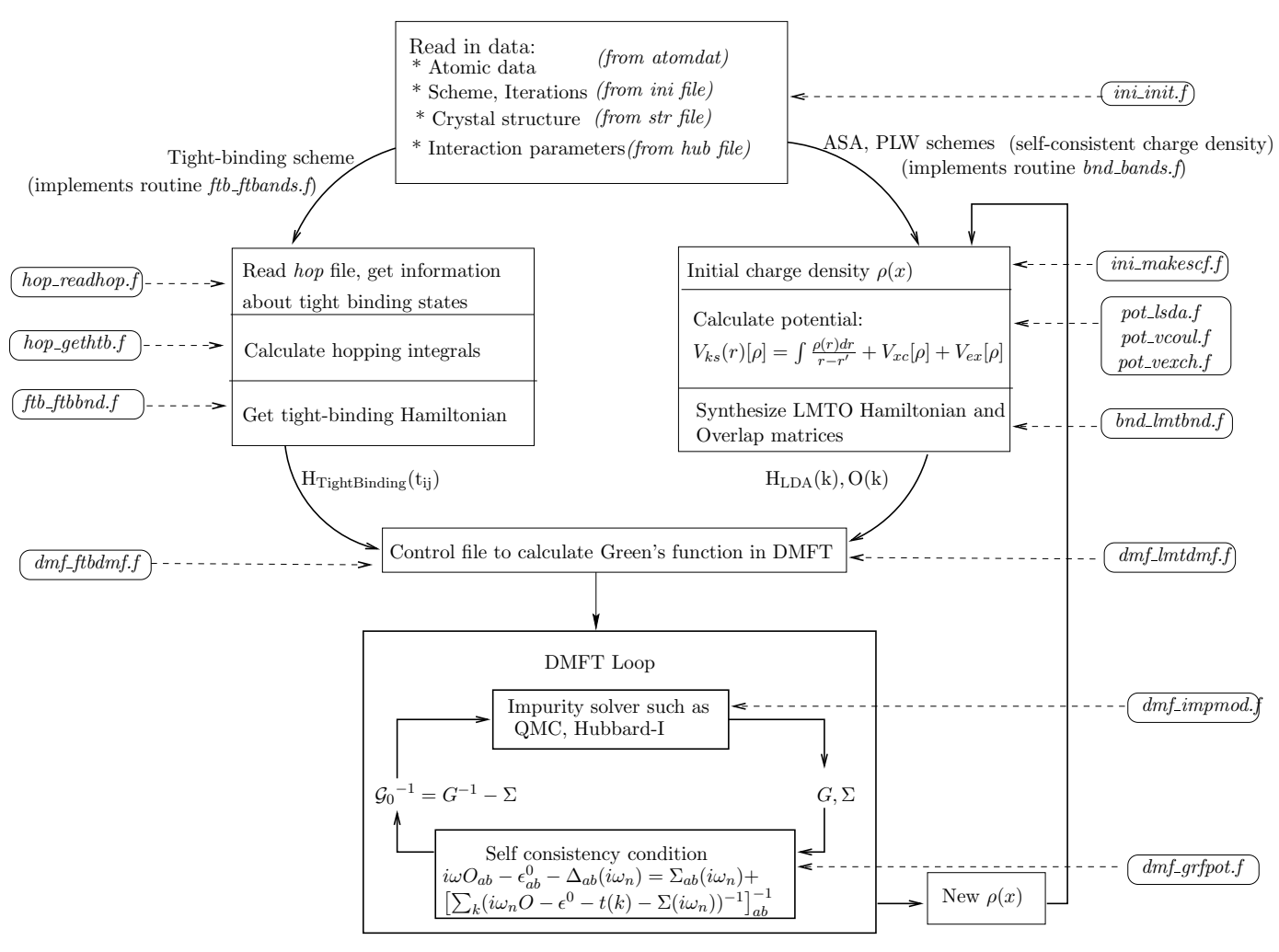
In this section, we describe in detail the sub-routines that implement the DMFT loop. The DMFT equations have a self-energy Σ , (eqn.3.35), which is the self-energy of a generalized Anderson impurity model in a bath characterized by a matrix of levels

$$\epsilon_{ab}^{0} = \epsilon_{ab}^{DC} + \sum_{\mathbf{k}} H_{ab}^{TB}(\mathbf{k}) \tag{3.45}$$

The hybridization function $\Delta_{ab}(i\omega_n)$ obeys a self-consistency condition

$$i\omega O_{ab} - \epsilon_{ab}^{0} - \Delta_{ab}(i\omega_n) = \Sigma_{ab}(i\omega_n) + \left[\sum_{k} (i\omega_n O - \epsilon^0 - t(\mathbf{k}) - \Sigma(i\omega_n))^{-1}\right]^{-1}$$
(3.46)

There are various possibilities for the double-counting term ϵ_{ab}^{DC} . One choice is to fix ϵ_{ab}^{DC} to coincide with $\Sigma(\infty)$, which is equivalent to Un, the Hatree-Fock limit. A different possibility is to fix the double counting term so that the Luttinger theorem is fulfilled, i.e. to choose $\epsilon_{ab}^{DC} = -\frac{1}{N_{\rm deg}}^2 \delta_{ab} \sum_{ab} \Sigma_{ab}(0)$.



Flow Diagram: LDA+DMFT

The exact sub-routines involved are described below.

Start DMFT loop

Input to DMFT loop: H_k^{LDA}, O_k , i.e. LDA Hamiltonian and overlap matrices from temporary file IUHAM.

• Subroutine grfsig

Input: $\Sigma(i\omega)$ from temporary file IUSGM.

Task: Read $\Sigma(i\omega)$ from IUSGM ($\Sigma = 0$ in 1st iteration)

• Subroutine **grfpot**

Input: $\Sigma(i\omega)$.

Task: Choose and set double counting $\epsilon_{DC} = \Sigma(0)$ or $\Sigma(\infty)$

• Subroutine grfbnd

Input: H_k^{LDA} and $\Sigma(i\omega)$.

Task: Construct $H_{LDA} + \Sigma(i\omega) - \Sigma_{DC}$, compute eigenvectors A^L, A^R and eigenvalues $\epsilon_k j$.

• Subroutine grffrm

Input: Eigenvalues ϵ_{kj} of $[H_{LDA} + \Sigma(i\omega) - \Sigma_{DC}]$, filling of electrons from control file.

Task: Find Fermi level ϵ_F .

$$\sum_{kj} \sum_{\omega_n} \frac{1}{i\omega_n + \epsilon_F - \epsilon_{kj}} = N_{electrons}$$

• Subroutine grfwgt

Input: Eigenvectors A^L , A^R and eigenvalues ϵ_{kj} of $[H_{LDA} + \Sigma(i\omega) - \Sigma_{DC}]$, Fermi level ϵ_F .

Task: Find weights for k-summation

$$\sum_{k} \frac{A^{L} A^{R}}{i\omega_{n} + \epsilon_{F} - \epsilon_{k}} = \sum_{k} W_{k} A^{L} A^{R}$$

• Subroutine grflev

Input: Eigenvectors A^L , A^R and eigenvalues ϵ_{kj} of $[H_{LDA} + \Sigma(i\omega) - \Sigma_{DC}]$, Overlap matrix O_k , weights for k-summation.

Task: Set matrix of impurity levels

$$E_{imp} = \left(\sum_{k} O_{k}^{-1}\right)^{-1} \left[\sum_{k} O_{k}^{-1} \left(H_{k}^{LDA} + \Sigma(\infty) - \Sigma_{DC}\right) \sum_{k} O_{k}^{-1}\right] \left(\sum_{k} O_{k}^{-1}\right)^{-1}$$

• Subroutine **implev**

Input: Impurity levels E_{imp} .

Task: Diagonalizes matrix of impurity levels: used later in impurity solver if diagonal representation is selected.

• Subroutine **grfloc**

Input: Eigenvectors A^L , A^R and eigenvalues ϵ_{kj} of $[H_{LDA} + \Sigma(i\omega) - \Sigma_{DC}]$, Overlap matrix O_k , weights for k-summation, Fermi level.

Task: Calculate local Green's function

$$G(i\omega_n) = \left(\sum_{k} \left[(i\omega_n + \epsilon_F)O(k) - (H_k^{LDA} + \Sigma(i\omega_n) - \Sigma_{DC}) \right] \right)^{-1}$$

• Subroutine grfhyb

Input: Fermi level, overlap matrix O_k , impurity levels E_{imp} , $\Sigma(i\omega)$, Σ_{DC} , local Green's function $G(i\omega)$.

Task: Calculate hybridization function

$$\Delta(i\omega_n) = (i\omega_n + \epsilon_F)O - (E_{imp} - \Sigma(\infty)) - G^{-1}(i\omega_n) - \Sigma(i\omega_n)$$

• Subroutine impmod

Input: Hybridization $\Delta(i\omega)$, impurity levels E_{imp} , overlap O_k .

Task: Impurity solver

• Subroutine **grfpot**

Task: Set double counting with new $\Sigma(i\omega)$.

$$\epsilon_{DC} = \Sigma(0)$$
 or $\Sigma(\infty)$

Check if number of DMFT iteration is equal to NDIT (In control file: hubfile, controls maximum number of DMFT iterations). If so, proceed to next file **grfden** to calculate charge density. If not, use $\Sigma(i\omega)$ from Impurity solver as an input to the next iteration in the self-consistency condition.

• Subroutine grfden

Input: New Green's function constructed from $\Sigma(i\omega)$ calculated by the impurity solver, eigenvectors of $[H_{LDA} + \Sigma(i\omega) - \Sigma_{DC}]$.

Task: Calculate charge density

$$\rho(r) = \sum_{\omega_n} \sum_{ab} \chi_a(r) G_{ab}(i\omega_n) \chi_b(r)$$

from which the outer LDA loop begins again.

3.3.1 Impurity solver: Hubbard-I method

The impurity model can be solved using different solvers – exact methods such as Quantum Monte Carlo (computationally expensive for low temperatures) or approximate methods such as Hubbard-I or Gutzwiller approximation. In this section we describe the details of one such method that is based on the Hubbard-I approximation [49, 50]. The equations can be tailored to fit the symmetry of the system in hand. A simple case is when different states for a fixed number of electrons in an atom are considered equivalent. The equations we describe here are suited for a system in which spin-orbit effects are significant. In particular, we deal with an actinide system with $14\ f$ -levels that are split into two sub-bands due to spin-orbit coupling. In chapter 5, we discuss the results of this calculation for Americium.

The starting point of the Hubbard-I approximation is the atomic limit. The self-energy describes the two atomic levels and the Green's function consists of two poles at $i\omega - \mu$ and $\omega - \mu + U$. We first find the Green's function for the atomic Hamiltonian using the equation of motion method for the Hubbard operators. We then express the impurity Green's functions in terms of the atomic Green's function and the hybridization $\Delta(i\omega)$.

We start with a multi-band impurity model that has the form $H = H_{atom} + H_{band} + H_{hyb}$.

$$H_{atom} = \sum_{\substack{ll'=5/2,7/2\\m=1...(2l+1)\\m'=1...(2l'+1)}} \epsilon_{ll'mm'}^{f} f_{lm}^{\dagger} f_{l'm'} + U \sum_{\substack{l,l'=5/2,7/2\\m,m'}} f_{lm}^{\dagger} f_{lm} f_{l'm'}^{\dagger} f_{l'm'}$$

$$H_{band} = \sum_{lk} \epsilon_{lk} c_{lk}^{\dagger} c_{lk}$$

$$H_{hyb} = \sum_{ll'mk} V_{ll'k} (f_{lm}^{\dagger} c_{l'k} + h.c.)$$
(3.47)

Here l,l' label the two bands that are split due to spin-orbit coupling. These two bands have the j-quantum number as 5/2 or 7/2. Notation: The band with l=5/2 and is 6-fold degenerate and that with l=7/2 and is 8-fold degenerate. Thus m,m' label the degeneracy and run from 1 to (2j+1). Since the impurity level matrix $\epsilon_{ll'mm'}^f$ has off-diagonal terms as zero, the first term simplifies to $\sum_{lm} \epsilon_l^f f_{lm}^{\dagger} f_{lm}$. H_{hyb} is due to the hybridization between the conduction electrons and the localized f electrons. The hybridization function can be written as $\Delta_l(i\omega) = \sum_{l'k} V_{l'k}^2/(i\omega - \epsilon_{l'k})$.

Due to the above degeneracy, we have a $SU(6) \times SU(8)$ symmetry. With this, the impurity Green's function in the Hubbard-1 approximation becomes

$$\left[G_l^{imp}(i\omega)\right]^{-1} = \left[G_l^{at}(i\omega)\right]^{-1} - \Delta_l(i\omega) \tag{3.48}$$

The atomic Green's function G_{at} is given by

$$G_l^{at}(i\omega) = \sum_{n=0}^{14} \sum_{\substack{n_1=0\\n_1<6\\(n-n_1)<8}}^{n} \frac{\left(C_{n_1}^6 C_{n-n_1}^8 \left[e^{-E_{ln}/T} - e^{-E_n/T}\right]\right)/Z}{i\omega + \mu - E_{ln} + E_n}$$
(3.49)

where E_{ln} is the energy of an atom with n total number of electrons, n_1 in level l=1 and $n-n_1$ in level l=2 is given by :

$$E_{ln} = E_n + \epsilon_l^f + Un \tag{3.50}$$

$$E_n = \frac{U(n-1)n}{2} + n_1 \epsilon_1^f + (n-n_1)\epsilon_2^f$$
 (3.51)

The numerator in (3.49) denotes the probability of finding an atom with n total number of electrons, n_1 in level l = 1 and $n - n_1$ in level l = 2. $C_{n_1}^6$ and $C_{n-n_1}^8$ are the

combinatorial coefficients. Z is a normalization factor for the probability given by

$$Z = \sum_{n=0}^{14} \sum_{\substack{n_1=0\\n_1\leq 6\\(n-n_1)\leq 8}}^{n} C_{n_1}^6 C_{n-n_1}^8 e^{-E_n} / T$$
(3.52)

Using the Hubbard-I approximation to solve for the impurity Green's function, we get a splitting of the upper and lower Hubbard bands for arbitrarily small but finite U.

In the LMTART program the above procedure is implemented in the routine $impatomsun_so$ in the file $dmf_imp_atomso.f$. This in turn calls upon $cal_sigma_atomsun_so.f$ and $cal_green_atomsun0_so.f$ to calculate the self-energy and Green's function respectively. The output is the Green's function and the probability distribution of finding an atom with n electrons. At large U we expect this distribution to be peaked at a single value n which should also describe the number of electrons calculated from the Green's function.

3.4 Preparing control files for LMTART

In this section we briefly describe the control files that need to be prepared for the implementation of the LMTART program. For LDA calculations only, there are two essential input files – the ini and the str files. The ini file contains details about the various approximation schemes such as 'full-potential plane wave' or 'atomic sphere approximation' as well as those about the exchange-correlation functional. It also contains information about the different atoms in the unit cell. The structure file or the str file has information about the crystal structure. In addition, for LDA+U or LDA+DMFT calculations, we need the hub file that contains the interaction parameters and the DMFT options.

Each control file is divided into different sections, separated by $\langle SECTION = \rangle$, each containing a certain set of data. There are certain common features in each control file:

• The first line $\langle FILE = ***FILE, INPUT = MODERN \rangle$ where '***' stands for the type of control file – i.e., INI or STR or HUB, must be present in each control file. This line is required by the main program in the LMTART program to call the corresponding subroutine to read the control file.

- The first section in the control files contains the title of the material this section is optional.
- A comment that usually contains the description of the parameter and some options for it can be placed on each line after a '!' mark.
- Many parameters have default values. If a default value exists, this parameter can be omitted from the file.

3.4.1 *INI* file

• $\langle SECTION = CTRL \rangle$

The parameters in this section control the choice of the scheme we would like to use in the implementation of LMTART.

- FullPot This parameters allows us to choose the approximation for the potential seen by an atom in the solid. The choices are a Full Potential plane wave approximation (PLW) or the atomic sphere approximation (ASA) where the potential in the interstitial region is approximated by a constant. We can also describe the Hamiltonian in a tight-binding representation (FTB) and solve the eigenvalue problem.

• $\langle SECTION = ITER \rangle$

Details about the iterational loop are contained in this section.

$-\langle SECTION = MAIN \rangle$

This section contains information about the number of atoms and spins in the unit cell.

- Nsort: The number of non-equivalent atoms in the unit cell. This parameter becomes important in anti-ferromagnetic calculations as explained in section 3.4.3.
- **Is:** This labels the different kinds of basis atoms. The order must correspond to that in $\langle SECTION = BASS \rangle$ in the str file. An example is provided in Table 3.3.

Par0: The lattice parameter in atomic units needs to be provided, which
is used, along with the crystal structure to calculate the energy in Rydberg
units.

• $\langle SECTION = SORT \rangle$

This section contains information about the atoms. Once the name and atomic number of each element is entered, the LMTART routine searches for relevant information for the atom in the directory /atomdat/.

Note: The set of parameters above, in $\langle SECTION = SORT \rangle$ must be entered for each non-equivalent atom (the number of non-equivalent atoms being indicated in the parameter **Nsort**).

3.4.2 *STR* **file**

The structure file contains all the information about the crystal structure. To prepare the file, we need to know about the unit cell of the lattice – the parameters describing the geometry of the cell, the primitive translation vectors and the basis atoms. This information can be obtained from experimental values.

Table 3.2 describes a sample str file for NiO which has a FCC structure with two basis atoms, i.e. Ni and O. The unit cell for this is schematically shown in Fig. 3.2 In the notation we use, the primitive vectors of the unit cell are expressed as $A\hat{x} + B\hat{y} + C\hat{z}$ as shown in Fig. 3.2.

• $\langle SECTION = CTRS \rangle$

- Natom: The total number of basis atoms in the unit cell. For the above example of NiO it is 2. (no default)
- B to A: The ratio of the length along the y-direction to that along the x-direction. In the above example, we have a cubic cell, hence this ratio is
 1. (default is 1.0)

⟨FILE=INIFILE, INPUT=MODERN ⟩ ************* ⟨SECTION=HEAD⟩ ! PROJECT HEAD: title = NiO! Compound title ⟨SECTION=CTRL⟩ ! CONTROL PARAMETERS: Lmto = Bare! set: Bare / Screened / Rspace ! set: FTB/ ASA / PLW FulPot=ASA ⟨¡SECTION=EXCH⟩ ! EXCHANGE-CORRELATION: LDA = Vosko! set: none/Barth/Gunn/etc. ⟨SECTION=ITER ⟩ ! ITERATIVE PROCEDURES: Niter1=40! # of iterations in SCF loop Lbroy = 1! Broyden mixing for low l.le.lbroy Admix1 = 0.05000! initial mixing for density ⟨SECTION=MAIN⟩ ! MAIN ATOMIC DATA: Natom = 2! # of atoms in the unit cell Nsort = 2! # of sorts in the unit cell Nspin = 1! # of spins Norbs =1! 1-without/2 -with spin orbit coupling Par0 = 7.92600! lattice parameter in a.u. Is(:) = 1 2! atom-to-sort pointer array ⟨SECTION=SORT⟩ ! SORT DATA: Name = Ni! atom label Znuc = 28.0000! nuclear charge Smts=2.17900! non-overlapping MT-sphere Split = 0.50000! initial splitting ⟨SECTION=SORT⟩ ! SORT DATA: Name = O! atom label Znuc = 8.0000! nuclear charge Smts = 1.78300! non-overlapping MT-sphere Split = 0.50000! initial splitting Ndiv(:) = 6 6 6! Tetrahedron mesh

Table 3.1: Input file nio.ini

⟨FILE=STRFILE, INPUT=MODERN ⟩ ************ ⟨SECTION=HEDS⟩ ! STRUCTURE TITLE: Slabl = NiO⟨SECTION=CTRS⟩ ! CONTROL STRUCTURE: ! # of atoms Natom = 2BtoA = 1.00000! b over a ratio CtoA = 1.00000! c over a ratio ⟨SECTION=TRAN ⟩ ! PRIMITIVE TRANSLATIONS: 1/2, 1/2, 0.0! Ax,Ay,Az 1/2, 0.0, 1/2! Bx,By,Bz 0.0, 1/2, 1/2! Cx,Cy,Cz⟨SECTION=BASS⟩ ! BASIS ATOMS : 0.0, 0.0, 0.0! Ni@1 1/2, 1/2, 1/2! O@2

Table 3.2: Input file nio.str

- C to A: The ratio of the length along the z-direction to that along the x-direction. In the above example, we have a cubic cell, hence this ratio is
 1. (default is 1.0)
- $\langle \text{SECTION} = \text{TRAN} \rangle$ (no default)

 This section contains the primitive translation vectors of the lattice. For example, for the FCC lattice the set of vectors can be written as $\left(\left(\frac{1}{2}, \frac{1}{2}, 0\right), \left(0, \frac{1}{2}, \frac{1}{2}\right), \left(\frac{1}{2}, 0, \frac{1}{2}\right)\right)$ and for the BCC lattice the set is $\left(\left(\frac{1}{2}, \frac{1}{2}, -\frac{1}{2}\right), \left(-\frac{1}{2}, \frac{1}{2}, \frac{1}{2}\right), \left(\frac{1}{2}, -\frac{1}{2}, \frac{1}{2}\right)\right)$.
- \(\section \) (no default)
 This section contains the positions of the basis atoms in the unit cell, that, along with the primitive translations from the above section will generate the full lattice.
 Note: The order in which the basis atoms are written mut correspond to the order in which the atoms are written in \(\setminus \) SECTION = SORT\(\rightarrow\) in the ini file

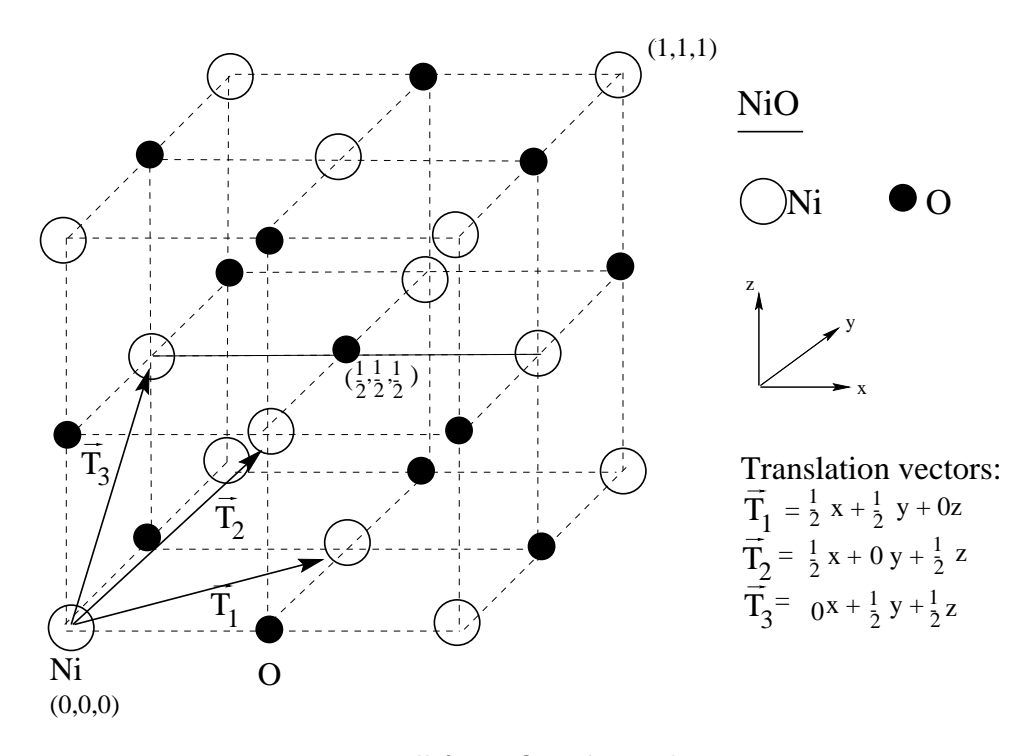


Figure 3.2: Unit cell for NiO and translation vectors.

3.4.3 Modifications for anti-ferromagnetic solution

If we need to compute the anti-ferromagnetic solution for a given material, we need to make appropriate changes in the *ini* as well as *str* files. To have an anti-ferromagnetic solution, we pick alternate magnetic atoms in the lattice to have *up* and *down* spins respectively. The unit cell thus has to be doubled, and contains two non-identical magnetic atoms due to different spins, even though the atomic numbers of the two atoms remain the same.

The main modifications in the *ini* file are in $\langle SECTION = MAIN \rangle$ as shown in a part of the *ini* file for anti-ferromagnetic NiO in Table 3.3. Note, especially, the parameter **Is(:)** which sorts the different atoms. Even though Atom 1 and Atom 2 are both nickel, we treat them differently due to their different spins. $\langle SECTION = SORT \rangle$ contains information about the different spins in the parameter **Split** which has different signs for potential for up and down spins.

To determine the crystal structure we treat the lattice as a new structure with different primitive translations and basis atoms and re-construct the *str* file. For the same example of NiO as above, we begin with Fig. 3.3 to generate the primitive

translations and basis atoms. The str file for this case is shown in Table 3.4.

```
⟨SECTION=MAIN ⟩
                        ! MAIN ATOMIC DATA:
Natom = 4
                        ! # of atoms in the unit cell
Nsort = 3
                        ! # of sorts in the unit cell
Nspin = 2
                        ! # of spins
                        ! 1-without/2 -with spin orbit coupling
Norbs = 1
Par0 = 7.02600
                        ! lattice parameter in a.u.
Is(:) = 1 2 3 3
                        ! atom-to-sort pointer array
⟨SECTION=SORT⟩
                        ! SORT DATA:
Name = Ni1
                        ! atom label
Znuc = 28.0000
                        ! nuclear charge
Smts = 2.17900
                        ! non-overlapping MT-sphere
Split = 0.50000
                        ! initial splitting
⟨SECTION=SORT⟩
                        ! SORT DATA:
Name = Ni2
                        ! atom label
Znuc = 28.0000
                        ! nuclear charge
Smts = 2.17900
                        ! non-overlapping MT-sphere
Split = -0.50000
                        ! initial splitting
(SECTION=SORT)
                        ! SORT DATA:
Name = O
                        ! atom label
Znuc = 8.0000
                        ! nuclear charge
Smts = 1.78300
                        ! non-overlapping MT-sphere
Split = 0.50000
                        ! initial splitting
Ndiv(:) = 6 6 6
                        ! Tetrahedron mesh
```

Table 3.3: Input file nio.ini for anti-ferromagnetic NiO

More working examples of the str file are given in chapter 4.3.1 YbRh₂Si₂ and in section 5.2 for Am. Also, 3.4.3 contains the str file for the anti-ferromagnetic case for YbRh₂Si₂, where the unit cell has to be doubled to contain two magnetic Yb atoms.

3.4.4 *HUB* file

The main data in this file that need to be entered by the user are the choice of scheme to treat the correlated orbitals (LDA+U or LDA+DMFT) and the values of the interaction parameters. After the first iteration, additional data regarding occupancy matrices, self-energies and potential terms are written into this file.

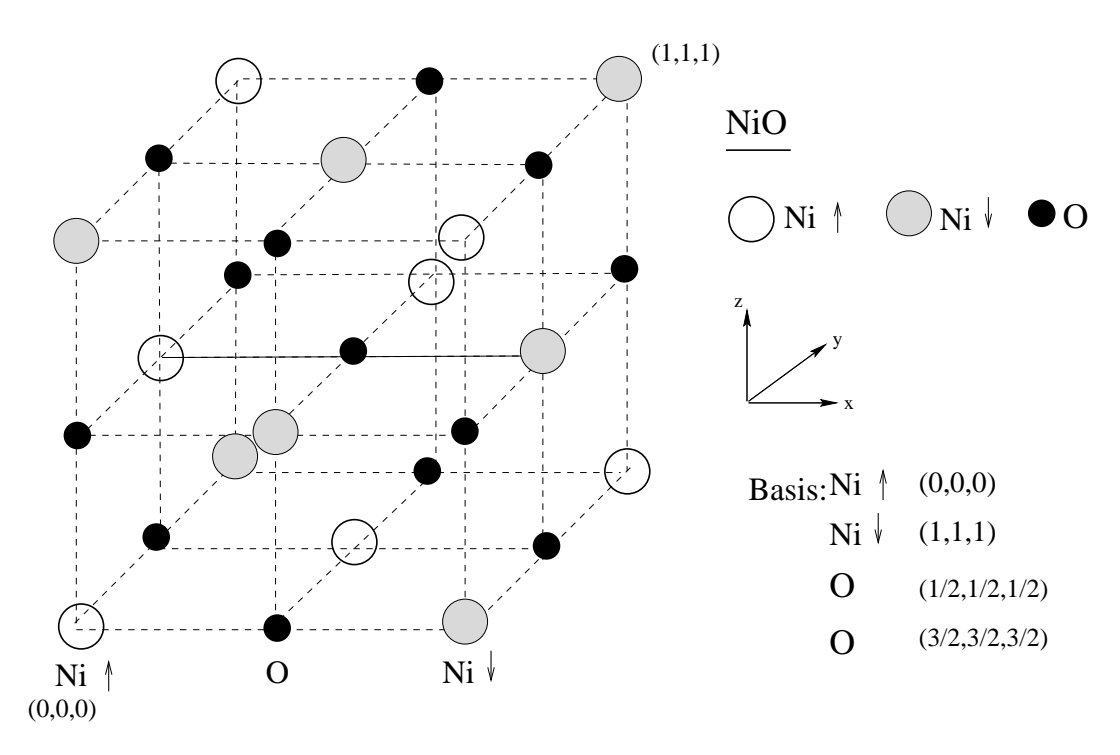


Figure 3.3: Unit cell for anti-ferromagnetic case

$\langle \text{FILE=STRFILE, INPUT=MODERN} \ \rangle$	

$\langle SECTION = HEDS \rangle$! STRUCTURE TITLE:
Slabl = NiO	
$\langle \text{SECTION} = \text{CTRS} \rangle$! CONTROL STRUCTURE:
Natom =4	! # of atoms
BtoA = 1.00000	! b over a ratio
CtoA = 1.00000	! c over a ratio
$\langle \text{SECTION=TRAN} \rangle$! PRIMITIVE TRANSLATIONS:
1/2, 1/2, 1.0	! Ax,Ay,Az
1/2, 1.0, 1/2	! Bx,By,Bz
1.0, 1/2, 1/2	! Cx,Cy,Cz
$\langle SECTION=BASS \rangle$! BASIS ATOMS :
0.0 , 0.0 , 0.0	! Ni1@1
$1.0 \; , 1.0 \; , 1.0$! Ni2@2
1/2 , $1/2$, $1/2$! O @3
3/2, $3/2$, $3/2$! O @4

Table 3.4: Input structure file nio.str for the anti-ferromagnetic case $\,$

A sample hub file for the anti-ferromagnetic case in NiO is shown in Table 3.5. All the energy values are in Rybergs. The various sections are explained below:

• $\langle SECTION = CTRL \rangle$

- Scheme: The details about the scheme to be used to treat the correlated orbitals, i.e. LDA+U or LDA+DMFT. A list of all the possible schemes that can be used is present in the file hub_readhub.f and hub_hubpot.f.
- Ncrl: The number of states which appear in the correlated term. Descriptions and options of the other parameters in this section appear as comments in the hub file in Table 3.5.

• $\langle SECTION = DMFT \rangle$

This section needs to be included only if the option for Scheme in the above section is chosen as LDA+DMFT. The details of the number of Matsubara frequencies to be used and the bandwidth for the grid are contained here.

- solver: The impurity solver used in the DMFT loop. A list of the solvers
 (e.g. QMC, Hubbard-I, Gutzwiller) appears in the file hub_readhub.f.
- **Kstates:** This is a pointer to the states in the correlated orbital that are treated similarly. For example, in NiO, there are 10 correlated states from the 3d orbital hence we need 10 labels. The t_2g spin-up states in are treated similarly, thus they all carry the label 1. Similarly the e_g spin-up states all carry the label 2, and so on.

\(\section = \corr \corr \)

This section has the core information about the interaction terms.

- Cstate: This points to the atom that has correlations, its position in $\langle SECTION = BASS \rangle$ in the str file and the correlated orbital.
- F0, F2, F4, F6: These are parameters that appear in the Slater integrals as explained in equations 29-32. For d-electrons, three constants F0, F2 and F4 are needed and for f-electrons, there are four constants F0, F2, F4 and

F6. These can be linked to U and J via U = F0 and J = (F2 + F4)/14 for d-electrons with F2/F4 = 0.625. For f-electrons, U = F0 and J = (286F2 + 194F4 + 250F6)/6435.

Note: The set of parameters above, in $\langle SECTION = CORR \rangle$ must be entered for each correlated state (the number of correlated states being defined by the parameter **Ncrl**).

• $\langle SECTION = DHUB \rangle$

From this section onwards, data about occupancy matrices, self-energies etc are written into the hub file after the first iteration. These quantities are self-consistently calculated at each iteration and are rewritten. A sample occupancy matrix for the 3d state of Ni in NiO is shown in Table 3.6.

We have now established the theoretical groundwork for the LDA+DMFT method to realistically treat strongly correlated materials. We shall turn to two applications of this method: in Chapter 4, we study the heavy fermion compound YbRh₂Si₂ and in Chapter 5, we discuss the Mott transition issue in Americium.

⟨FILE=HUBFILE, INPUT=MODERN ⟩	

$\langle SECTION = CTRL \rangle$! CONTROL PARAMETERS:
Scheme=LDA+U1.1	! LDA+U1.# / LDA+C / LDA+DMFT
Yharm =cubic	! Cubic/Spherical harmonics (output)
Iharm = cubic	! Cubic/Spherical harmonics (input)
Rorbs = Both	! One/Both orbits to read
Rspin = Both	! One/Both spins to read
Ncrl = 2	! # of correlated states
$\langle \text{SECTION=DMFT} \rangle$! DMFT SETTINGS:
Nmsb = 50	! # of Matsubara frequencies
Obnd = 0.5000000	! Effective bandwidth for the grid
Nmsl = 2048	! # of linear Matsubara frequencies
Nmsb = 1	! # of Matsubara frequencies
Ndit = 20	! # of DMFT iterations
Efermi = 0.7278130	! Fermi energy (Ry)
Solver = Hub1	! impurity solver choice
kStates(:)=1 1 1 2 2 3 3 3 4 4	
$\langle SECTION = CORR \rangle$! CORRELATED STATES:
Cstate = Ni1@1::3d	! Correlated state pointer
F0 = 0.5880000	! Slater integrals
F2 = 0.6012300	! Slater integrals
F4 = 0.3787700	! Slater integrals
F6 = 0.000000	! Slater integrals
Cstate = Ni2@2::3d	! Correlated state pointer
F0 = 0.5880000	! Slater integrals
F2 = 0.6012300	! Slater integrals
F4 = 0.3787700	! Slater integrals
F6 = 0.000000	! Slater integrals
$\langle \text{SECTION=DHUB} \rangle$! PARTIAL OCCUPANCIES:
cState=Ni1@1::3d	! spin up/dn-up/dn data are :

Table 3.5: Input hub file nio.hub

$\langle \text{SECTION=DHUB} \rangle$! PARTIAL OCCUPANCIES:		
cState = Ni1@1::3d					
yz	ZX	xy	x2-y2	3z2-1	REAL, Up-Up
0.9540211	0.0000329	0.0000329	-0.0005166	0.0002983	yz
0.0000329	0.9540211	0.0000329	0.0005166	0.0002983	ZX
0.0000329	0.0000329	0.9540211	0.0000000	-0.0005966	xy
-0.0005166	0.0005166	0.0000000	0.1318555	0.0000000	x2-y2
0.0002983	0.0002983	-0.0005966	0.0000000	0.1318555	3z2-1
yz	$\mathbf{Z}\mathbf{X}$	xy	x2-y2	3z2-1	${ m IMAG, Up-Up}$
0.0000000	0.0000000	0.0000000	0.0000000	0.0000000	yz
0.0000000	0.0000000	0.0000000	0.0000000	0.0000000	ZX
0.0000000	0.0000000	0.0000000	0.0000000	0.0000000	xy
0.0000000	0.0000000	0.0000000	0.0000000	0.0000000	x2-y2
0.0000000	0.0000000	0.0000000	0.0000000	0.0000000	3z2-1
yz	$\mathbf{Z}\mathbf{X}$	xy	x2-y2	3z2-1	$_{ m REAL,Dn\text{-}Dn}$
0.9584327	0.0000286	0.0000286	-0.0000267	0.0000154	yz
0.0000286	0.9584327	0.0000286	0.0000267	0.0000154	ZX
0.0000286	0.0000286	0.9584327	0.0000000	-0.0000308	xy
-0.0000267	0.0000267	0.0000000	0.9875338	0.0000000	x2-y2
0.0000154	0.0000154	-0.0000308	0.0000000	0.9875338	3z2-1
yz	$\mathbf{Z}\mathbf{X}$	xy	x2-y2	3z2-1	$_{\mathrm{IMAG,Dn-Dn}}$
0.0000000	0.0000000	0.0000000	0.0000000	0.0000000	yz
0.0000000	0.0000000	0.0000000	0.0000000	0.0000000	ZX
0.0000000	0.0000000	0.0000000	0.0000000	0.0000000	xy
0.0000000	0.0000000	0.0000000	0.0000000	0.0000000	x2-y2
0.0000000	0.0000000	0.0000000	0.0000000	0.0000000	3z2-1

Table 3.6: Partial occupancies for Ni in nio.hub

Chapter 4

Electronic structure and properties of f-band materials: YbRh₂Si₂

4.1 Introduction

In this chapter, we present our calculations of the the band structure and electronic properties of $YbRh_2Si_2$, a heavy-fermion compound. This material is experimentally well studied and has an anti-ferromagnetic phase transition at low temperature (T < 10~K) and ambient pressure. Susceptibility measurements on the material show a strong magnetic anisotropy [53]. Using DFT methods, we would like to study the various magnetic phases of this compound and compute its magnetic properties such as magnetic anisotropy energy.

We start our calculations with the standard LDA method. However, since YbRh₂Si₂ is a material with a strongly localized f-band, the LDA method is inadequate to explain the magnetic ground state of the material, as we expect. We then employ the LDA+U method which includes electron-electron interaction terms in the energy functional. However we find that in this case, LDA+U does not predict the correct magnetic ground state. The problem is traced to the double-counting term in the LDA+U functional, which includes the part of the total energy that have already been taken into account in the LDA Hamiltonian. This term is to be subtracted from the total energy, so that only the correction of the LDA mean-field solution is left. However, this procedure is not unique and there are various ideas previously implemented such as those by Mazin [54], Anisimov [15], Czyzyk and Sawatzky [55].

Our approach to the double-counting issue was to use an empirical method to determine which choice of parameters correctly predict the ground state. Once we found the suitable ground state solution, we proceeded to calculate properties such as magnetization and magnetic anisotropy energy. With the application of pressure, it should be possible to drive the non-magnetic phase of YbRh₂Si₂ into a magnetically ordered ground state. In our calculation, we study the evolution of magnetism in this material as a function of various parameters such as pressure and Coulomb interaction.

In section 4.2 we describe the motivation and the experimentally known properties of this material. Section 4.3 contains the results of our calculation to reproduce the magnetic ground state of the material using various techniques. In section 4.4, we use our calculated band structure to compute the magnetic anisotropy energy of YbRh₂Si₂. Finally, in section 4.5, we summarize the various techniques we used in the study of the compound, and draw our conclusions.

4.2 Properties of YbRh₂Si₂

Experimentally YbRh₂Si₂ is known to have an anti-ferromagnetic quantum critical point at ambient pressure [53]. It is an undoped and atomically well-ordered material. X-Ray diffraction studies showed that YbRh₂Si₂ has a body centered tetragonal phase as shown in Fig. 4.1 with the lattice parameters a = 4.007 Å and c = 9.858 Å [56]. The valence shell of Yb is in the $4f^{13}$ configuration.

At high temperatures, the magnetic susceptibility shows a Curie-Weiss like behavior with magnetic moment $\mu_{eff} = 4.5\mu_B$ which is almost equal to that of the free Yb³⁺ ion. The magnetic susceptibility along the plane of the tetragonal structure is measured to be much larger than that along the c-axis. This anisotropy in the magnetic response indicates that the Yb³⁺ moments form a 2-dimensional lattice perpendicular to the c-axis. At ambient pressure and low temperature $T_N = 65mK$, YbRh₂Si₂ develops a long range anti-ferromagnetic order. One of the goals of our band structure computation is to obtain the different magnetic phases of YbRh₂Si₂, and to calculate it magnetic properties. Further, we would like to compute properties of this material that might arise as a result of the strong magnetic anisotropy.

YbRh₂Si₂ shows many deviations from Fermi liquid behavior at low temperatures

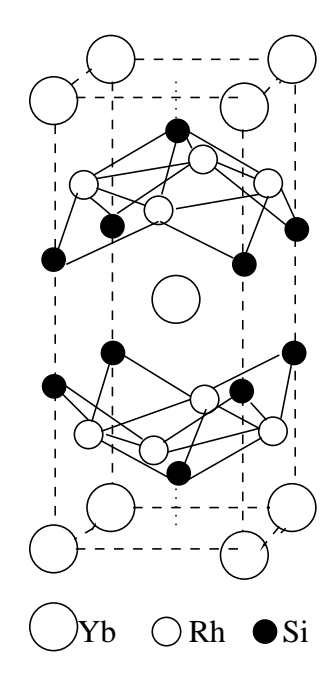


Figure 4.1: Body centered tetragonal crystal structure for YbRh₂Si₂

such as linear temperature dependence of electrical resistivity and a logarithmic dependence of specific heat $C/T \propto -\ln T$. These unusual properties arise due to the interactions between the localized f-electrons in Yb³⁺ and the conduction band formed by the s,p and d electrons. We would like to use the band structure calculation to understand how localized bands and strong correlations in the 4f-electrons affect the properties of the material.

4.3 Band structure calculation of YbRh₂Si₂

The computation of the band structure is done using the LmtART code [57] based on the linear muffin-tin orbital density functional method as described in the previous chapter. We start with the LDA method. Since YbRh₂Si₂ exhibits strong electron-electron correlations we expect an LDA calculation to fail to reproduce the magnetic ground state of the material. We recalculate the structure using the LDA+U technique. We will show that LDA+U also does not work well, due to problems with the double counting term in the functional.

4.3.1 LDA calculation

We first describe some technical details of the numerical simulation:

The program and the database associated with it provides the Hamiltonian and the overlap matrix of the valence orbitals as well as the necessary space group information and Brillouin zone data. The unit cell of YbRh₂Si₂ has five basis atoms at the following positions: Yb(0,0,0), Rh1(0,1/2,1/4), Rh2(1/2,0,1/4), Si1(0,0,3/8), Si2(0,0,5/8). This information is contained in the input structure file ybrh2si2.str shown in Table 4.1. Details about the atomic numbers of elements in the solid, the the lattice constant, the schemes used for self-consistency (ASA) and exchange-correlation, and information about the iterations in the self-consistent loop, in are contained the input file ybrh2si2.ini in Table 4.2. Finally, for the LDA+U calculation, the details of the interactions U and J, and the correlations are contained in the file ybrh2si2.hub in Table 4.3.

```
⟨FILE=STRFILE, INPUT=MODERN ⟩
************
⟨SECTION=HEDS⟩
                                        ! STRUCTURE TITLE:
Slabl = YbRh2Si2
⟨SECTION=CTRS⟩
                                        ! CONTROL STRUCTURE:
Natom = 5
                                        ! # of atoms
BtoA = 1.00000
                                        ! b over a ratio
                                        ! c over a ratio
CtoA = 2.46019
⟨SECTION=TRAN ⟩
                                        ! PRIMITIVE TRANSLATIONS:
-1/2, 1/2, 1/2
                                        ! Ax,Ay,Az
1/2, -1/2, 1/2
                                        ! Bx,By,Bz
1/2, 1/2, -1/2
                                        ! Cx,Cy,Cz
⟨SECTION=BASS⟩
                                        ! BASIS ATOMS :
0.0 , 0.0 , 0.0
                                        ! Yb
0.0, 1/2, 1/4
                                        ! Rh1
1/2 , 0.0 , 1/4
                                        ! Rh2
0.0, 0.0, 3/8
                                        ! Si1
                                        ! Si2
0.0, 0.0, 5/8
```

Table 4.1: Input file ybrh2si2.str

⟨FILE=INIFILE, INPUT=MODERN ⟩ ************************************ ! PROJECT HEAD: ⟨SECTION=HEAD⟩ title = YbRh2Si2! Compound title ⟨SECTION=CTRL⟩ ! CONTROL PARAMETERS: Lmto = Bare! set: Bare / Screened / Rspace ! set: FTB/ ASA / PLW FulPot=ASA ⟨¡SECTION=EXCH⟩ ! EXCHANGE-CORRELATION: LDA = Vosko! set: none/Barth/Gunn/etc. $\langle SECTION = ITER \rangle$! ITERATIVE PROCEDURES: Niter1=200! # of iterations in SCF loop Lbroy = -1! Broyden mixing for low l.le.lbroy ! initial mixing for density Admix1 = 0.05000! MAIN ATOMIC DATA: ⟨SECTION=MAIN⟩ Natom = 5! # of atoms in the unit cell Nsort = 3! # of sorts in the unit cell Nspin = 2! # of spins Norbs =2! 1-without/2 -with spin orbit coupling Par0 = 7.57500! lattice parameter in a.u. Is(:) = 1 2 2 3 3! atom-to-sort pointer array ⟨SECTION=SORT⟩ ! SORT DATA: Name = Yb! atom label Znuc = 70.0000! nuclear charge Smts = 3.66200! non-overlapping MT-sphere Split = 0.00000! initial splitting ⟨SECTION=SORT⟩ ! SORT DATA: Name = Rh! atom label Znuc = 45.0000! nuclear charge Smts = 2.26700! non-overlapping MT-sphere ⟨SECTION=SORT⟩ ! SORT DATA: Name = Si! atom label Znuc = 14.0000! nuclear charge Smts = 2.17800! non-overlapping MT-sphere ! FFT GRIDS: ⟨SECTION=FFTS⟩

Table 4.2: Input file ybrh2si2.ini

! Tetrahedron mesh

Ndiv(:)=6666

```
⟨FILE=HUBFILE, INPUT=MODERN ⟩
*********************************
⟨SECTION=CTRL⟩
                                            ! CONTROL PARAMETERS:
Scheme=LDA+U1.1
                                            ! LDA+U1.# / LDA+C / LDA+CU1.# / LDA+G:
                                            ! Cubic/Spherical harmonics (output)
Yharm =spherical
Iharm =spherical
                                            ! Cubic/Spherical harmonics (input)
Rorbs = Both
                                            ! One/Both orbits to read
Rspin = Both
                                            ! One/Both spins to read
Format=complex
                                            ! Real/Complex input/output
⟨SECTION=CORR⟩
                                            ! CORRELATED STATES:
Ncrl = 1
                                            ! # of correlated states
Cstate = Yb@1::4f
                                            ! Correlated state pointer
OutSvs = local
                                            ! global/local coordinate system
OutAxis = -1,1,0
                                            ! rotational axis
OutAngle= 0*pi
                                            ! rotational angle
OutInv = no
                                            ! apply inversion after rotation
InpSys = local
                                            ! global/local coordinate system
InpAxis = -1,1,0
                                            ! rotational axis
InpAngle= 0*pi
                                            ! rotational angle
                                            ! apply inversion after rotation
InpInv = no
F0 = 0.4411765
                                            ! Slater integrals
F2 = 0.000000
                                            ! Slater integrals
F4 = 0.000000
                                            ! Slater integrals
F6 = 0.000000
                                            ! Slater integrals
⟨SECTION=DHUB⟩
                                            ! PARTIAL OCCUPANCIES:
                                            ! spin up/dn-up/dn data are :
cState=Yb@1::4f
```

Both the full potential plane-wave (PLW) and the atomic sphere approximation (ASA) schemes have been used. The results for the energy bands (using the PLW scheme) show a narrow localized set of bands below the Fermi level E_F which is near 13.7eV (Fig. 4.2,left). On investigating the character of these localized bands, which are near energies of ~ 13 eV, it is seen that these correspond to the localized 4f bands of Yb, as expected. Self-consistency for the energy was obtained in ~ 40 iterations. We find that the there are 14 fully occupied 4f-bands below E_F at the Γ point. The LDA calculation predicts that all the 4f-bands are filled, that is, the occupancy of the 4f-bands of Yb in YbRh₂Si₂ is 14.

On performing the same calculation using the ASA method to compute the potential, we find that the main differences are that the overall energies and the Fermi level have shifted downwards with the Fermi energy $E_F \sim 13 \, \mathrm{eV}$, and that the position of the localized 4f bands of Yb are pushed further below to $12 \, \mathrm{eV}$ (Fig. 4.2,right). Unless otherwise mentioned, all further calculations are in the ASA method. A large contribution to the bands crossing the Fermi level comes from the 5d-bands of Yb and the 4d-bands of Rh (Fig. 4.3).

According to the experimental evidence, Yb³⁺ in YbRh₂Si₂ is in a $4f^{13}$ configuration. Thus we need to improve upon the simple LDA method in order to check if one of the Yb³⁺ 4f-bands lies above the Fermi energy. Since the electrons on the Yb³⁺ ion are strongly correlated we will use the LDA+U method next to obtain the electronic structure.

4.3.2 LDA+U calculation

We used the LDA calculation to estimate the interaction energy required to push one of the 4f-bands from below to above the Fermi level. From the LDA calculation in the ASA case, we located the 4f sub-band (amongst all the 4f-bands) that has the highest energy at the Γ -point. It is most likely that it is this band that would be unfilled upon the inclusion of U. From Fig. 4.4, we can see that this band is the $4f:\{z(x^2-y^2)\}$ sub-band. Thus to obtain only 13 filled 4f-bands we use the correct initial partial occupancies in the DHUB matrix. We input a partial occupancy of 0

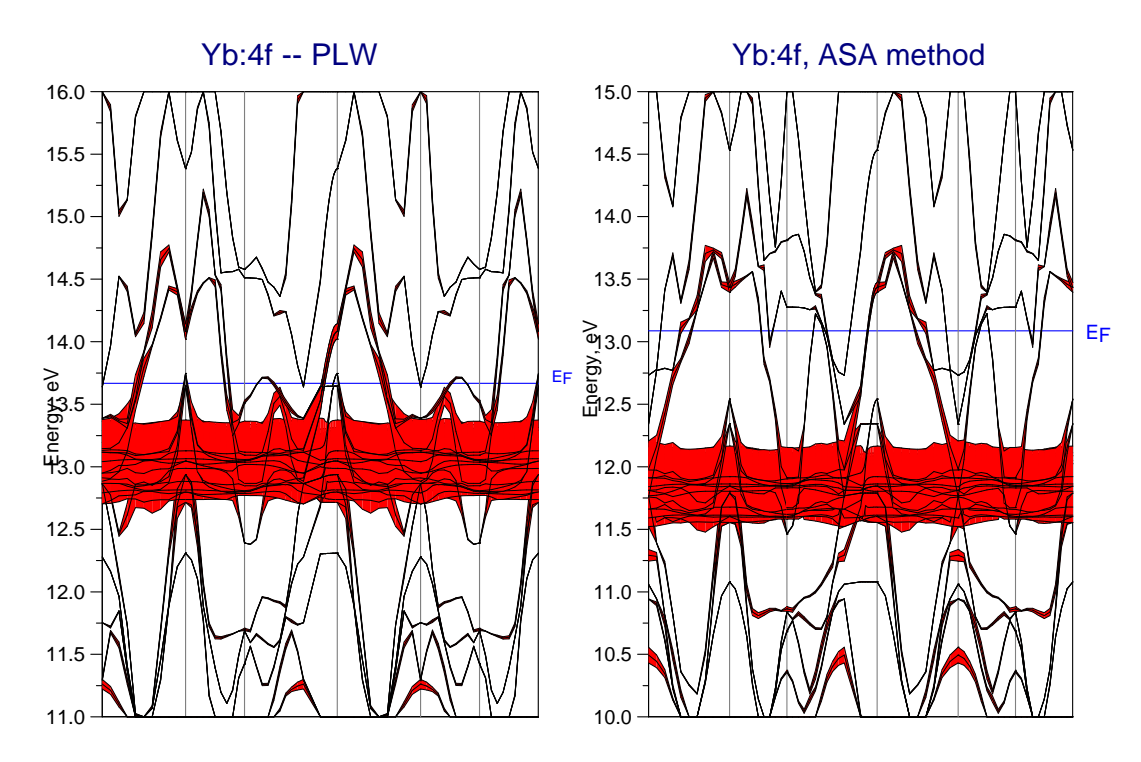


Figure 4.2: Energy bands of $YbRh_2Si_2$ – Full Potential(left) and Atomic Sphere Approximation(right). The colored regions in are the fat bands for Yb:4f.

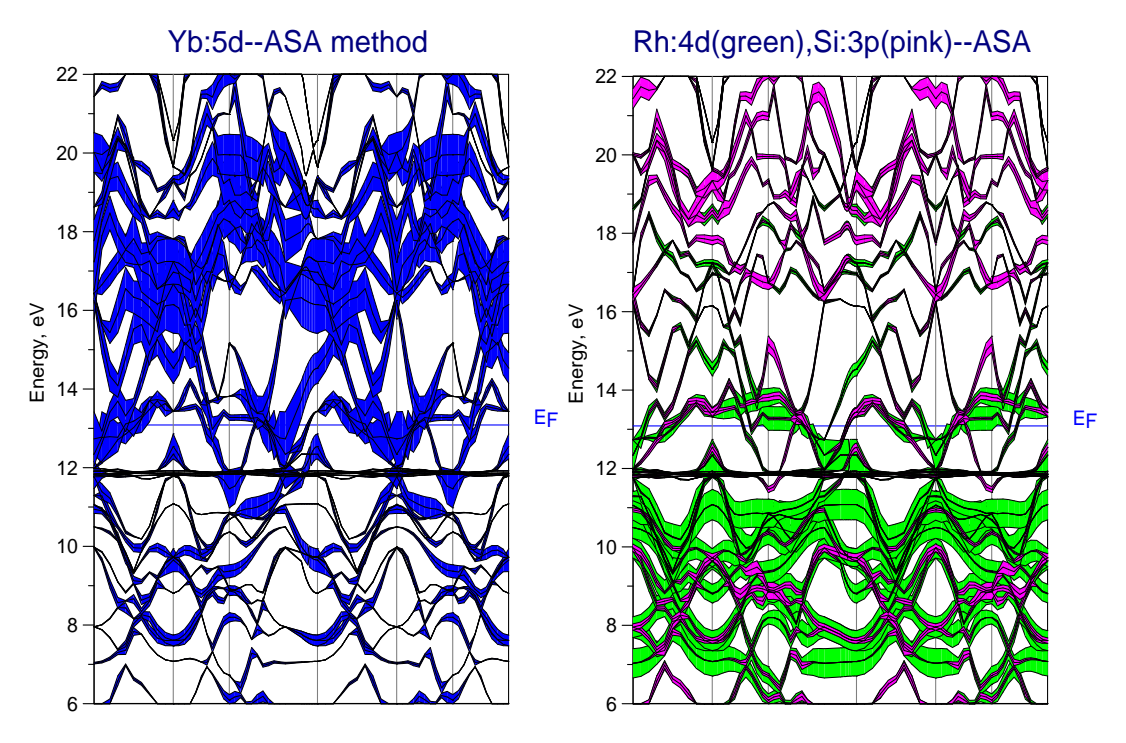


Figure 4.3: Energy bands of $YbRh_2Si_2$. The colored regions in are the fat bands for Yb:5d (left) and Rh(4d) and Si:3p(right).

for the $4f: \{z(x^2-y^2)\}$ —spin-up (an arbitrary choice, as spin-up and spin-dn bands displayed the same behavior) and a partial occupancy of 1 for the other sub-bands.

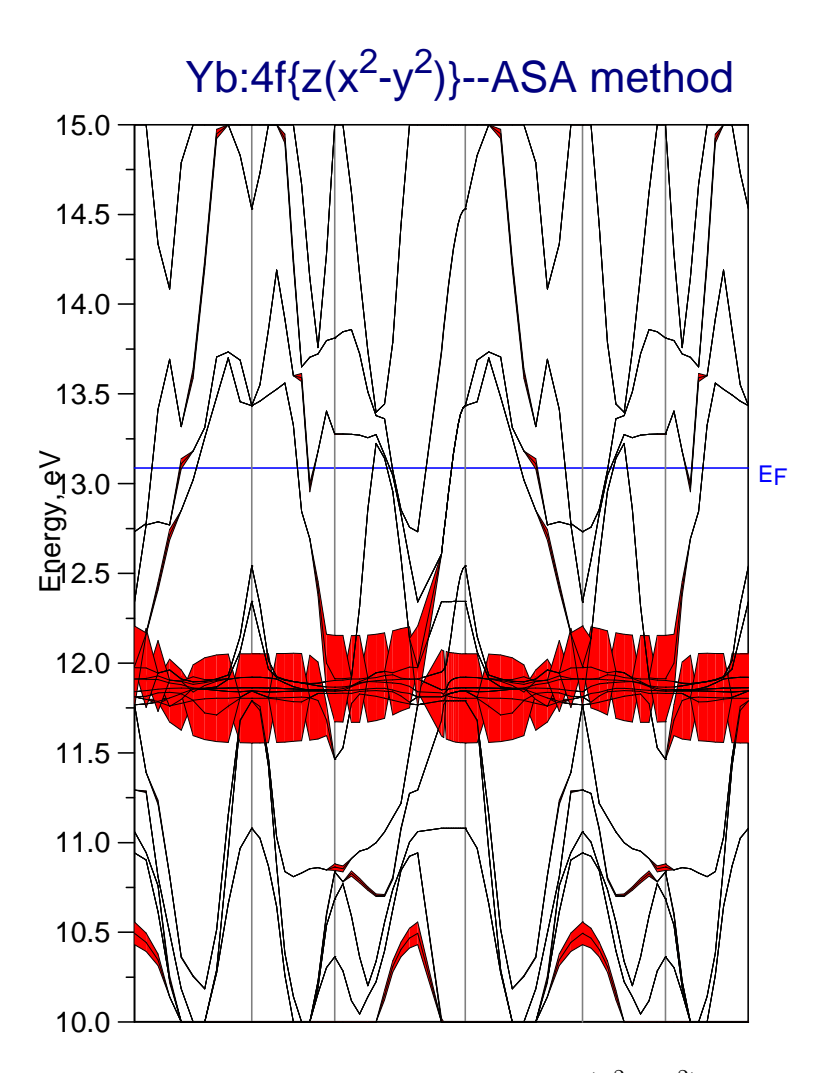


Figure 4.4: Energy bands of Yb: $4fz(x^2 - y^2)$

We find that even on increasing the value of U, we get all the 14 4f-bands of Yb to be filled. The results for U=2,4,6 and 8eV and are shown in Fig. 4.5 Self-consistency for the energy was obtained in 100 iterations.

Under the simple LDA calculation, all the 14 4f-bands of Yb are filled. We want to locate the magnetic solution with one of the 4f-bands to be pushed above the Fermi level. Fig. 4.6 shows the behavior of the position of the center of the f-band w.r.t. U. Thus in order to push one of the bands towards and above the Fermi level, we propose that the value of U used in the double counting term is different from that in

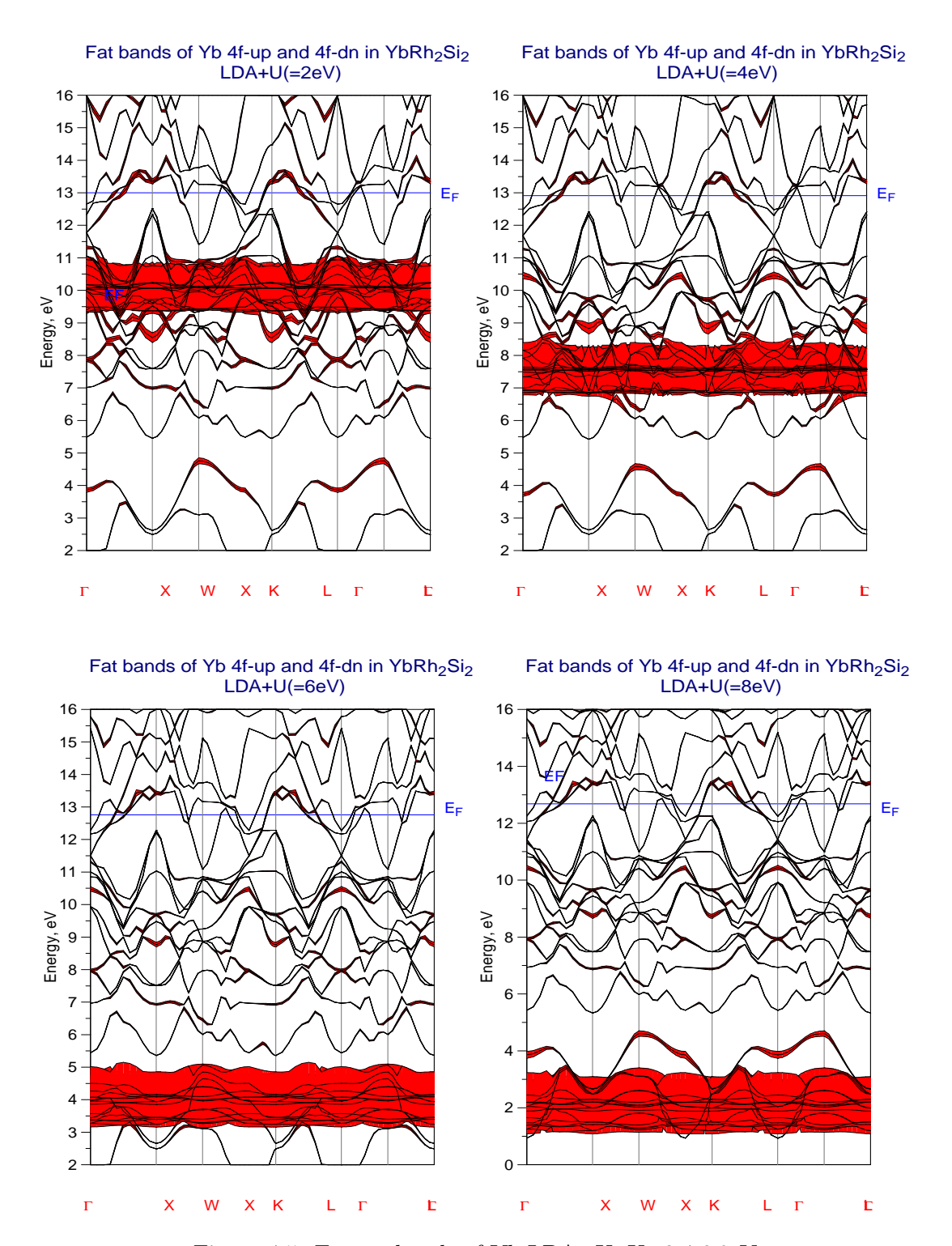
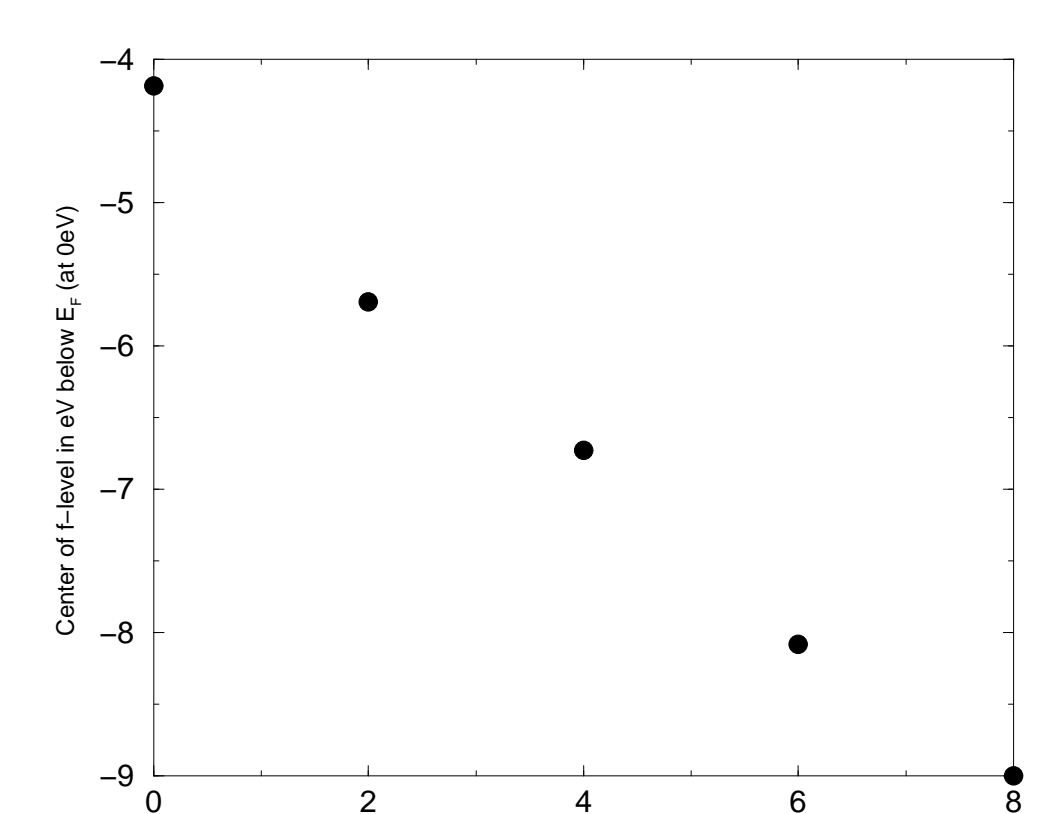


Figure 4.5: Energy bands of Yb:LDA+U, U=2,4,6,8eV



the LDA+U energy functional for the model.

Figure 4.6: Position of center of 4f-bands of Yb as a function of the interaction U

U (eV)

4.3.3 Effect of the double counting term:

Our prescription for obtaining the correct band structure for this material is that we treat the interaction U that is used in the model and the interaction \bar{U} used in the double counting term as two separate parameters. The former controls the position of the band below the Fermi level while the latter controls the splitting in energy between the occupied and the unoccupied bands, on which the magnetic moment depends. To test this hypothesis, we run the LDA+U calculation using different values of U and \bar{U} .

In Fig. 4.7 we plot the position of the 4f-level as a function of \bar{U} for the interaction U=4.0eV and U=6.0eV. Initially we keep $\bar{U}=U$. As we decrease \bar{U} (to $\bar{U}=5.5eV$ for U=6eV and to $\bar{U}=3.4eV$ for U=4eV) we find that the system has a magnetic

solution. These results are shown in Figs. 4.8 and 4.9 where we see that a part of the 4f-band of Yb is unoccupied and the Yb-ion shows a non-zero magnetic moment.

However, when we calculate the total magnetic moment, we find that it is less than the experimental value of $\sim 4\mu_B$. For this solution, our initial condition had, for the $4f:\{z(x^2-y^2)\}$ sub-band, an occupation number of 0 (for the spin-up electron), and for the other 4f-bands, an occupation number of 1. This led to a stable converged solution with a total occupation of 13.3 for the f-bands. However, magnetic moment (in units of Bohr magnetons μ_B) for this state was lower than the experimental one.

For $U = 6eV, \bar{U} = 5.5eV$:

Orbital moment $M_z = 0.4$

Spin moment = 1.16

Total moment = 1.56.

The difference is due to the contribution from the orbital angular moment. In the above state, the contribution came from the orbitals $l_z=+2,-2$. In order to obtain the correct angular moment, the initial state has to have the $l_z=+3$ orbital empty and the other orbitals filled. With this initial condition, we get a band structure as shown in Fig. 4.9. The magnetization for $U=6eV, \bar{U}=5.5eV$ is:

Orbital moment $M_z = 2.97$

Spin moment = 1.14

Total moment = 4.11

Thus, using the correct value of the interaction \bar{U} in the double-counting term, and the correct initial conditions in the occupancy matrix, we obtain a band structure for YbRh₂Si₂ that has the correct magnetic solution.

4.3.4 Comparison with other methods involving the double-counting term

In order to describe the physics of correlated metals, which fall in between materials which have fully localized shells, and those which have uniform electron occupancies, Mazin et.al [54] proposed an alternate form of the double counting term in the LDA+U

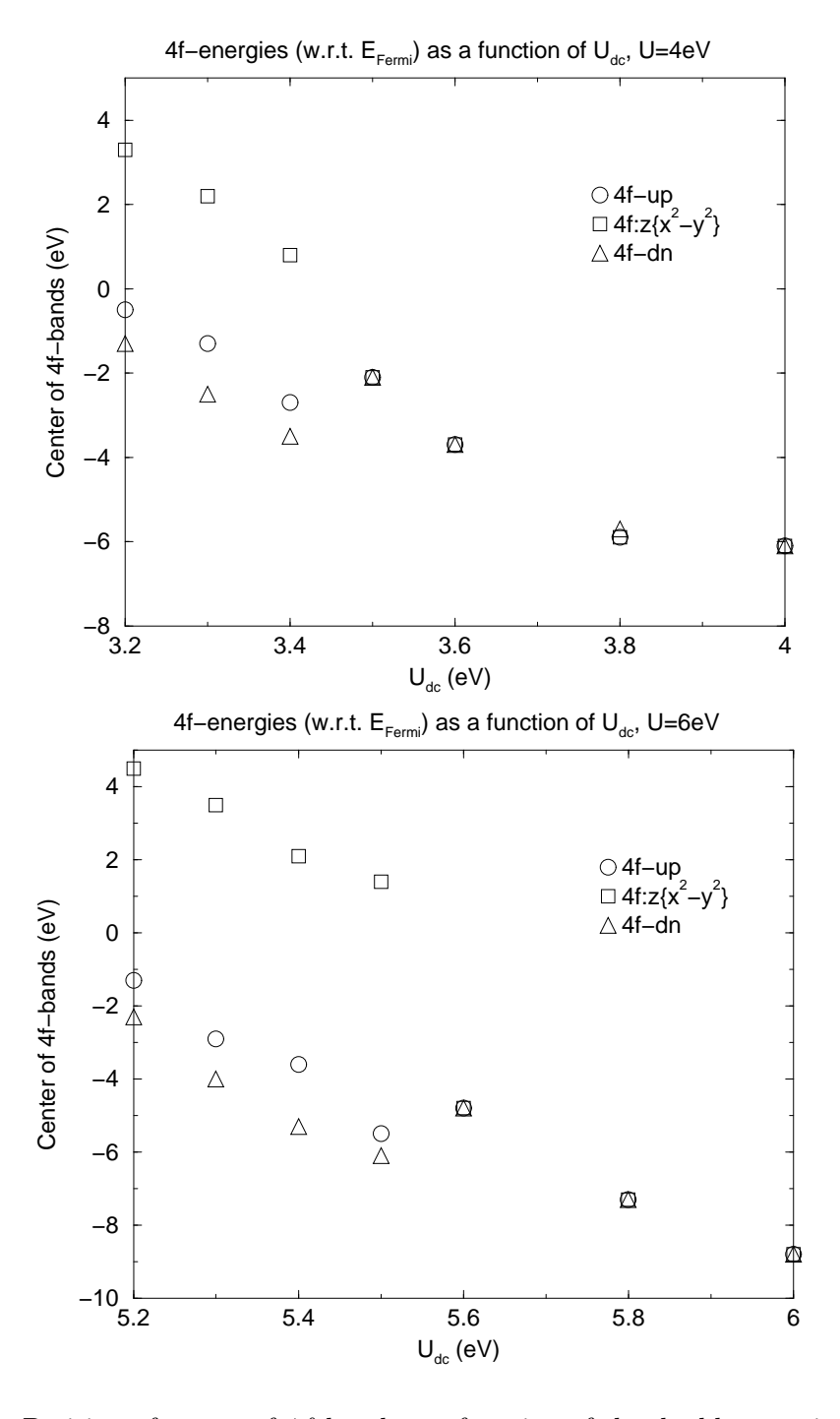


Figure 4.7: Position of center of 4f-band as a function of the double-counting term \bar{U} for U=4eV (top) and U=6eV(bottom)

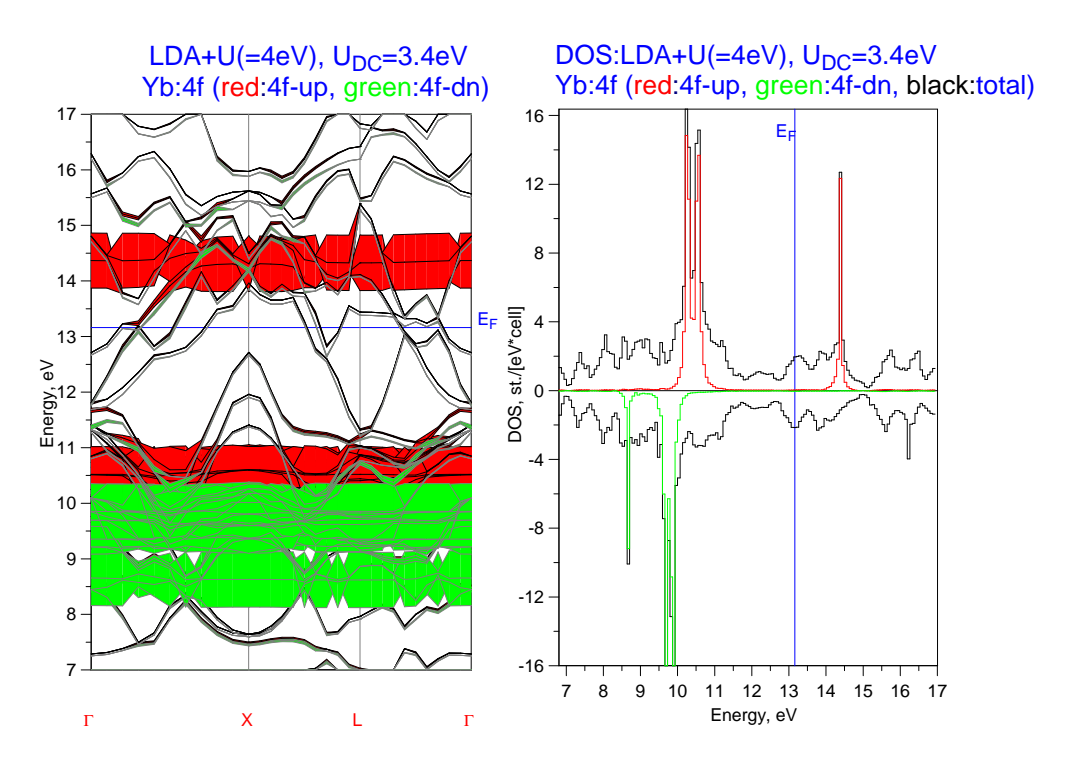


Figure 4.8: Energy bands(left) and DOS(right) of Yb:4f, LDA+U, U=4eV.

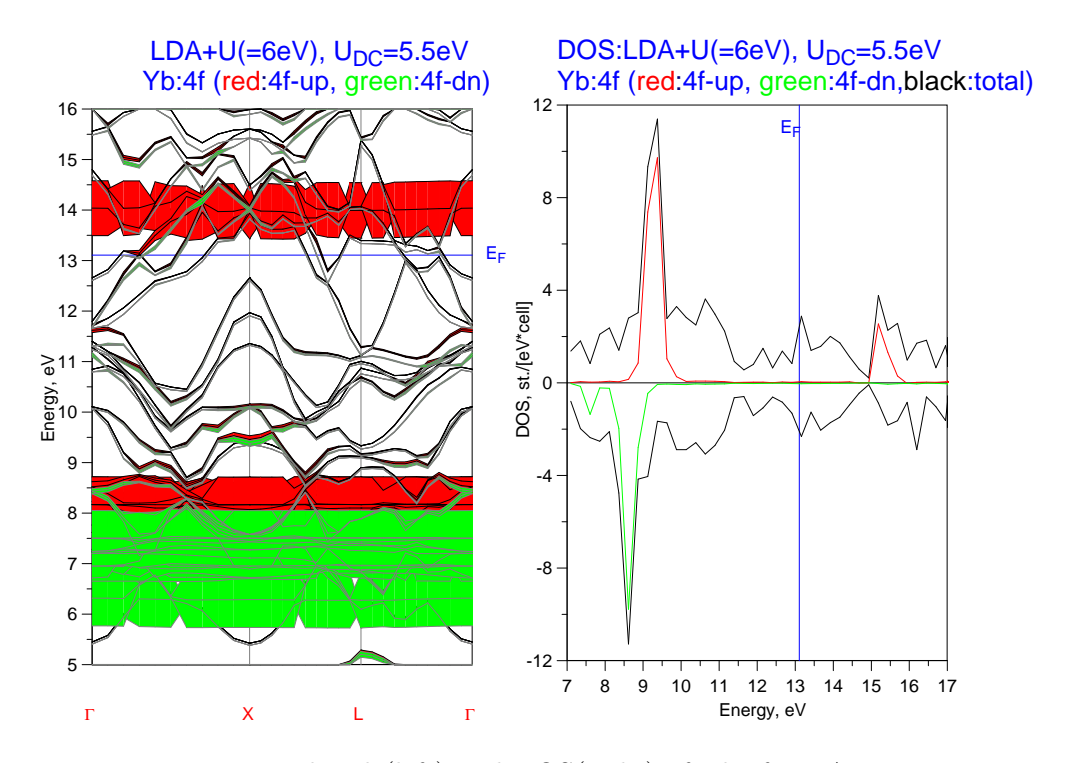


Figure 4.9: Energy bands(left) and DOS(right) of Yb:4f, LDA+U, U=6eV.

functional (c.f. Eqns. 3.18 and 3.19):

$$E_{LDA+U}^{DFT} = -\frac{(\bar{U} - \bar{J})}{2} \sum_{\sigma} \left[Tr(\rho^{\sigma} \cdot \rho^{\sigma}) - (2l+1) \left[\alpha_{\sigma} n_{\sigma}^{2} + (1 - \alpha_{\sigma}) n_{\sigma} \right] \right]$$
(4.1)

$$0 \le \alpha_{\sigma} = \frac{Tr(\delta \rho^{\sigma} \cdot \delta \rho^{\sigma})}{(2l+1) n_{\sigma} (1 - n_{\sigma})} \le 1$$

$$(4.2)$$

The correction to the potential is

$$\lambda_{LDA+U}^{DFT}(ab,\sigma) = -(\bar{U} - \bar{J}) \left[\rho_{ab}^{\sigma} - \alpha_{\sigma} n_{\sigma} - \frac{1 - \alpha_{\sigma}}{2} \right]$$
 (4.3)

Here, the orbital occupation matrix, $\rho_{ab}^{\sigma} = -1/\pi \int^{E_F} G_{ab}(E) dE$ where G_{ab} is the oneelectron Green's function, $n_{\sigma} = Tr \rho^{\sigma}/(2l+1)$ and $\delta \rho_{ab}^{\sigma} = \rho_{ab}^{\sigma} - n_{\sigma}$. α_{σ} is a system dependent constant between 0 and 1 that is calculated using the self-consistent occupation matrix at each iteration as in Eqn. 4.2 According to this scheme, our LDA+U calculation has a double counting term in eqn.3.19 as $(\rho_{ab}^{\sigma} - \frac{1}{2}\delta_{ab})$ that is equivalent to keeping the value of $\alpha = 0$.

We tested the above functional for our calculation on YbRh₂Si₂. We replace the original double-counting term (eqn.3.19) in the file $hub \, Jubpot.f$ by the one above. We find that this double-counting term does not produce a magnetic ground state for YbRh₂Si₂. Fig. 4.10 shows how the 4f-bands of Yb in YbRh₂Si₂ behave as a function of U using the scheme descibed above. From the self-consistent procedure we get a value of $\alpha = 0.22$. Also included in the figure are the location of the bands using the original double-counting with $U = \bar{U}$, as well as the result from our empirical method of treating U and \bar{U} as different parameters. We see that using the functional described by Mazin, the center of the bands move in the correct direction, however we still do not obtain the correct magnetic ground state. For that we must follow the method we described in section 4.3.3 where we treat the interaction \bar{U} as a different parameter from the interaction U in the model.

In yet another functional for the total energy proposed by Czyzyk and Sawatzky [55], the double counting term to be subtracted from the potential is given by $(\rho_{ab}^{\sigma} - n^{\sigma}\delta_{ab})$ which corresponds to the limit of uniform occupancy in LDA, i.e. $\rho_{ab}^{\sigma}(LDA) = \delta_{ab}n^{\sigma}$. For correlated materials, the limit of uniform occupancy is not correct, hence this method of treating the double counting term produces the incorrect ground state for YbRh₂Si₂.

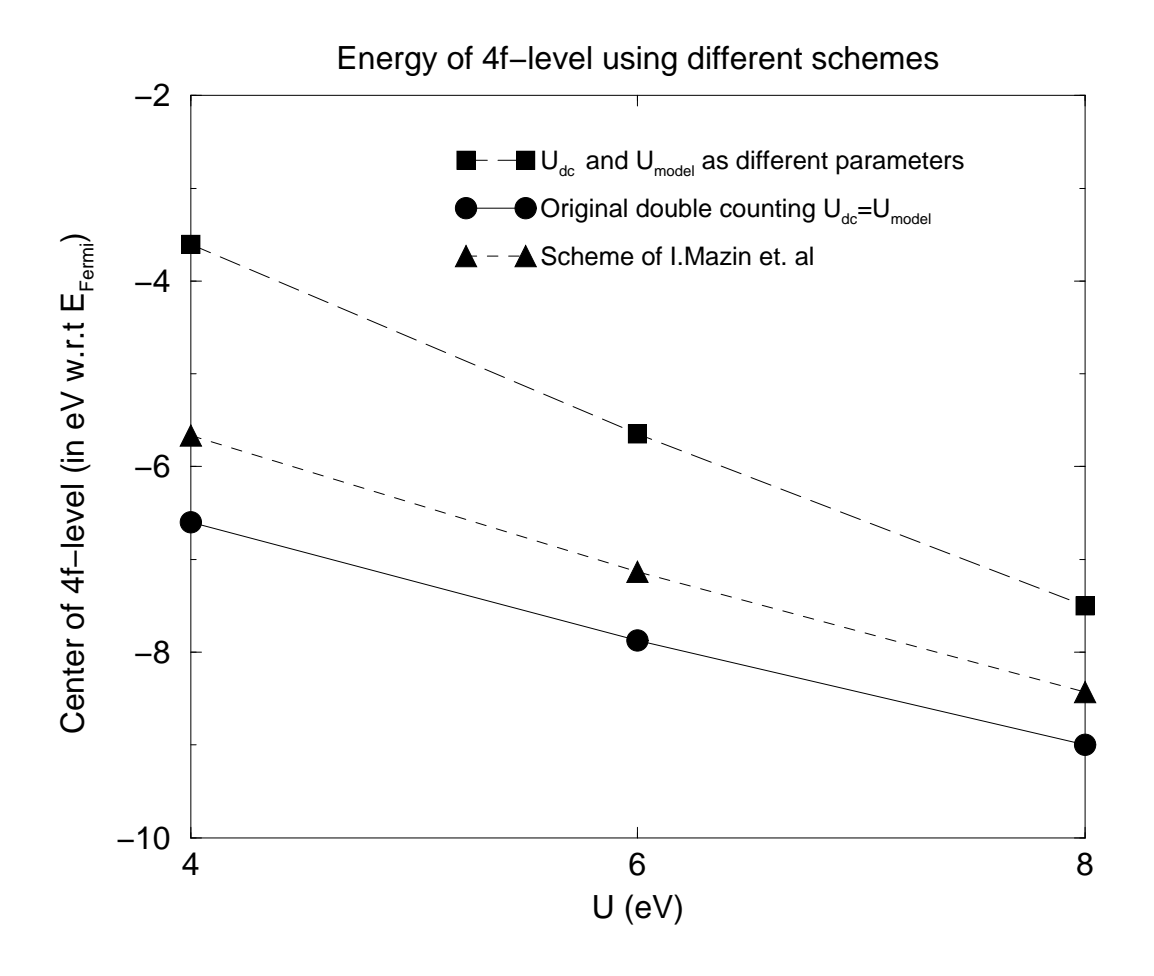


Figure 4.10: Location of the 4f-bands in various schemes. The original double-counting where $U=\bar{U}$ and the one used by Mazin et.al [54] as described above do not predict a magnetic ground state. The empirical method described in section 4.3.3 does predict the correct ground state.

4.3.5 Effects of pressure

If we apply pressure, we expect that the f-level moves closer to the Fermi level. If sufficient pressure is applied, we expect some of the f-bands to cross the Fermi level so the material has a magnetic solution. To incorporate the effects of pressure, we decrease the volume compression factor V/V_0 from its original value of 1. We find that there is an overall increase in all the energies observed, including the Fermi level. When pressure is increased by $\sim 10\%$, the center of the 4f-band moves up by $\sim 12\%$ but the Fermi level increases by about as much. Hence we do not observe a magnetic solution

with the application of pressure alone.

Once we have obtained the correct magnetic solution by using the appropriate value of the double-counting term and the interaction term, we find that on applying pressure, the gap between the occupied and the unoccupied states decreases, leading to a decrease in the magnetization. As pressure is applied, the volume of the muffin-tin spheres decreases which causes a decrease in the effective interaction. The Hubbard bands come closer and the magnetic moment decreases. Fig. 4.11 shows this trend. The band structures for the magnetic solution on applying pressure are shown in Fig. 4.12.

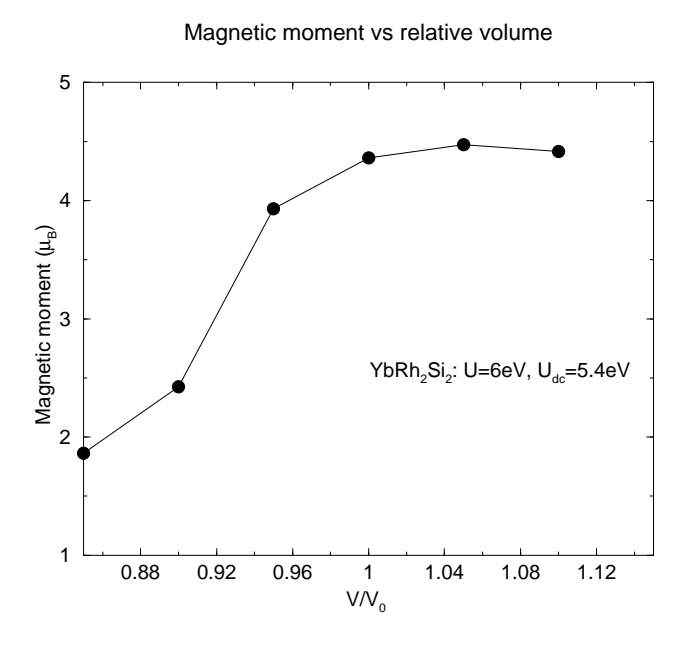


Figure 4.11: Dependence of magnetic moment on relative volume

4.3.6 Anti-ferromagnetic solution

Experimentally YbRh₂Si₂ is in an anti-ferromagnetic state. To obtain the anti-ferromagnetic solution and the band structure, we have to first incorporate the correct crystal structure in the input files. In the ferromagnetic case, each unit cell has one Yb atom, which is located at the origin. To have an anti-ferromagnetic solution, we have to double the unit cell so that it contains two Yb atoms. Adjacent Yb atoms have opposite spins. The following table shows the input structure file that shows the basis atoms and the

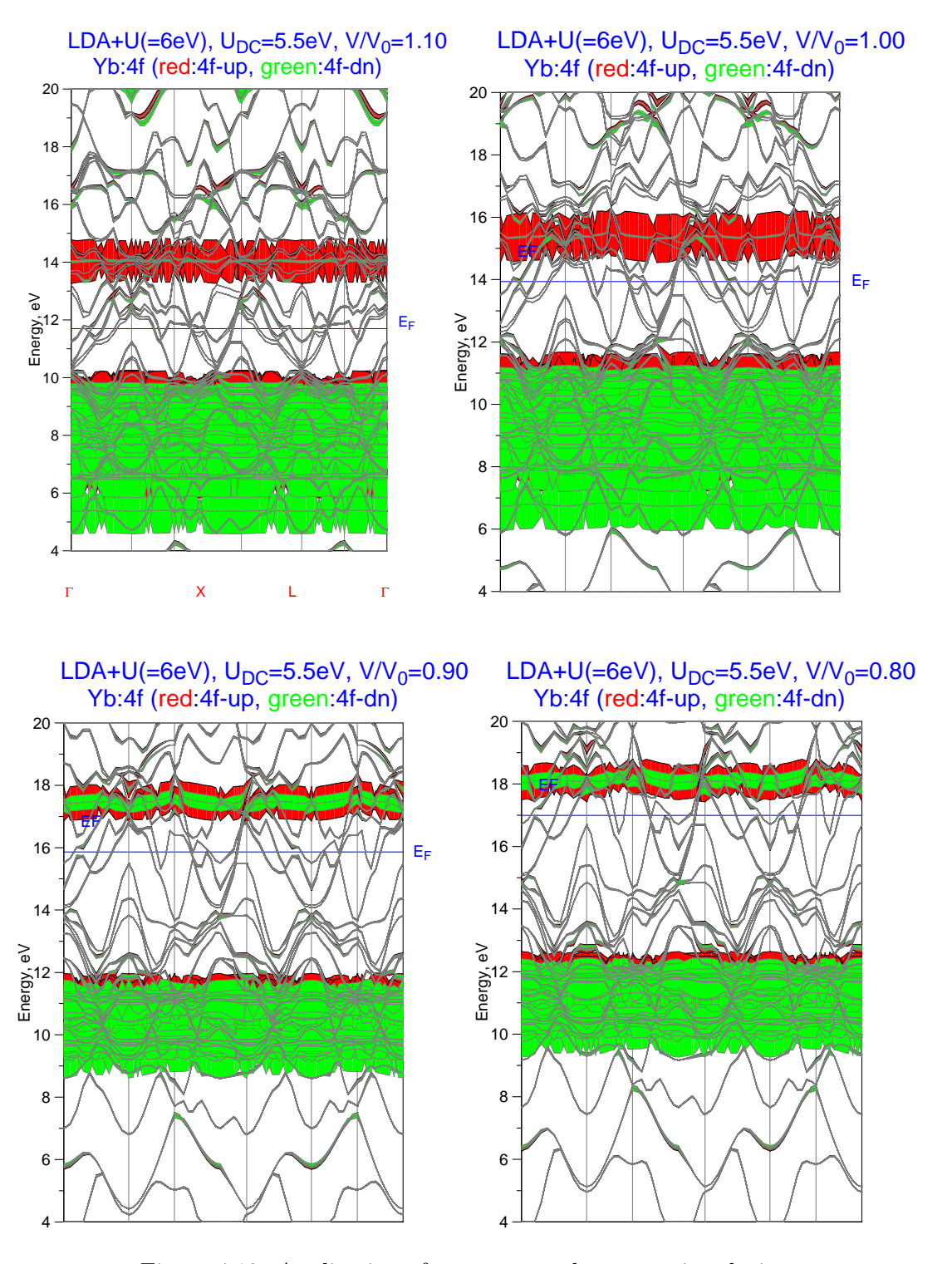


Figure 4.12: Application of pressure on the magnetic solution

positions of the atoms. (Compare with structure file in Table 4.1)

```
⟨FILE=STRFILE⟩
⟨SECTION=HEDS⟩
                                            ! STRUCTURE TITLE:
Slabl = YbRh2Si2
⟨SECTION=CTRS⟩
                                            ! CONTROL STRUCTURE:
Natom = 10
                                            ! # of atoms
BtoA = 1.00000
                                            ! b over a ratio
CtoA = 2.46019
                                            ! c over a ratio
⟨SECTION=TRAN ⟩
                                            ! PRIMITIVE TRANSLATIONS:
1, 1, 0
                                            ! Ax,Ay,Az
1, -1, 0
                                            ! Bx,By,Bz
1/2, 1/2, 1/2
                                            ! Cx,Cy,Cz
⟨SECTION=BASS⟩
                                            ! BASIS ATOMS :
0.0 , 0.0 , 0.0
                                            ! Yb1
1.0, 0.0, 1.0
                                            ! Yb2
0.0 , 1/2 , 1/4
                                            ! Rh1
1/2, 0.0, 1/4
                                            ! Rh2
1.0, 1/2, 1/4
                                            ! Rh3
3/2 , 0.0 , 1/4
                                            ! Rh4
0.0, 0.0, 3/8
                                            ! Si1
                                            ! Si2
0.0, 0.0, 5/8
1.0, 0.0, 3/8
                                            ! Si3
1.0, 0.0, 5/8
                                            ! Si4
```

Table 4.4: Input file ybrh2si2.str

The interaction parameters we used were $U=6 \, \mathrm{eV}, \ \bar{U}=5.5 \, \mathrm{eV}.$ The magnetic moment (in units of Bohr magnetons) in this case is as follows:

Orbital magnetic moment for 1st Yb atom (spin-up): 2.959937

Orbital magnetic moment for 2nd Yb atom (spin-dn): 2.667827

Spin magnetic moment for 1st Yb atom (spin-up): 1.112074

Spin magnetic moment for 2nd Yb atom (spin-dn): 0.923587

Fig. 4.13 shows the energy bands of YbRh₂Si₂ in the anti-ferromagnetic calculation.

4.4 Magnetic Anisotropy Energy

YbRh₂Si₂ shows a highly anisotropic magnetic response along different crystallographic directions. The experimentally measured magnetic susceptibility (Fig. 4.14 from [59])

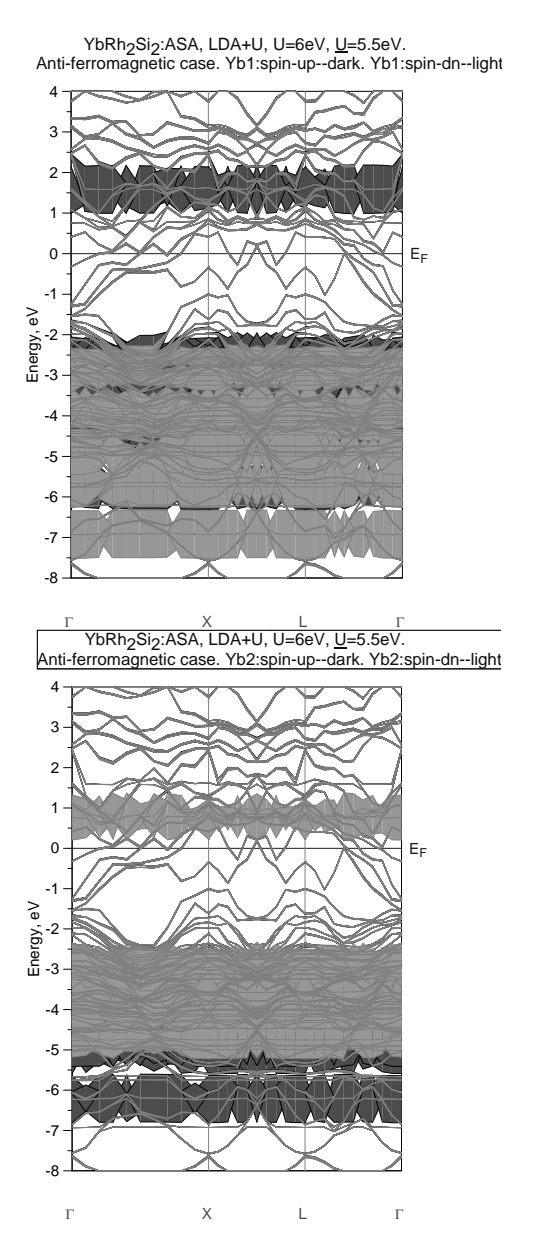


Figure 4.13: Energy bands of Yb in the anti-ferromagnetic case. Top: Bands of Yb-1 atom. Bottom: Bands of Yb-2 atom

along the plane of the tetragonal structure is $\simeq 20$ times larger than that measured along the perpendicular c axis at 2 K and upto 100 times larger at 0.1K according to Trovarelli et. al. [53], [59]. The magnetic anisotropy energy (MAE) is defined as the difference of the total energies with the orientation of the magnetization pointing in different crystalline directions. Since it depends on the total energy, the MAE is a ground state property and hence can be calculated using density functional theory.

To calculate the MAE, we calculate the total energy with the magnetic axis pointing in two different directions – [100] corresponding to the z-axis in the crystal and [110], corresponding to the X-Y plane. In practice, we implement this as explained below.

We first start with the converged paramagnetic solution that we obtain with LDA+U. To obtain the solution with the magnetization along the c-axis of the crystal, which is also our z-direction, we set the parameter AxMag = 0, 0, 1 in the input file ybrh2si2.ini. We also use the correct initial values in the occupancy matrix with the magnetic axis in the [100] crystallographic direction. We calculate the total energy with these conditions as E_c . The magnetization obtained is in the z-direction.

To calculate the total energy in the [110] crystallographic direction, that is, along the basal a-b plane of the crystal, we set AxMag = 1, 1, 0 in the input file ybrh2si2.ini. We also have to rotate the initial occupancy matrix, so that the orbital and the spin magnetic moments both point along the x-y plane. We calculate the total energy E_a in this configuration. The difference of the energies in the above two configurations is the MAE.

We first compute the magnetic anisotropy energy using the **ferromagnetic** solution. We use 12 k-points per dimension in the Brillouin zone.

For the magnetization along the c-axis, total energy $E_c = -48409.504501$ Ry. Here, magnetic moment $M_z = 1.08 \mu_B$ and $M_x, M_y << M_z$.

For the magnetization along the a-b plane, total energy $E_a=-48409.504513$ Ry. Magnetic moment $M_x=M_y=0.48202~\mu_B$ and $M_z<< M_x, M_y$.

The magnetic anisotropy energy per Yb atom is

$$MAE = E_a - E_c = -1.32 \times 10^{-5} Ry \simeq -179.5 \mu eV$$

Thus $E_a < E_c$, that is, the configuration where the spins point along the x-y plane is more stable, as confirmed by experiment.

Experimentally we know that the magnetic susceptibility $\chi_a \simeq 20\chi_c$ at a field of 5T and temperature of 2K (Fig. 4.14 from [59]). Here χ_a is the susceptibility along the plane of the tetragonal structure and χ_c is that perpendicular to the plane, i.e. along the c-axis. To compare the magnetic anisotropy energies in our LDA+U calculation, as compared to the experimental value, we do a calculate the experimental value of the magnetic anisotropy energy given the susceptibility.

We have

$$E = -\frac{1}{2} \frac{M^2}{\chi} \tag{4.4}$$

where E is the energy, M is the magnetization and χ is the susceptibility. The magnetic anisotropy energy $MAE = E_a - E_c$.

From the plots in Figs. 4.14 and 4.15 obtained from [58] and [59] at a field of 5 T and temperature 2 K we have:

$$M_a = 0.73 \mu_B/atom, M_c = 0.1 \mu_B/atom$$

$$\chi_a = 1.0 \times 10^{-6} m^3 / mol, \quad \chi_c = 0.1 \times 10^{-6} m^3 / mol$$

Converting all quantities so that the value are per atom, we have

$$\chi_a = \frac{1.0 \times 10^{-6} m^3 / mol}{6.023 \times 10^{23} atoms / mol} = 1.66 \times 10^{-30} m^3 / atom$$
 (4.5)

$$\chi_c = \frac{0.1 \times 10^{-6} m^3 / mol}{6.023 \times 10^{23} atoms / mol} = 1.66 \times 10^{-31} m^3 / atom$$
 (4.6)

MAE per atom =
$$E_a - E_c = -\frac{1}{2} \left(\frac{M_a^2}{\chi_a} - \frac{M_c^2}{\chi_c} \right)$$

= $-\frac{1}{2} \left(\frac{(0.73\mu_B/atom)^2}{1.66 \times 10^{-30} m^3/atom} - \frac{(0.1\mu_B/atom)^2}{1.66 \times 10^{-31} m^3/atom} \right)$
= $-\frac{1}{2} \times \left(3.166 \times 10^{29} (\mu_B)^2/m^3 - 6.024 \times 10^{28} (\mu_B)^2/m^3 \right)$
= $-1.282 \times 10^{29} (\mu_B)^2/m^3$

(4.7)

Using the value of the Bohr magneton, $1\mu_B = 9.274 \times 10^{-24} J/T$, and the conversion $1(\mu_B)^2/m^3 = (9.274 \times 10^{24} J/T)^2 \times \mu_0 = 1.079 \times 10^{-52} J$ we get

MAE per atom =
$$E_a - E_c = -1.384 \times 10^{-23} J/atom$$

= $-8.65 \times 10^{-5} eV/atom$ (4.8)

When we compute the total energy for the **anti-ferromagnetic** solution, by doubling the unit cell, we get total energy $E_c = -96819.024913$ when the magnetization is along the c-axis of the crystal. With the magnetization pointing along the a-b plane, we get the total energy $E_a = -96819.024942$. Since each unit cell has two Yb atoms, the magnitude of the MAE per Yb atom is $|E_a - E_c|/2 = (2.9 \times 10^{-5})/2 = 1.45 \times 10^{-5} Ry \simeq 200 \mu eV$.

The typical order of magnitude of magnetic anisotropy energies are a few μeV per atom. For example, MAE per atom at low temperature for Fe is 1.4 μeV , for Ni is 2.7 μeV and for Co is 60 μeV . In comparison, from our LDA+U calculation, we have, MAE per Yb atom in YbRh₂Si₂ to be $\simeq 200\mu eV$ and the experimental value for YbRh₂Si₂ per Yb atom is $\simeq 86.5\mu eV$ with $E_a < E_c$, that is, the configuration where the magnetization is along the a-b plane being more stable.

We also calculate the exchange energy using the total energies per atom for the ferromagnetic and the anti-ferromagnetic case in the two directions.

Parallel to a-b plane:

$$E_a^{Ferro} - E_a^{Antiferro} = -48409.504513 - (-48409.512471) = 0.07958Ry$$

Perpendicular to a-b plane, i.e. along c-axis:

$$E_c^{Ferro} - E_c^{Antiferro} = -48409.504501 - (-48409.512456) = 0.07955Ry$$

4.5 Summary and Conclusions

We used LDA and LDA+U methods to compute the band structure of YbRh₂Si₂. Both methods predict an incorrect non-magnetic structure with all the above 4f-shells occupied. Experimentally YbRh₂Si₂ is in an anti-ferromagnetic state with a total magnetic

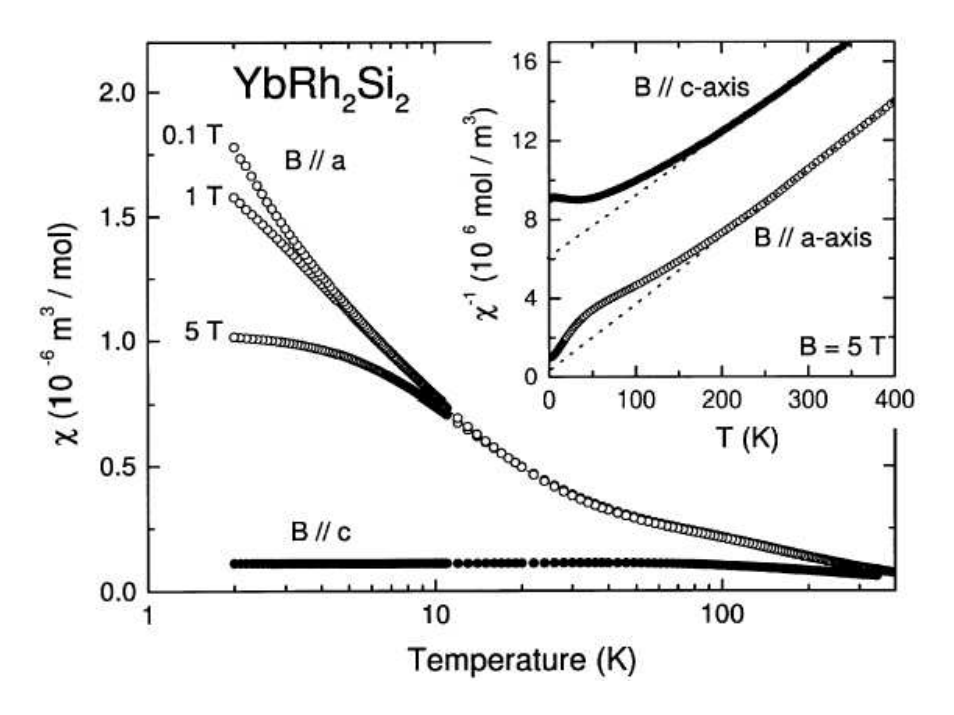


Figure 4.14: χ vs T (from Trovarelli et.al. [59])

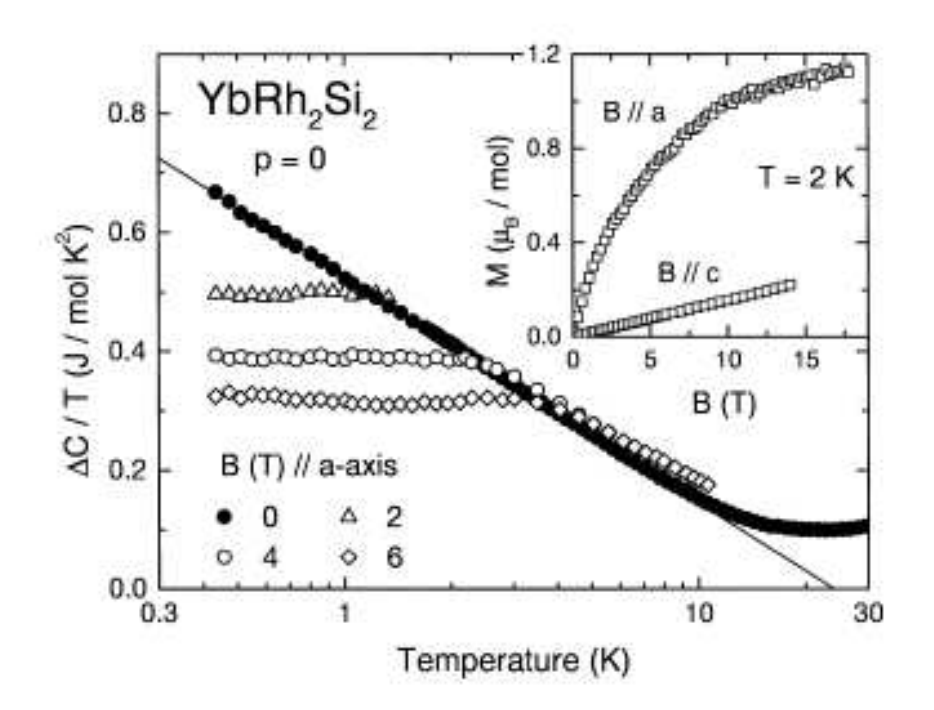


Figure 4.15: from Trovarelli et.al. [58]

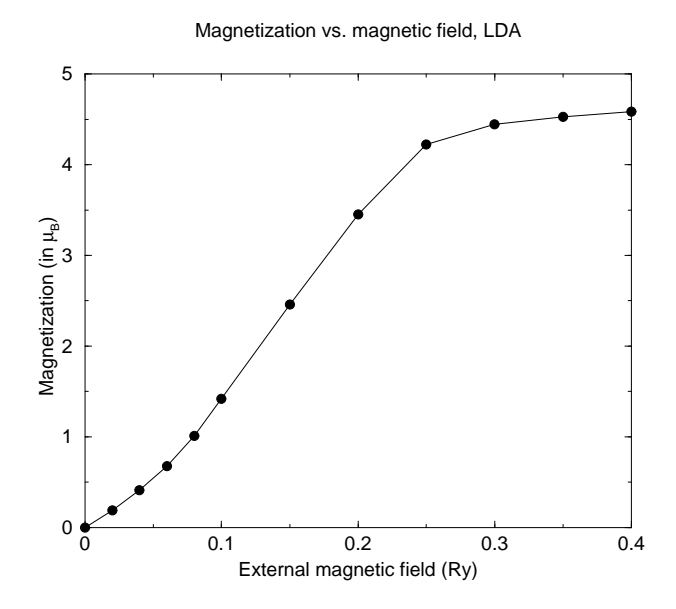


Figure 4.16: Magnetization as a function of external magnetic field (along z-axis)

moment of $\sim 4.5\mu_B$. In order to obtain the correct magnetic solution, we proposed that the value of U used in the double counting term, U_{dc} , is different from that in the energy functional. When U_{dc} is decreased, keeping U fixed, we do observe that the $4f:\{z(x^2-y^2)\}$ sub-band of Yb gets unoccupied as per the initial condition.

The magnetic anisotropy energy of YbRh₂Si₂ is calculated using the difference of the total energies with the magnetization pointing in two different directions. Our calculations show that YbRh₂Si₂ is a highly anisotropic material, as was observed in experiments.

Chapter 5

Electronic structure and properties of f-band materials: Americium

5.1 Introduction

In this chapter, we use LDA+U and LDA+DMFT methods described in chapter 3, to study the electronic structure and properties of Americium, another material which has occupation in the f-shell.

Experiment and motivation:

Americium is a metal that is nearly in the center of the actinide series, which have occupation in the 5f shell. The actinides show interesting behavior in terms of crystal structure and atomic volumes as one moves across the series. The lighter actinides until Pu are known to have delocalized 5f-electrons that participate in bonding. They have open low-symmetry structures. On the other hand, the 5f-electrons in the heavier actinides are localized and the materials have closed structures.

Fig. 5.1 shows the volume change as one moves across the actinide series. One can see that Americium is at a pivotal position. There is a sudden change in the atomic volume as one moves from Pu to Am across the actinide series. This jump in volume is argued to be a Mott transition with the 5f-electrons localized in Am, and itinerant in the preceding element, Plutonium. A natural question we can ask at this point is whether an external parameter such as pressure cam change the character of the 5f-electrons in Am.

Am has strong spin-orbit coupling due to which it is in a non-magnetic J=0 ground state. Experimentally, the photoemission spectra of Am has been studied by Nagele [60], which shows a localized 5f-peak (Fig. 5.2,left).

Actinides: Experimental atomic volumes

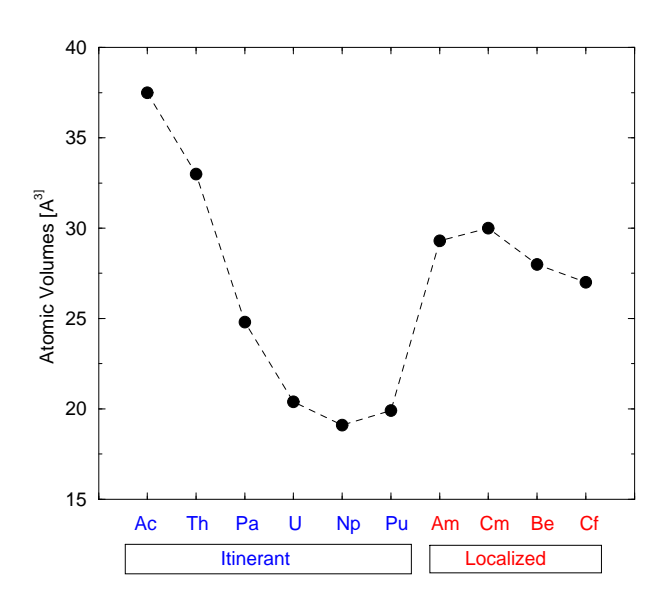


Figure 5.1: Volumes of actinide elements

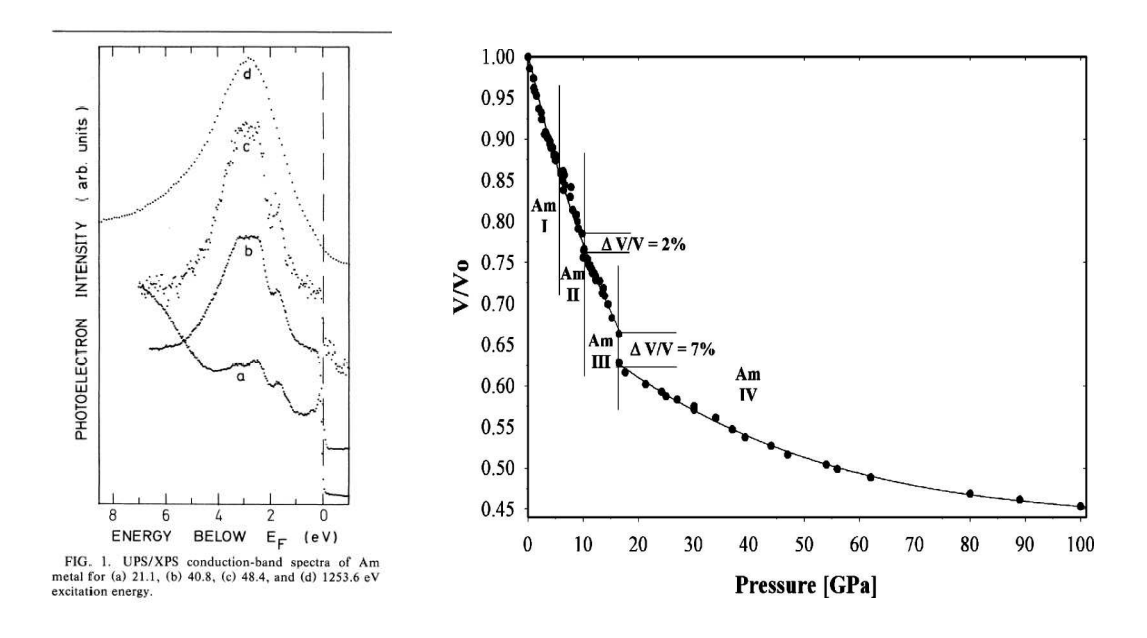


Figure 5.2: Left: Photoemission spectra of Am by Naegele [60]. Right: Relative volume of americium as a function of pressure obtained by Lindbaum et. al. [62]

Experimental studies have indicated [61], [62] that pressure induces major changes in the nature of the 5f electrons of Americium. At normal pressure, the 5f electrons of Americium are localized. With the application of pressure, the f electrons acquire an itinerant character. There has been considerable debate in literature about the volume of Americium in its various phases. From the high pressure studies using synchrotron radiation as described by Heathman et. al. in Ref. [61] Americium has 4 phases. At ordinary pressures Americium has a double hexagonal close packed (dhcp) structure which under application of pressure gets converted to the Americium II fcc structure at 6 GPa. This transition was reported to occur at higher pressures of 10 GPa by Benedict et. al. [63]. With additional pressure Americium II transforms to the Americium III phase accompanied by a volume collapse of 7% [61] which indicates that the f electrons begin to get delocalized (Fig. 5.2, right). The goal of this study is to test the predictions of the LDA+DMFT technique regarding the electronic structure, equilibrium atomic volume and the Mott transition in Am.

Theoretical studies:

Previous density functional electronic structure calculations in Americium [64], [65], [66] have shown that Americium has localized 5f-electrons at normal pressure with a FCC crystal structure. Application of high pressure leads to a phase with open, low symmetry structures which are accompanied by a delocalization of the 5f-electrons. However there has been some debate about the exact structure that Americium is calculated to have at high pressures. Two contenders have been the orthorhombic (α -Uranium) structure [64] or the monoclinic (α -Plutonium) structure [65], [66]. A discrepancy in all the previous theoretical studies is that the calculated volume collapse for the transition is much higher than the experimental value.

Eriksson and Wills [64], calculate the total energy versus volume of Americium in FCC and the α -U structures using relativistic full-potential LMTO methods. The basis set used in this computation contains 6s, 6p, 7s, 7p and 5f orbitals. On applying pressure, they calculate a transition from Am-II (FCC) to Am-III (α -U) accompanied by a volume collapse of 34%.

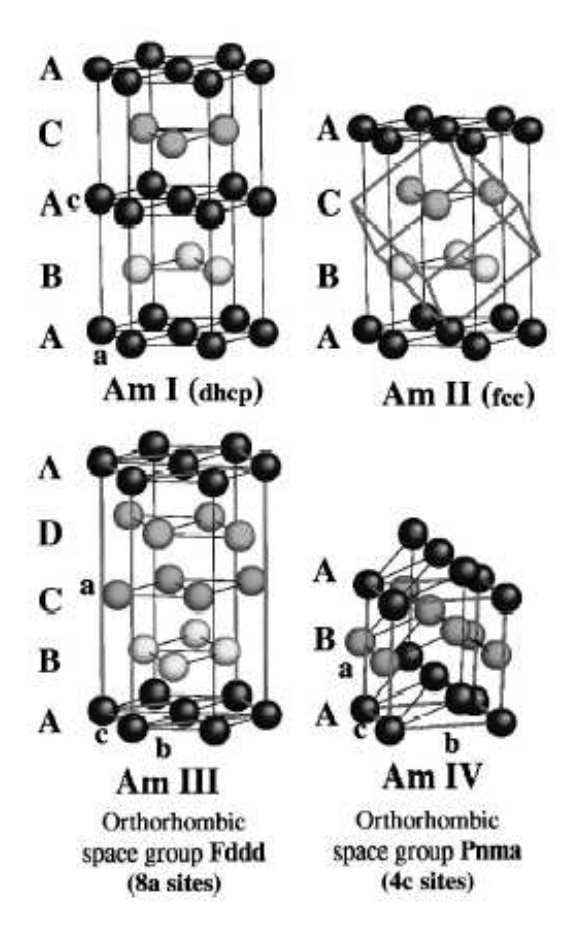


Figure 5.3: Four phases of Americium (Lindbaum et. al [62])

According to Soderlind et.al [65], however, the stable phase at high pressure is determined to be the monoclinic, i.e. the α -Pu structure. In this calculation, the total energies of six different crystal structures of Americium is determined as a function of volume. A full-potential LMTO method using the generalized gradient approximation for the exchange-correlation term is used. Spin degeneracy is assumed for all the structures except the FCC structure. The results show that on applying pressure, there is a transition from the FCC-Americium to monoclinic-Am accompanied by a volume collapse of 25%.

The theoretical calculations of Eriksson [64] and Soderlind *et.al* [65] underestimate the equilibrium volume of Americium at normal pressure. The volume of FCC-Americium is calculated to be 15% less than the experimentally determined volume by

Benedict [63]. Soderlind et.al also compute the total volume of Americium by treating the 5f electrons as core: in this calculation, the equilibrium volume at normal pressure is closer to the experimental volume, but still differs by 10%.

In the study by Pénicaud [66], the total energy versus atomic volume of Am is calculated in various structures. The normal phase is the FCC structure as in the previous calculations. At high pressures, the stable phase is calculated to be the α -Pu phase. On further applying pressure, a transition to the Am-IV structure is observed, which remains stable upto very high pressures. The equilibrium volume of Am at normal pressure in this study is close to the experimental value. The volume collapse for the FCC- α -Pu transition is calculated to be 31%.

In our calculation, we use the LMTO method in the atomic sphere approximation. We calculate the band structure for FCC-Americium in the LDA+U scheme, and we find that for a certain interaction U and double counting term, we can correctly predict the position photoemission peak. Further, our LDA+U computation of the equilibrium volume is in close agreement with experiment. However, using the LDA+U method, we do not get the correct magnetic moment of zero. We then use the LDA+DMFT technique using the Hubbard-I impurity solver to compute the band structure of Am, which should also predict the correct magnetic moment.

In section 5.2, we describe the details of the LDA+U computation of the band structure and density of states. section 5.2.2 deals with the equilibrium volume calculation. In section 5.3 we discuss the LDA+DMFT method, and apply it to calculate the bands in Am. Finally, our conclusions are stated in section 5.4.

5.2 LDA and LDA+U band structure calculation of Americium

The computation of the band structure is done using the LmtART code. The details of the calculation are as follows:

There are two input files required for the LDA calculation and an additional input file for the LDA+U calculation. The files are shown in the following tables. Table 5.1 has details of the crystal structure including the positions of the basis atoms and the lattice vectors. We used the FCC structure of Americium throughout our calculation. Table 5.2 contains the scheme used to calculate the self-consistency, the number of iterations in the self-consistent loop, atomic numbers and the lattice constant in atomic units. We used the atomic sphere approximation (ASA) scheme to achieve self-consistency. In order to obtain a well converged charge density and magnetization, we used the Broyden mixing scheme. For the LDA+U calculation, the details of the correlated orbitals and the interaction U are contained in Table 5.3. The band structure of Americium was calculated at various values of the interaction strength U.

```
⟨ FILE=STRFILE,INPUT=MODERN ⟩
************
⟨SECTION=HEDS⟩
                                                   ! STRUCTURE TITLE:
Slabl = Am
⟨SECTION=CTRS⟩
                                                   ! CONTROL STRUCTURE:
Natom = 1
                                                   ! # of atoms
BtoA = 1.00000
                                                   ! b over a ratio
CtoA = 1.00000
                                                   ! c over a ratio
                                                   ! PRIMITIVE TRANSLATIONS:
(SECTION=TRAN)
0.0, 1/2, 1/2
                                                   ! Ax,Ay,Az
1/2, 0.0, 1/2
                                                   ! Bx,By,Bz
1/2, 1/2, 0.0
                                                   ! Cx,Cy,Cz
⟨SECTION=BASS⟩
                                                   ! BASIS ATOMS :
0.0, 0.0, 0.0
                                                   ! Am
```

Table 5.1: Input file am.str

```
⟨FILE=INIFILE, INPUT=MODERN ⟩
************
⟨SECTION=HEAD⟩
                                         ! PROJECT HEAD:
Title = Am
                                         ! Compound title
⟨SECTION=CTRL⟩
                                         ! CONTROL PARAMETERS:
                                         ! set: Bare / Screened / Rspace
Lmto = Bare
                                         ! set: FTB/ ASA / PLW
FulPot=ASA
⟨SECTION=EXCH⟩
                                         ! EXCHANGE-CORRELATION:
LDA = Vosko
                                         ! set: none/Barth/Gunn/etc.
GGA = none
                                         ! set: none/91/96
⟨SECTION=ITER⟩
                                         ! ITERATIVE PROCEDURES:
                                         ! # of iterations in SCF loop
Niter1=200
                                         ! Broyden mixing for low l.le.lbroy
Lbroy = -1
⟨SECTION=MAIN⟩
                                         ! MAIN ATOMIC DATA:
Natom = 1
                                         ! # of atoms in the unit cell
Nsort = 1
                                         ! # of sorts in the unit cell
Nspin = 2
                                         ! # of spins
Par0 = 8.72023
                                         ! lattice parameter in a.u.
Is(:) = 1
                                         ! atom-to-sort pointer array
⟨SECTION=SORT⟩
                                         ! SORT DATA:
Name = Am
                                         ! atom label
Znuc = 95.0000
                                         ! nuclear charge
⟨SECTION=FFTS⟩
                                         ! FFT GRIDS:
Ndiv(:)=888
                                         ! Tetrahedron mesh
```

Table 5.2: Input file am.ini

We start by calculating the Americium band structure using the non spin-polarized LDA method. As we expect, this method predicts the 5f bands to lie at the Fermi level. Once we include the effects of U, we see the formation of Hubbard bands separated by an energy U. The 5f-bands and the density of states are plotted in Figs. 5.4 and 5.5 respectively for various values of U. In Americium, spin-orbit effects are significant, which lead to a non-magnetic ground state with total J=0. When we include the effects of spin-orbit coupling in our LDA calculation, the bands for U=0eV that lie near the Fermi level are split by an energy equal to the spin-orbit coupling. When we increase the interaction U, the localized 5f-band moves further away from the Fermi level, and the energy separation between the filled and the empty bands increases by

U. The bands are seen in Fig. 5.6 and the density of states corresponding to the above bands are seen in Figs. 5.7. In all further calculations, we include the effects of spin-orbit coupling.

```
⟨FILE=HUBFILE,INPUT=MODERN,TRACE=TRUE⟩
***************
⟨SECTION=CTRL⟩
                                                        ! CONTROL PARAMETERS:
Scheme=LDA+U1.1
                                                        ! LDA+U1.# / LDA+C / LDA+G1.7
Yharm =spherical
                                                        ! Cubic/Spherical harmonics (output)
Iharm =spherical
                                                        ! Cubic/Spherical harmonics (input)
Rorbs = Both
                                                        ! One/Both orbits to read
Rspin = Both
                                                        ! One/Both spins to read
Format=complex
                                                        ! Real/Complex input/output
                                                        ! DMFT SETTINGS:
⟨SECTION=DMFT⟩
Nmsb = 1
                                                        ! # of Matsubara frequencies
Ndit = 20
                                                        ! \# of DMFT iterations
Efermi = 0.6632451
                                                        ! Fermi energy (Ry)
EpsDMF = 0.1000000E-04
                                                        ! Accuracy
                                                        ! CORRELATED STATES:
⟨SECTION=CORR⟩
Ncrl = 1
                                                        ! # of correlated states
Cstate = Am@1::5f
                                                        ! Correlated state pointer
OutSys = local
                                                        ! global/local coordinate system
OutAxis = -1,1,0
                                                        ! rotational axis
OutAngle= 0*pi
                                                        ! rotational angle
OutInv = no
                                                        ! apply inversion after rotation
InpSys = local
                                                        ! global/local coordinate system
InpAxis = -1,1,0
                                                        ! rotational axis
InpAngle = 0*pi
                                                        ! rotational angle
InpInv = no
                                                        ! apply inversion after rotation
F0 = 0.1470588
                                                        ! Slater integrals
F2 = 0.000000
                                                        ! Slater integrals
F4 = 0.000000
                                                        ! Slater integrals
F6 = 0.000000
                                                        ! Slater integrals
                                                        ! PARTIAL OCCUPANCIES:
⟨SECTION=DHUB⟩
```

Table 5.3: Input file am.hub

The occupancy matrices and the LDA+U potential are written in $\langle SECTION = DHUB \rangle$ in the HUB file.

In Fig. 5.8 we plot the position of the center of the 5f-level (w.r.t the Fermi level)

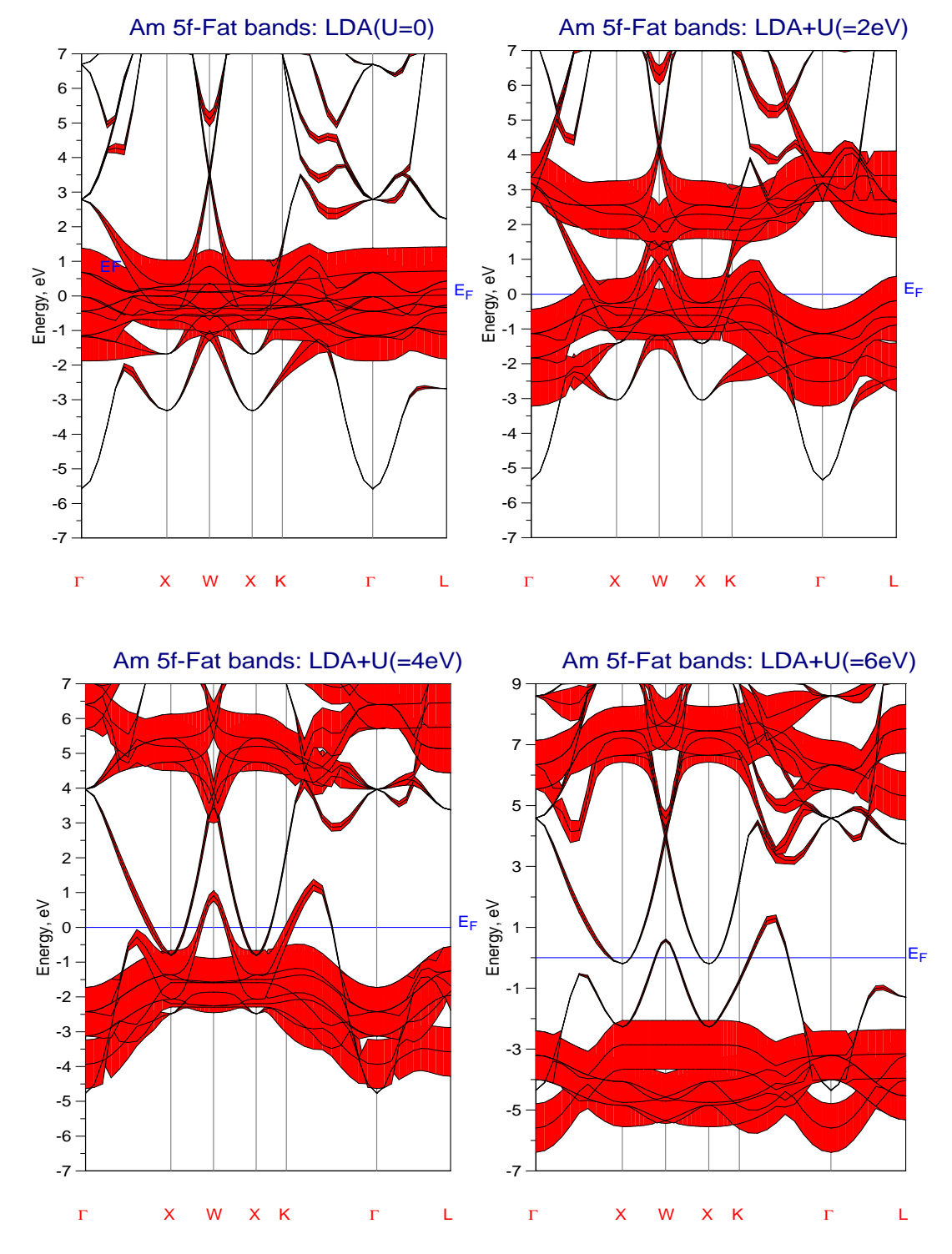


Figure 5.4: Energy bands of Am in LDA+U, no spin-orbit coupling. The colored regions are the fat bands of Am:5f

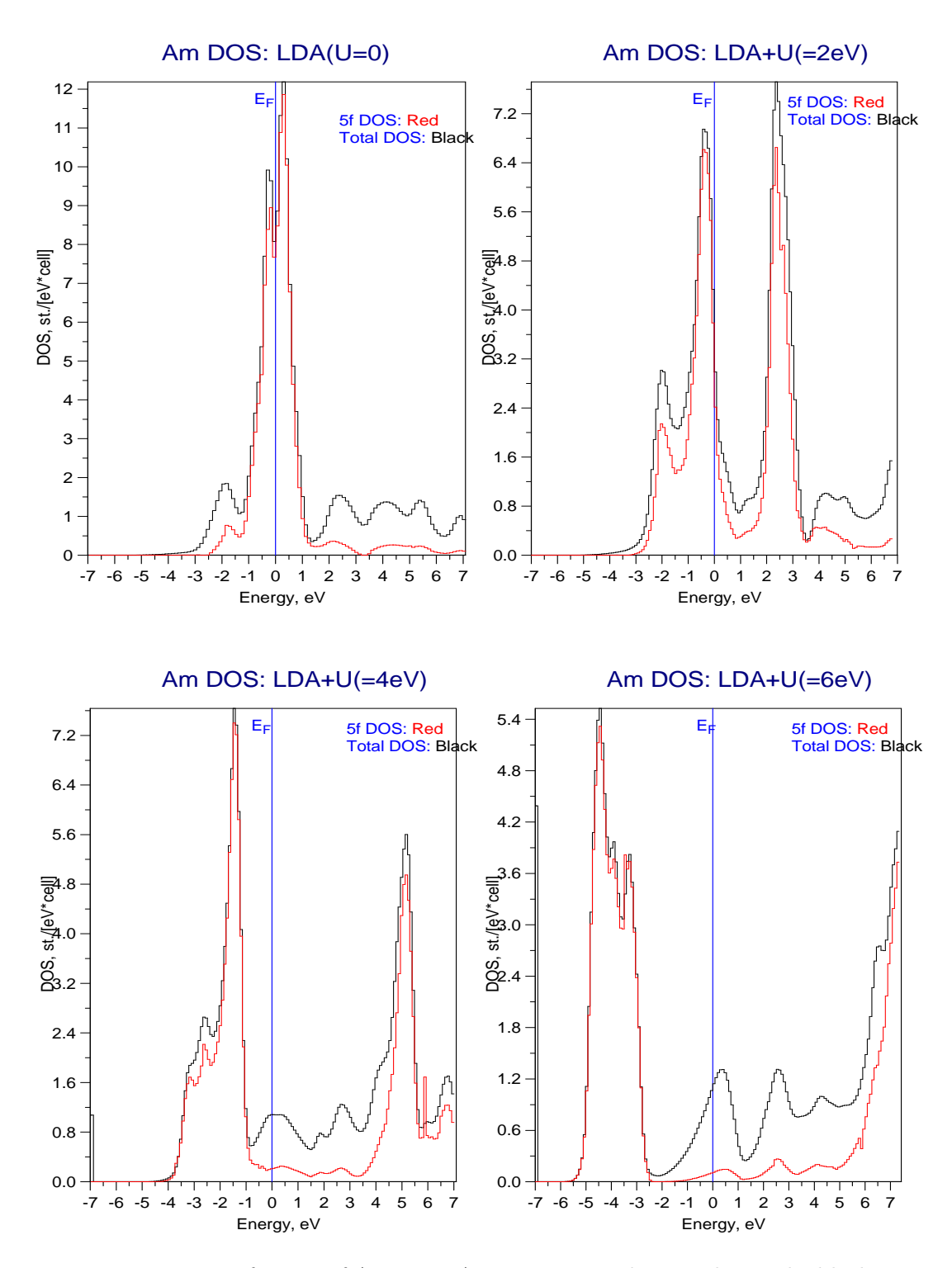


Figure 5.5: Density of states of Am in LDA+U, no spin-orbit coupling. The black curve is the total DOS and the red curve is the partial 5f-DOS

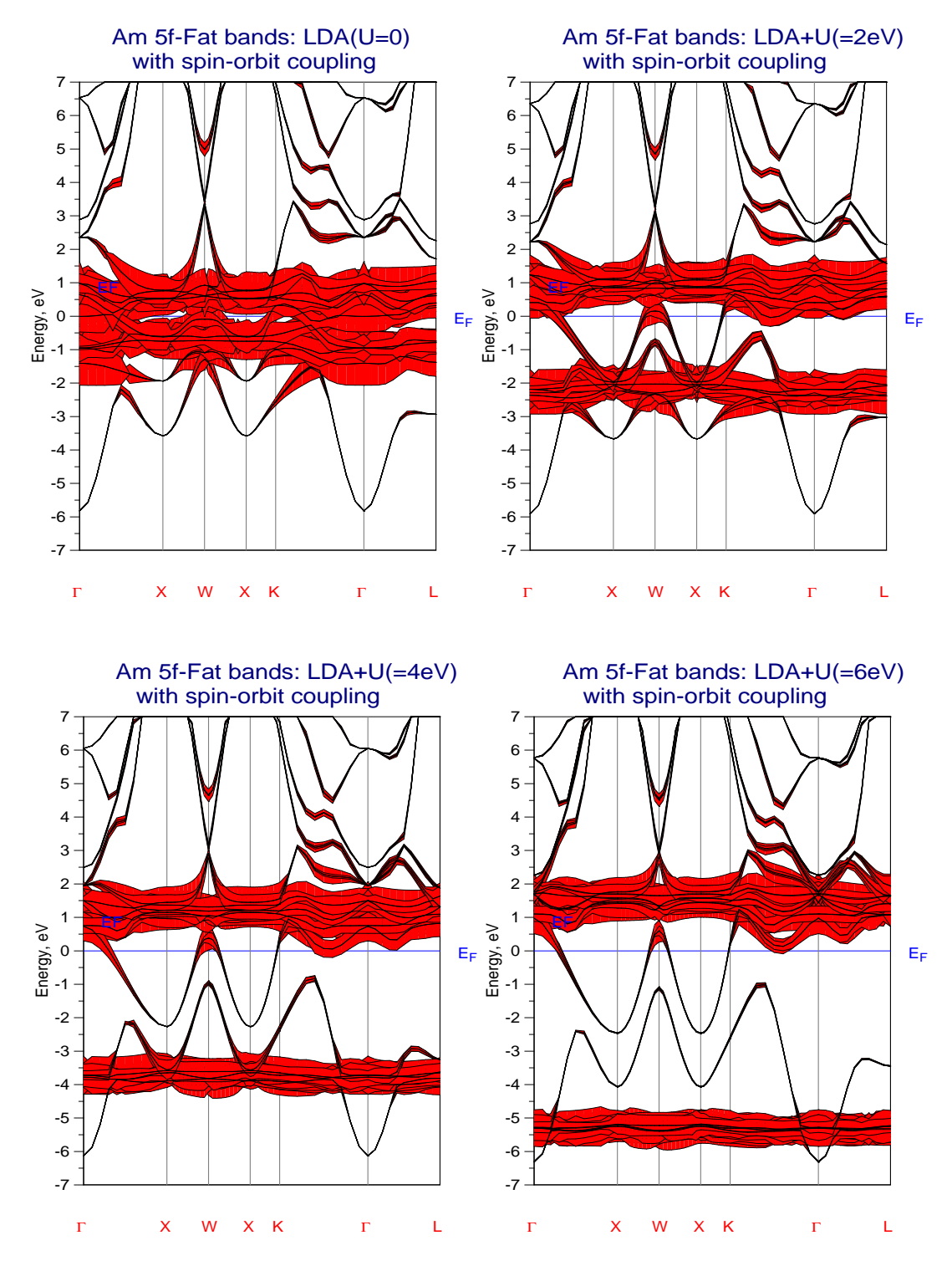


Figure 5.6: Energy bands of Am in LDA+U, with spin-orbit coupling. The colored regions are the fat bands of Am:5f. Note the initial separation (for U=0) between the filled and empty states, which is due to spin-orbit coupling

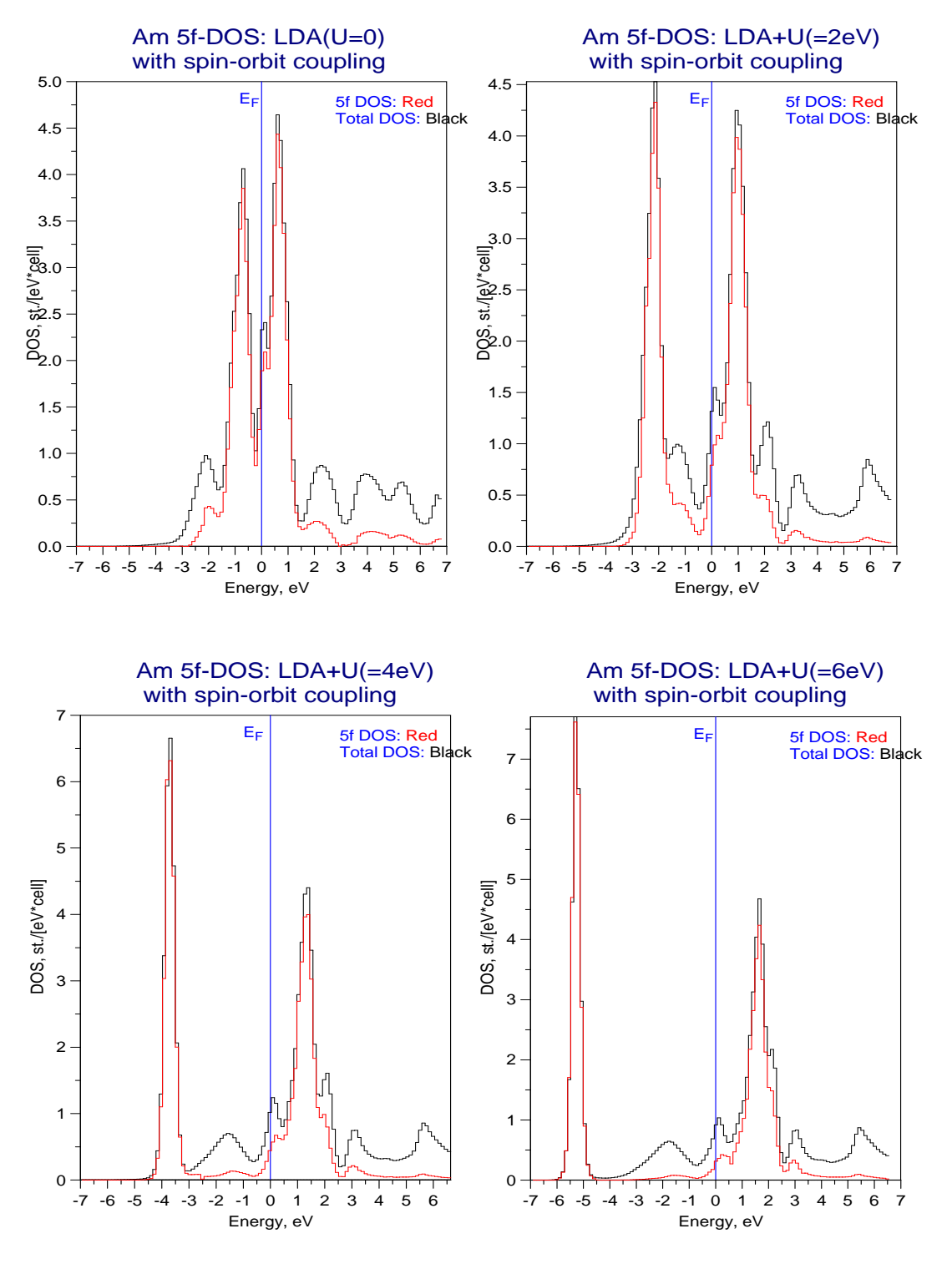


Figure 5.7: Density of states in LDA+U, no spin-orbit coupling. Note the initial separation (for U=0) between the filled and empty states, which is due to spin-orbit coupling. The black curve is the total DOS and the red curve is the partial 5f-DOS

Am: FCC structure, ASA O (Na u) -2 -8 0 2 4 6 8

Figure 5.8: Position of center of the Am 5f-band as a function of the interaction strength

as a function of the interaction U, as obtained from our LDA+U calculations. The 5f-band moves away from the Fermi level as U is increased, and the center of the occupied 5f-band linearly decreases. Experimentally, according to photoemission data (Fig. 5.2, left) obtained by Naegele et. al [60], the conduction band spectrum of Americium shows a peak at 2.8eV below the Fermi energy which corresponds to the localized 5f-band. From our calculations of the spectra as a function of U, (Fig. 5.8) we see that at U = 3eV the 5f level of Americium is centered around 2.8eV below E_{Fermi} .

In the LDA calculation, the filled and the empty states are separated by an energy gap of the order of spin-orbit coupling. As we increase the interaction U, the gap increases linearly with U. When we add correlations, the gap between the occupied and unoccupied states is the LDA-energy gap plus an energy equal to U. In Fig. 5.9 we see the gap between the spin-up and the spin-down electrons of Americium plotted as a function of U.

The LDA+U calculation however fails to predict the correct occupancy and correct magnetic moment of Americium. The LDA calculation predicts the occupancy of the Am 5f-band to be 6.3. As we increase U, the cost of putting two electrons on the same

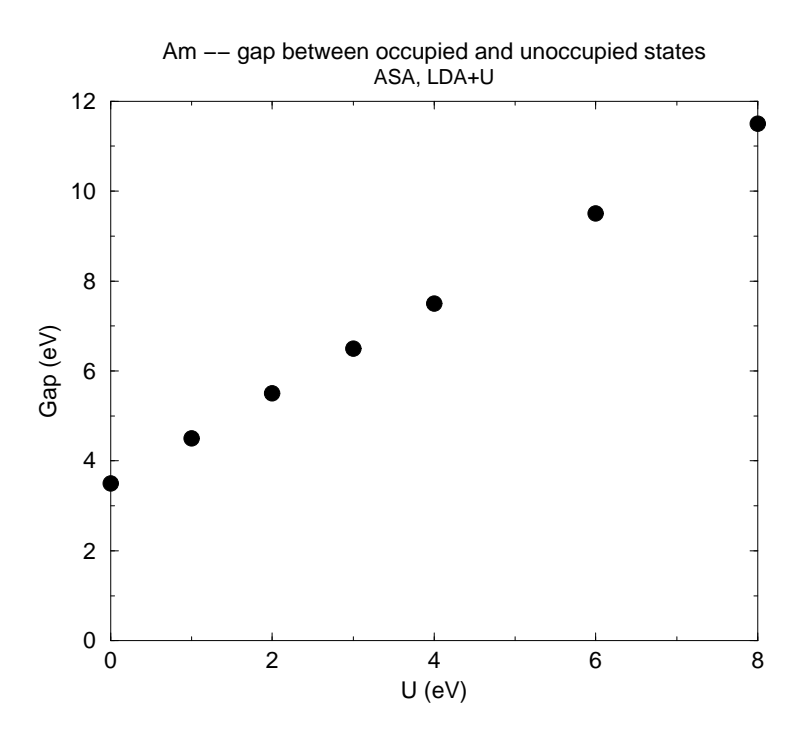


Figure 5.9: Gap between spin-up and spin-dn electrons as a function of the interaction

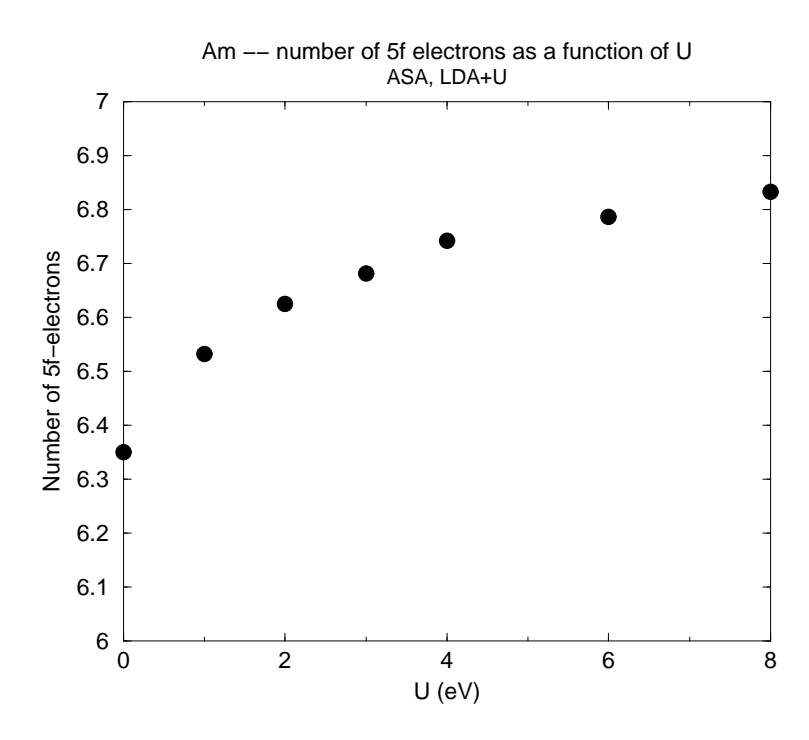


Figure 5.10: Occupancy of Am 5f-band as a function of the interaction strength U

site goes up, and the occupancy of the 5f-band increases. In the LDA+U calculation with $U=4\mathrm{eV}$, it is close to 6.8. Fig. 5.10 shows the occupancy of the Americium 5f-band as a function of U. However, the occupancy of the 5f states of Americium is known to be 6 (Ref. [67]). In section 5.3 we will show that the LDA+DMFT calculations predict the correct occupancy of 6, and a zero magnetic moment for Americium.

5.2.1 Effect of the double counting term

In the fat bands and density of states (Figs. 5.6 and 5.7), we kept the interaction \bar{U} in the double counting term in the same as that used in the model, U. Decreasing the value of \bar{U} however shifts the 5f peak away from the Fermi level. Fig. 5.11 shows the position of the localized 5f-level as a function of the double counting interaction U_{dc} , or \bar{U} at U = 3eV. In the LDA+DMFT calculation in section 5.3 we will use U_{dc} as a parameter to fix the 5f peak at its experimental value.

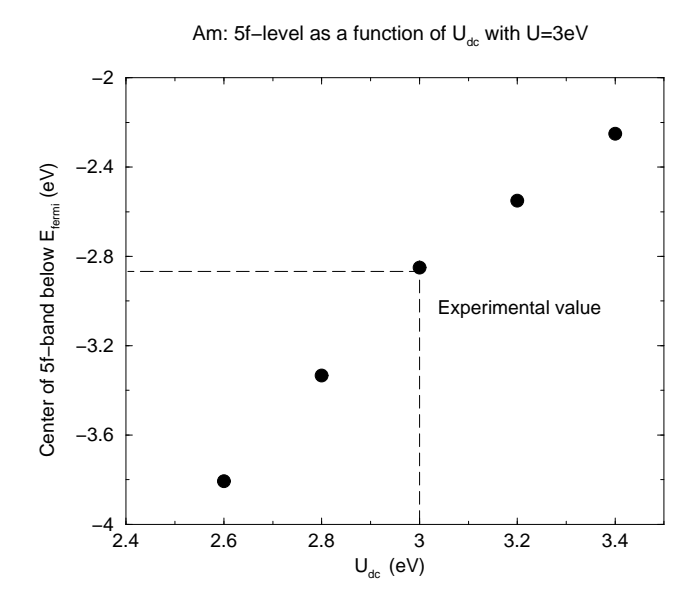


Figure 5.11: Effect of U_{dc} : Position of the center of the f-band as a function of the U_{dc} , with U kept at 4eV.

In the next section, we turn to the details of the calculation of equilibrium volume in LDA+U, which gives excellent agreement with experiment.

5.2.2 Volume behavior

We calculate the equilibrium atomic volume of Americium by plotting the total energy from our LDA+U calculations as a function of relative volume V/V_0 , for various values of U (Fig. 5.12). From the minimum in these plots, the equilibrium volume for Americium is calculated. In each of the methods, the fcc structure is used as the crystal structure for Am. In Fig. 5.12, we use the experimental equilibrium atomic volume of $29.3 \text{ Å}A^3$ [70] for V_0 . Our LDA+U calculation predicts the correct equilibrium volume at U = 4.5 eV.

We also performed a calculation by considering the 5f electrons as core electrons. In order to do this we change one of the input files lmt.am that contains all the atomic data. We remove the 5f-electrons from the basis and set them as the core electrons. We set lmax=2, and consider 8 valence electrons only from the 6p and 7s subshells. The 6s electrons are considered as semi-core electrons. The input file lmt.am that we enter the above data in is shown in Fig. 5.13. However, in this case, the self-consistent equations fail to give a a bound state solution with 5f electrons in the core. The band structure and the density of states for Americium in this scheme are shown in Figs. 5.14 and 5.15 respectively. According to similar calculations by Soderlind, et.al [65] the volume obtained by treating the 5f-electrons as core electrons is only $26.6 \text{\AA}A^3$, which is about 10% less than the experimental volume.

Table-5.4 summarizes the results we obtain:

Method	Equlibrium volume $(in \mathring{A}^3)$
LDA	20.3682
LDA+U, U=1eV	23.6460
LDA+U, U=2eV	26.1092
LDA+U, U=3eV	27.5871
LDA+U, U=4eV	28.7118
LDA+U, $U=4.5eV$	29.2
LDA w/ 5f in core	27.97
Experiment	29.3

Table 5.4: Equilibrium volumes for Am in \mathring{A}^3

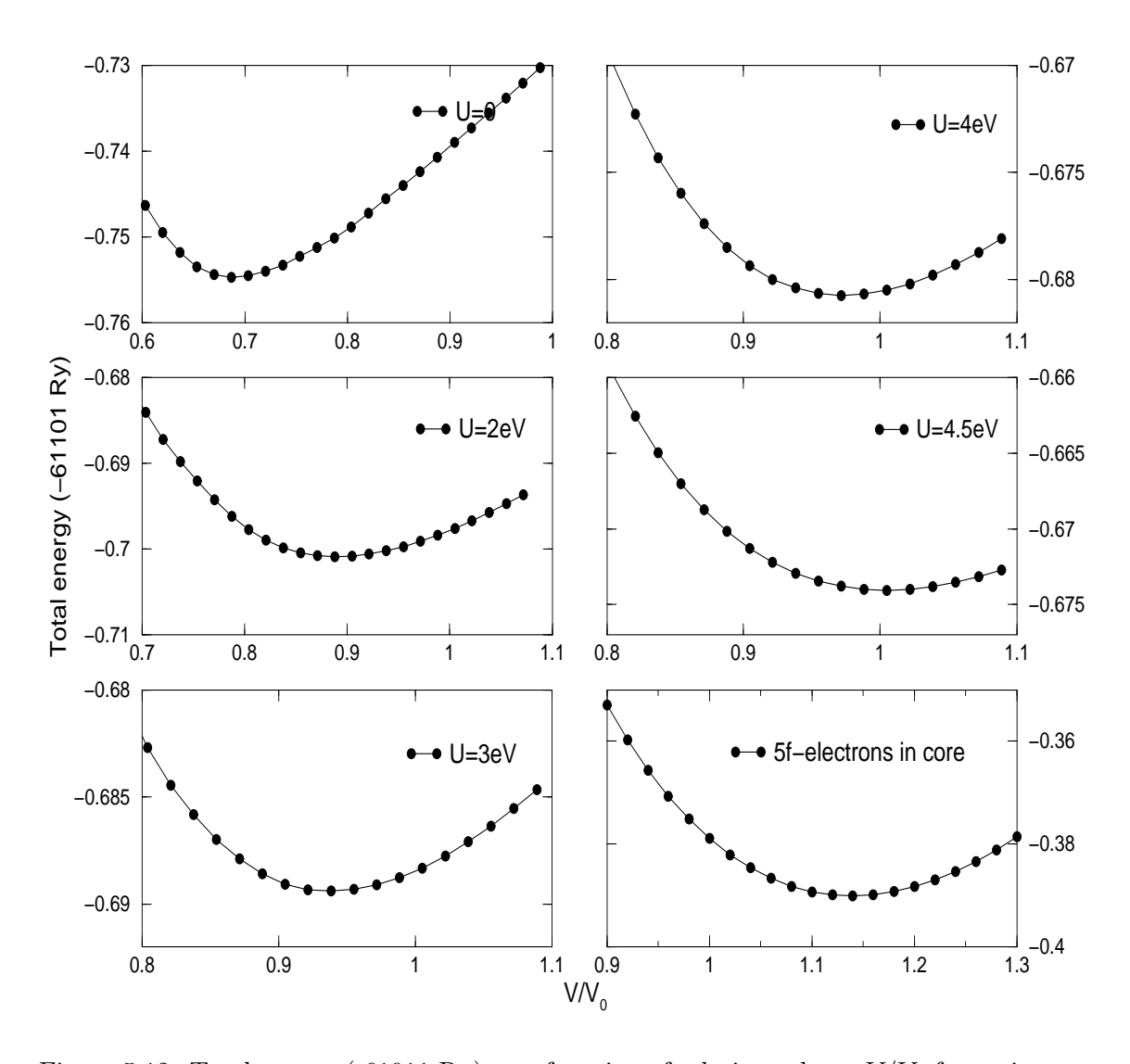


Figure 5.12: Total energy (-61011 Ry) as a function of relative volume V/V_0 for various values of interaction U(in eV).

* DI DMDMD A		
* ELEMENT: Am,	Configuration 6s2/6p6/7s2/6d0/5f7	
$\langle SECTION = SORT \rangle$ name	=Am	! element name
znuc	=95	! nuclear charge
zval	=8	! # of valence electrons
zsem	=0 $=2$! # of semicore electrons
amas	-2 =243	! atomic mass
lmaxb	=243 =2	! Lmax for LMTO basis
(subsection=lmto)	-2	: Elliax for EWTO basis
!	s p d f g	! States
Mqn(:)	76655	! Main quantum numbers
Bas(:)	1 1 1 0 0	! LMTO basis set
Mnu(:)	3 3 3 0 0	! Choice of Enu
Enu(:)	+0.5, +0.5, +0.5, +0.5, +0.5	! Initial Enu
Dnu(:)	-1.0,-2.0,-3.0,-4.0,-5.0	! Initial Dnu
(subsection=semi)	-1.0,-2.0,-3.0,-4.0,-0.0	: Illitiai Diid
nsem	=1	! # semicore states
lsem	=6s	! n,l
(subsection=conf)	-05	. 11,1
!Orbital	n l j #el.	Levels(Ry)
1s1/2	$ \begin{array}{cccccccccccccccccccccccccccccccccccc$	-7850.4727
$\frac{2s1}{2}$	$ \begin{array}{cccccccccccccccccccccccccccccccccccc$	-1447.8048
291/2 $2p1/2$	$\begin{array}{cccccccccccccccccccccccccccccccccccc$	-1394.6574
$\frac{2p1}{2}$ $\frac{2p3}{2}$	$\begin{array}{cccccccccccccccccccccccccccccccccccc$	-1155.9321
3s1/2	$\begin{array}{cccccccccccccccccccccccccccccccccccc$	-360.94632
3p1/2	$\begin{array}{cccccccccccccccccccccccccccccccccccc$	-336.82037
3p3/2	$\begin{array}{cccccccccccccccccccccccccccccccccccc$	-282.31668
3d3/2	$\begin{array}{cccccccccccccccccccccccccccccccccccc$	-243.61142
3d5/2	$\begin{array}{cccccccccccccccccccccccccccccccccccc$	-232.36490
4s1/2	$ \begin{array}{cccccccccccccccccccccccccccccccccccc$	-89.627118
4p1/2	$\begin{array}{cccccccccccccccccccccccccccccccccccc$	-78.886649
4p3/2	$\begin{array}{cccccccccccccccccccccccccccccccccccc$	-64.904609
4d3/2	$\begin{array}{cccccccccccccccccccccccccccccccccccc$	-47.651517
4d5/2	$\begin{array}{cccccccccccccccccccccccccccccccccccc$	-45.061490
4f5/2	$\begin{array}{cccccccccccccccccccccccccccccccccccc$	-22.427601
4f7/2	$\begin{array}{cccccccccccccccccccccccccccccccccccc$	-21.774721
5s1/2	$ \begin{array}{cccccccccccccccccccccccccccccccccccc$	-19.277471
5p1/2	5 1 1/2 2	-15.228066
5p3/2	5 1 3/2 4	-12.070072
5d3/2	5 2 3/2 4	-6.1802559
5d5/2	$\begin{array}{cccccccccccccccccccccccccccccccccccc$	-5.7243980
5f5/2	$5 \ 3 \ 5/2 \ 6$	-0.1227601
5f7/2	$5 \ 3 \ 7/2 \ 1$	-0.1227601
6s1/2	$\begin{array}{cccccccccccccccccccccccccccccccccccc$	-3.0330305
6p1/2	$\begin{array}{cccccccccccccccccccccccccccccccccccc$	-1.9080418
6p3/2	$\begin{array}{cccccccccccccccccccccccccccccccccccc$	-1.4078676
7s1/2	$\begin{array}{cccccccccccccccccccccccccccccccccccc$	-0.3556810
101/2	1 0 1/2 2	5.5555515

Figure 5.13: Input file lmt.am for treating f-electrons as core.

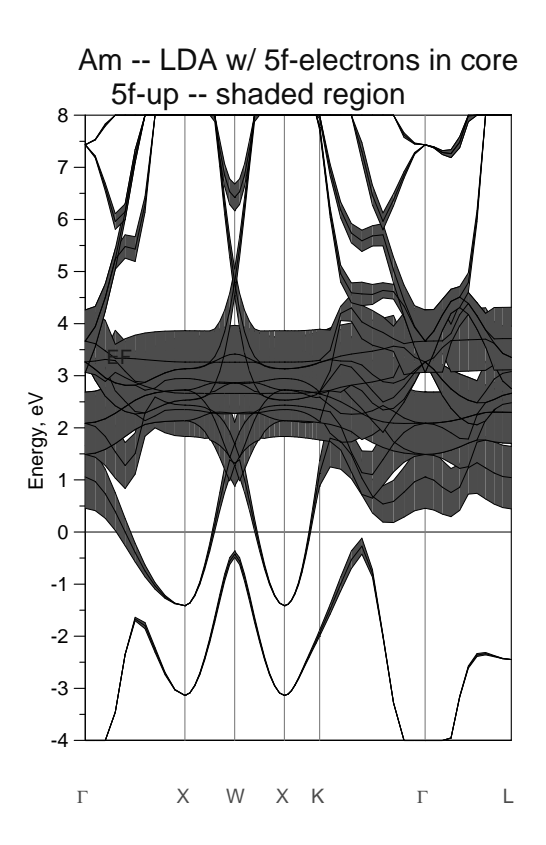


Figure 5.14: Energy bands of Am treating 5f electrons as core

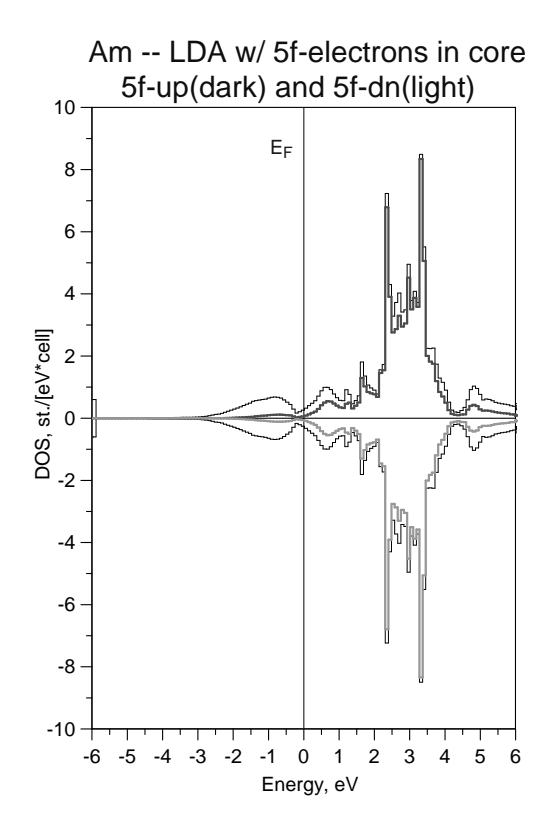


Figure 5.15: DOS of Am treating 5f electrons as core

5.3 LDA+DMFT method

The equilibrium volume of Americium predicted by LDA+U is in good agreement with experiment. However it fails to predict the correct zero magnetic moment. We now apply the LDA+DMFT method described in chapter 3 to calculate the band structure of americium.

To solve the impurity model, we use a method that is based on the Hubbard-I approximation. We do a full self-consistent calculation, where the charge density is recomputed after the DMFT loop and is fed back to the routine that calculates the potential and then the new LDA Hamiltonian.

5.3.1 Hubbard-1 method

The starting point of the Hubbard-I approximation is the atomic limit. We first find the Green's function for the atomic Hamiltonian using the equation of motion method for the Hubbard operators. We then express the impurity Green's functions in terms of the atomic Green's function and the hybridization $\Delta(i\omega)$.

We start with a impurity model that has the form $H = H_{atom} + H_{band} + H_{hyb}$.

$$H_{atom} = \sum_{\substack{ll'=5/2,7/2\\m=1...(2l+1)\\m'=1...(2l'+1)}} \epsilon_{ll'mm'}^{f} f_{lm}^{\dagger} f_{l'm'} + U \sum_{\substack{l,l'=5/2,7/2\\m,m'}} f_{lm}^{\dagger} f_{lm} f_{l'm'}^{\dagger} f_{l'm'}$$

$$H_{band} = \sum_{lk} \epsilon_{lk} c_{lk}^{\dagger} c_{lk}$$

$$H_{hyb} = \sum_{ll'mk} V_{ll'k} (f_{lm}^{\dagger} c_{l'k} + h.c.)$$
(5.1)

Here l, l' label the two bands that are split due to spin-orbit coupling. These two bands have the j-quantum number as 5/2 or 7/2. Notation: The band with l=5/2 and is 6-fold degenerate and that with l=7/2 and is 8-fold degenerate. Thus m, m' label the degeneracy and run from 1 to (2j+1). Since the impurity level matrix $\epsilon_{ll'mm'}^f$ has off-diagonal terms as zero, the first term simplifies to $\sum_{lm} \epsilon_l^f f_{lm}^\dagger f_{lm}$. H_{hyb} is due to the hybridization between the conduction electrons and the localized f electrons. The hybridization function can be written as $\Delta_l(i\omega) = \sum_{l'k} V_{l'k}^2/(i\omega - \epsilon_{l'k})$.

In the case of Americium, due to the above degeneracy, we have a $SU(6) \times SU(8)$ symmetry. With this, the impurity Green's function in the Hubbard-1 approximation becomes

$$\left[G_l^{imp}(i\omega)\right]^{-1} = \left[G_l^{at}(i\omega)\right]^{-1} - \Delta_l(i\omega) \tag{5.2}$$

The atomic Green's function G_{at} is given by

$$G_l^{at}(i\omega) = \sum_{n=0}^{14} \sum_{\substack{n_1=0\\n_1<6\\(n-n_1)<8}}^{n} \frac{\left(C_{n_1}^6 C_{n-n_1}^8 \left[e^{-E_{ln}/T} - e^{-E_n/T}\right]\right)/Z}{i\omega + \mu - E_{ln} + E_n}$$
(5.3)

where E_{ln} is the energy of an atom with n total number of electrons, n_1 in level l=1 and $n-n_1$ in level l=2 is given by :

$$E_{ln} = E_n + \epsilon_l^f + Un \tag{5.4}$$

$$E_n = \frac{U(n-1)n}{2} + n_1 \epsilon_1^f + (n-n_1)\epsilon_2^f$$
 (5.5)

The numerator in (5.3) denotes the probability of finding an atom with n total number of electrons, n_1 in level l = 1 and $n - n_1$ in level l = 2. $C_{n_1}^6$ and $C_{n-n_1}^8$ are the combinatorial coefficients. Z is a normalization factor for the probability given by

$$Z = \sum_{n=0}^{14} \sum_{\substack{n_1=0\\n_1 \le 6\\(n-n_1) \le 8}}^{n} C_{n_1}^6 C_{n-n_1}^8 e^{-E_n} / T$$
(5.6)

5.3.2 Tight-binding calculation

We first do a tight-binding calculation for the band structure of americium. We generate the hop file that gives the hopping integrals and positions of the impurity levels. We then run the LMTART program in the tight-binding mode and calculate the bands and density of states.

Experimentally, Americium has zero magnetic moment with 6 electrons in the j = 5/2 state. Thus from the tight-binding calculation, we choose a model with two bands – band 1 corresponding to j = 5/2 and band 2 that has j = 7/2:

$$H_{TB} = t_1 c_1^{\dagger} c_1 + t_2 c_2^{\dagger} c_2 + \epsilon_1 f_1^{\dagger} f_1 + \epsilon_2 f_2^{\dagger} f_2 \tag{5.7}$$

where c_1 and c_2 are the operators for the conduction electrons in bands 1 and 2 respectively, and f_1 and f_2 are the operators for the f-electron. The parameters t_1, t_2, ϵ_1 and ϵ_2 are chosen so that the bands from the tight-binding calculation match the bands from the fully self-consistent LDA calculation. We find that the other hoppings are negligible compared to t_1 and t_2 . Figs. 5.16-5.19 show a comparison between the density of states obtained from the tight-binding calculation and those obtained from the LDA self-consistent calculation.

Figs. 5.20 and 5.21 shows how the tight-binding parameters change as a function of pressure. In the calculation, we reduce the relative volume V/V_0 , thus applying pressure on the system. As the pressure is increased we find that the parameters increase.

We then perform a DMFT calculation on the above model, using the Hubbard-I impurity solver described in Chapter 3. A plot containing the density of states for different values of U obtained from LDA+DMFT on the above model is shown in Fig. 5.22. As U is increased, we see the increase in the gap between the occupied and the unoccupied states.

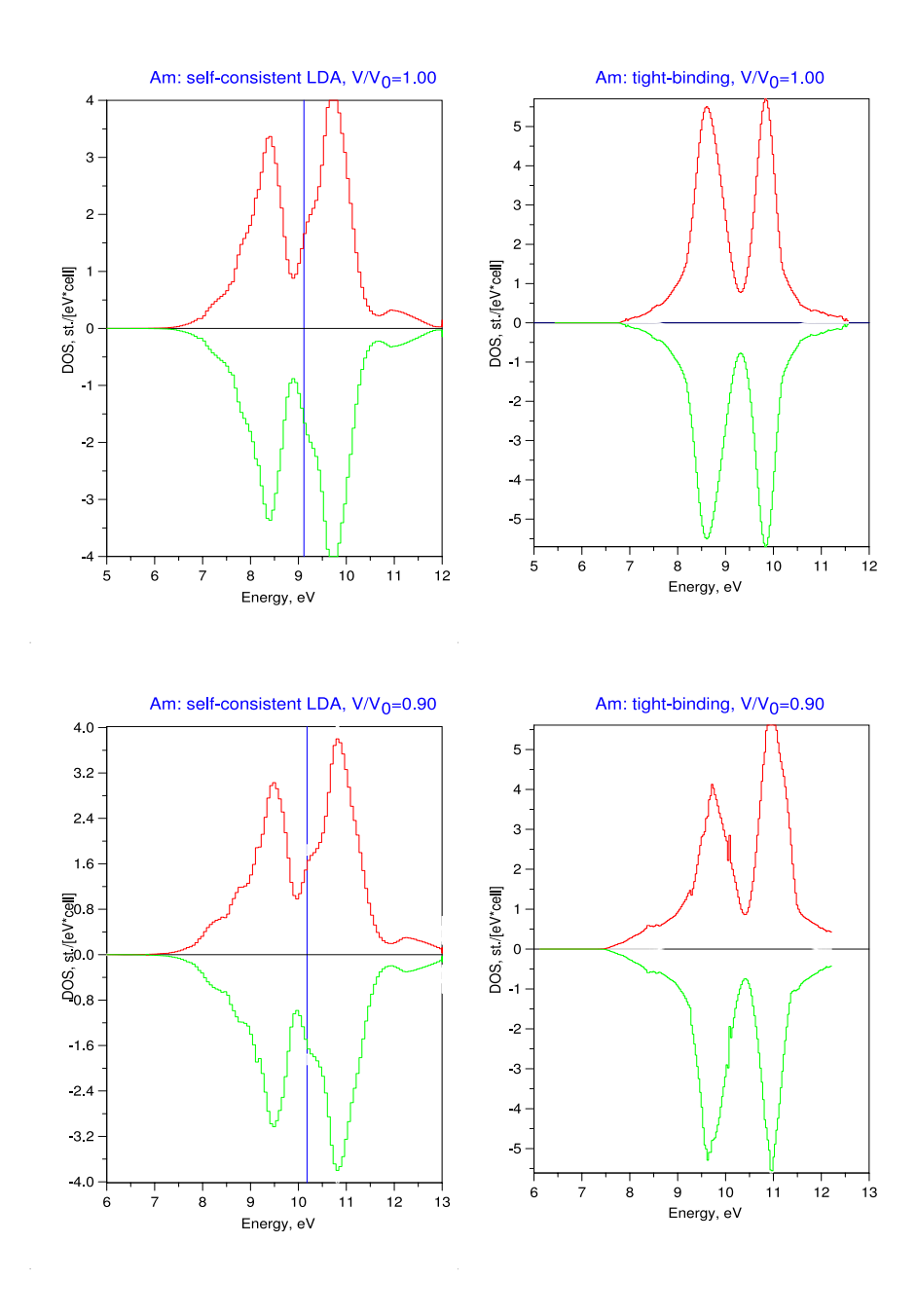


Figure 5.16: Comparison of DOS : LDA and Tight binding methods

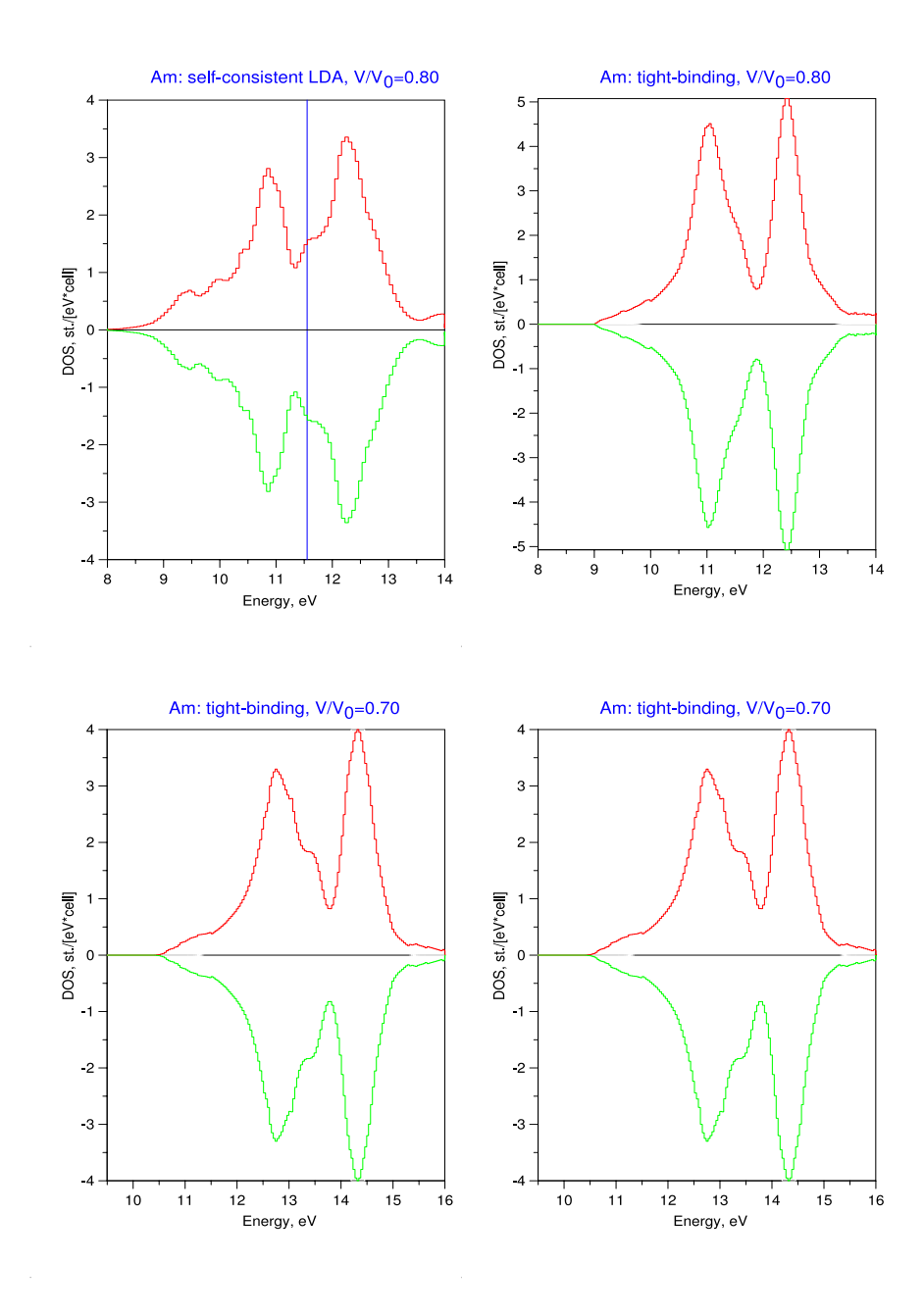


Figure 5.17: Comparison of DOS : LDA and Tight binding methods

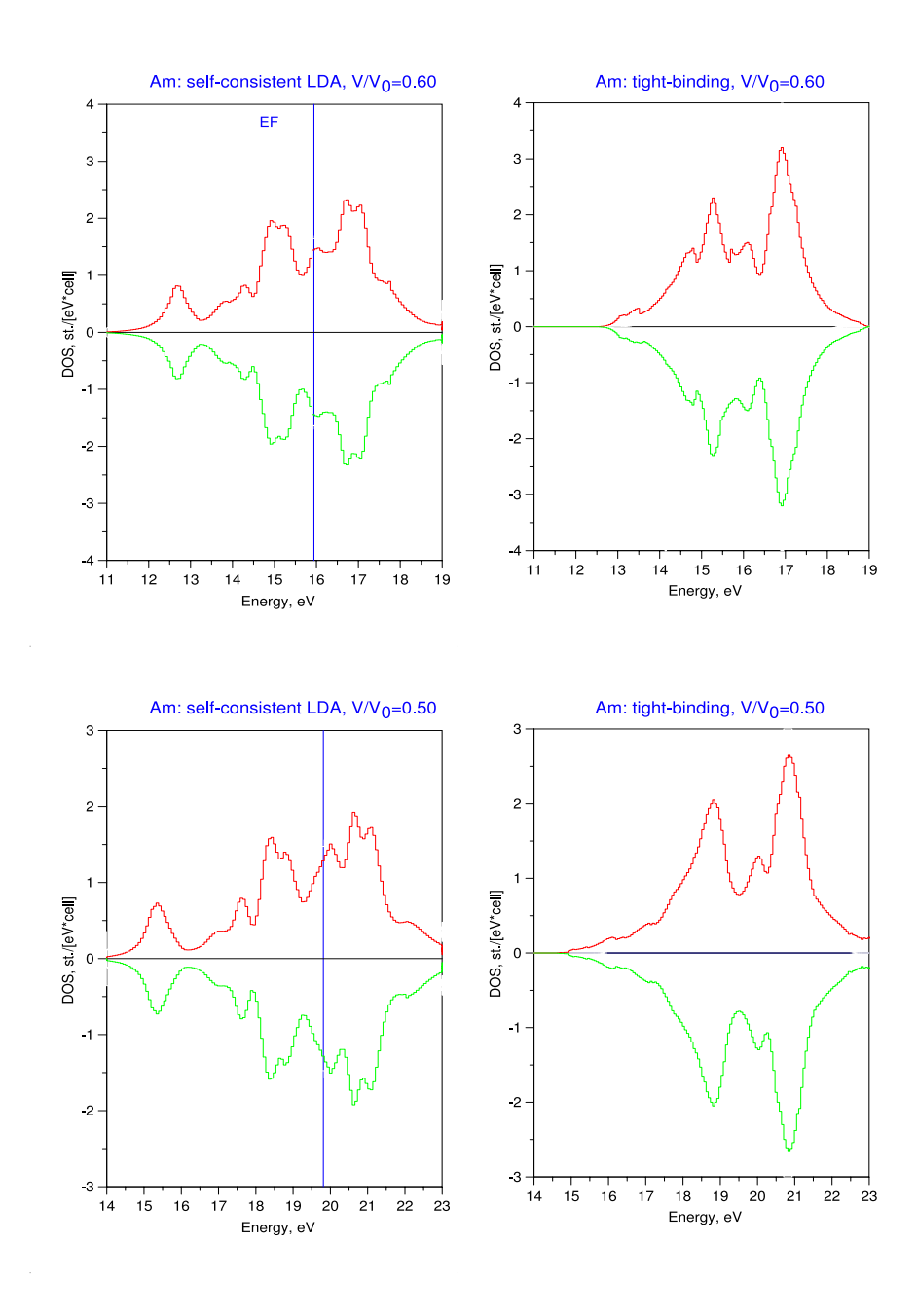
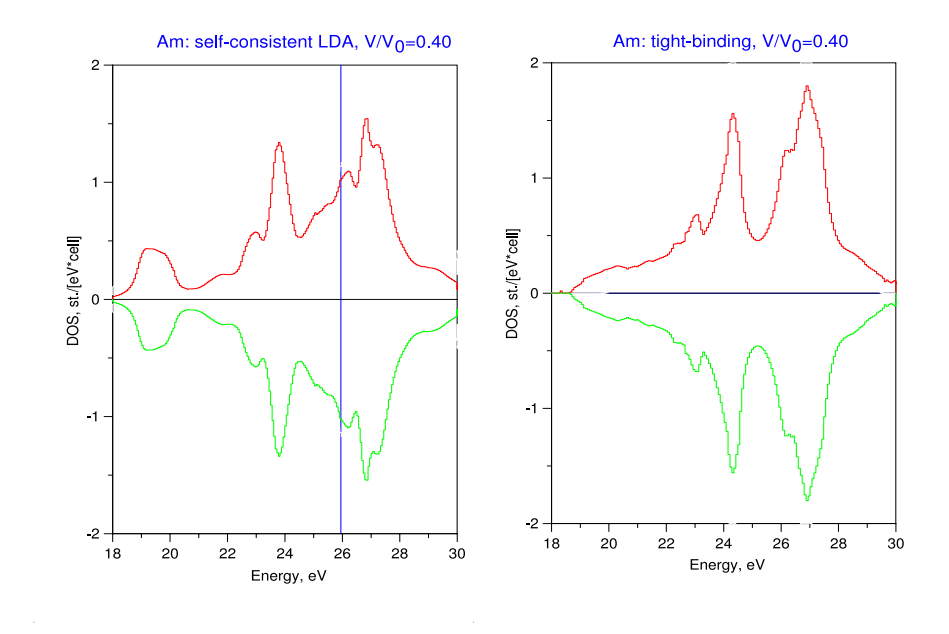


Figure 5.18: Comparison of DOS : LDA and Tight binding methods

Figure 5.19: Comparison of DOS : LDA and Tight binding methods



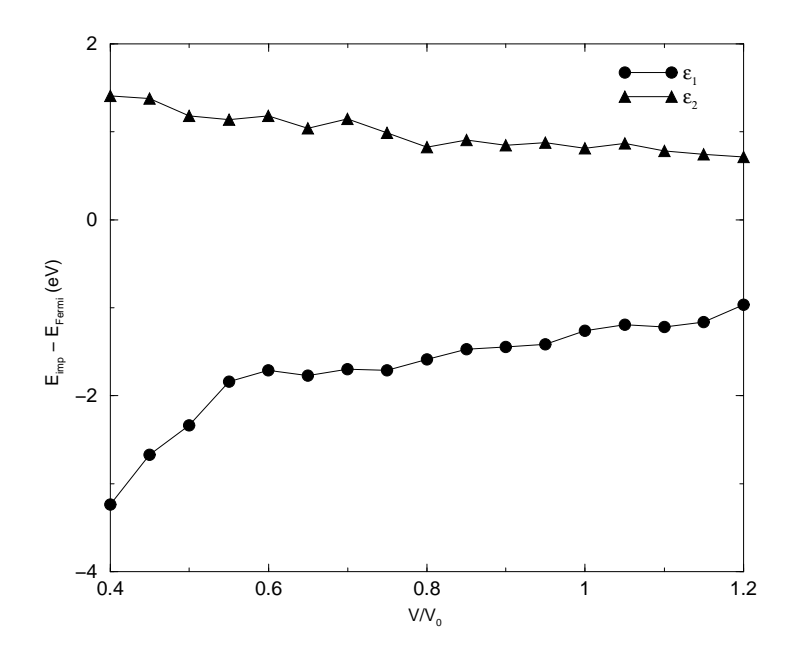


Figure 5.20: Impurity level (w.r.t E_F) as a function of relative volume

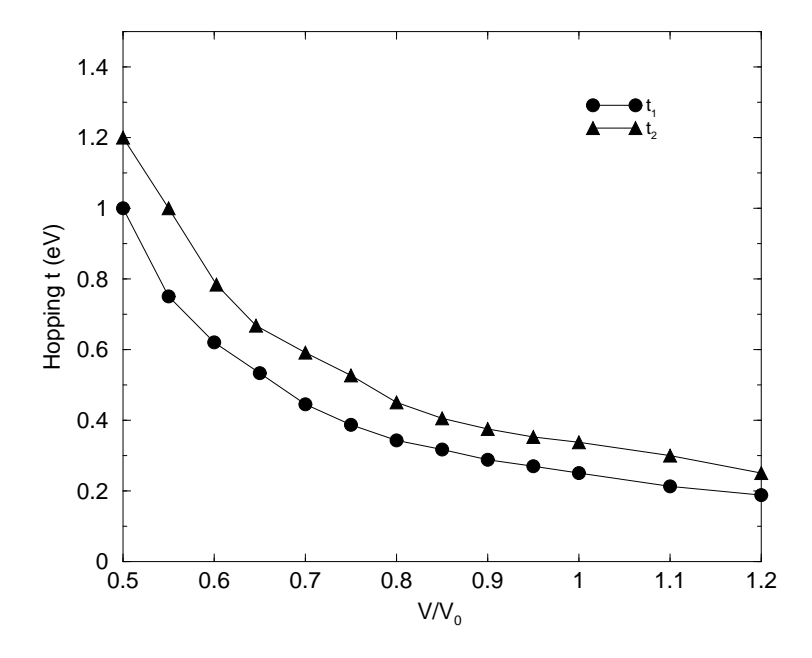


Figure 5.21: Tight binding hoppings as a function of relative volume

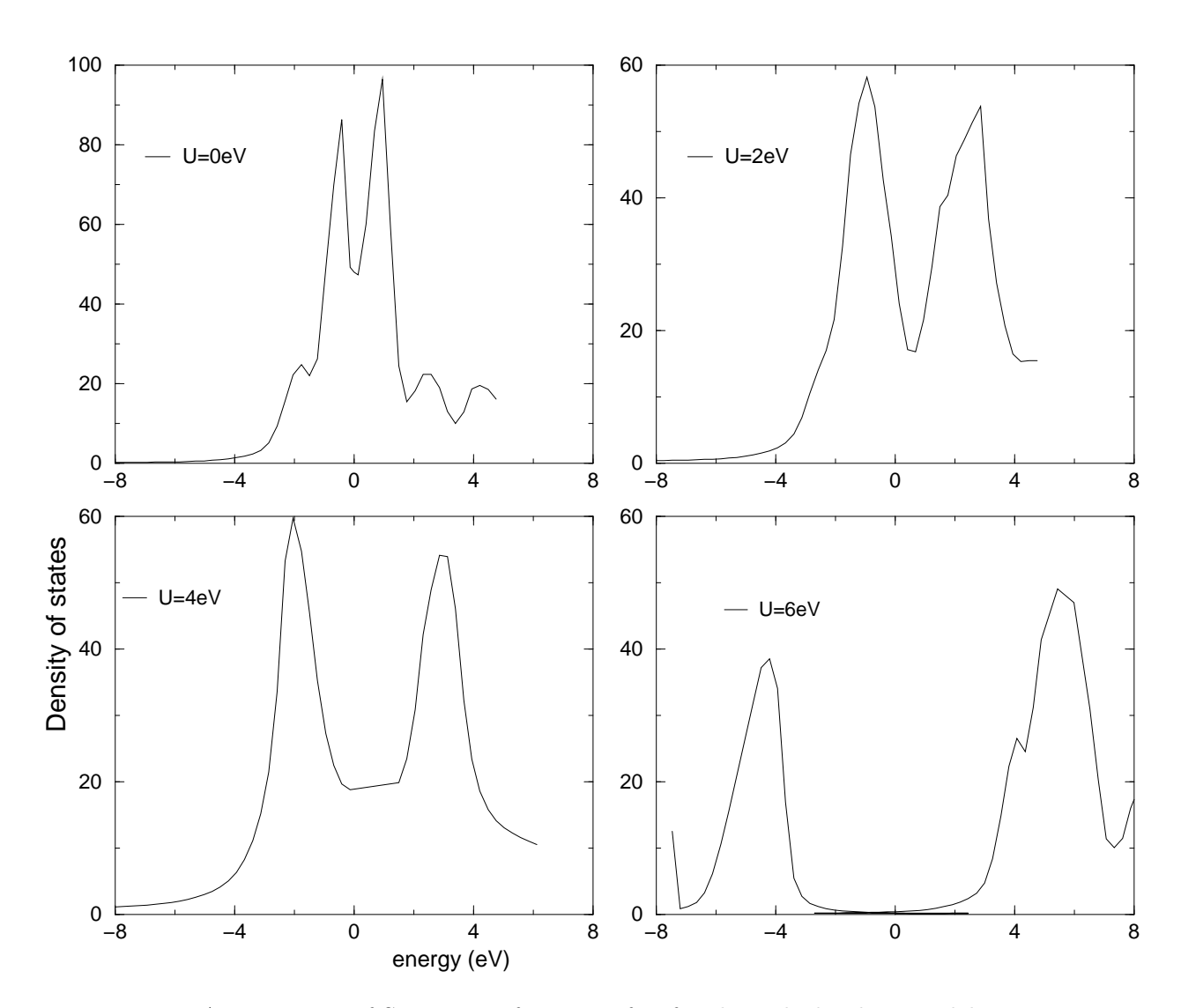


Figure 5.22: Am: Density of States as a function of U for the tight-binding model

5.3.3 LDA+DMFT Results

The above tight-binding model for Americium correctly describes its natural state. We now perform a full self-consistent LDA+DMFT calculation on Am, with the effects of spin-orbit coupling included. We use the Hubbard-I solver explained in section (5.3.1) as the impurity solver.

In Figs. 5.23 we plot the total energy (-61102Ry) as a function of relative volume at U = 4.5eV. The volume V_0 is chosen to be the experimental volume.

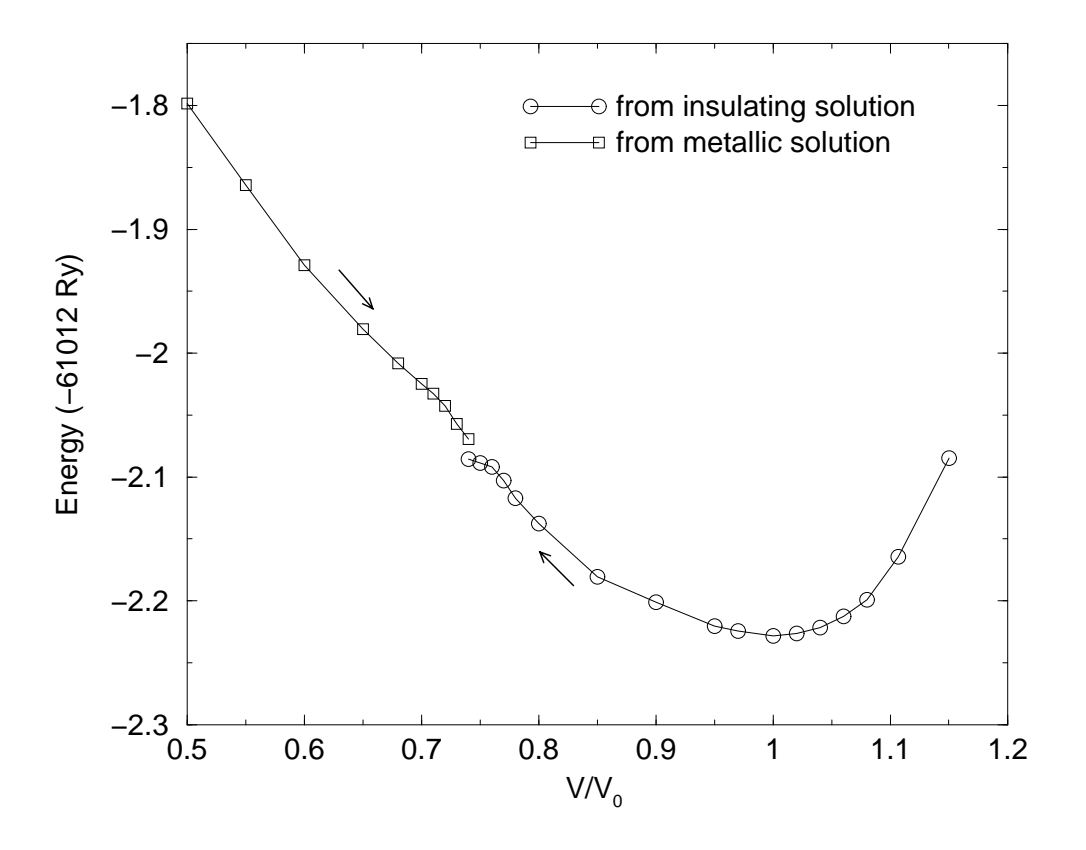


Figure 5.23: Energy vs. relative volume

The equilibrium volume is predicted correctly by the LDA+DMFT method, similar to the equilibrium calculation in the LDA+U method. The curve with circles is obtained from the high volume side, gradually decreasing the volume and using the self-consistent results from the previous run for the next. The curve with squares is obtained starting from the low volume side, and gradually increasing the volume. We find a region near $V/V_0 = 0.7$ where there are two different energies for the same volume. The pressure,

i.e., the derivative of energy w.r.t. volume $\partial E/\partial V$ is plotted as a function of relative volume in Fig. 5.24.

The region of the where there is a discontinuity in the solutions can be thought of as a coexistence region for the metallic-like and the insulating-like phases of the material. This is a strong indication of the a Mott transition where the 5f electrons undergo a change of character from localized to delocalized as we increase the pressure.

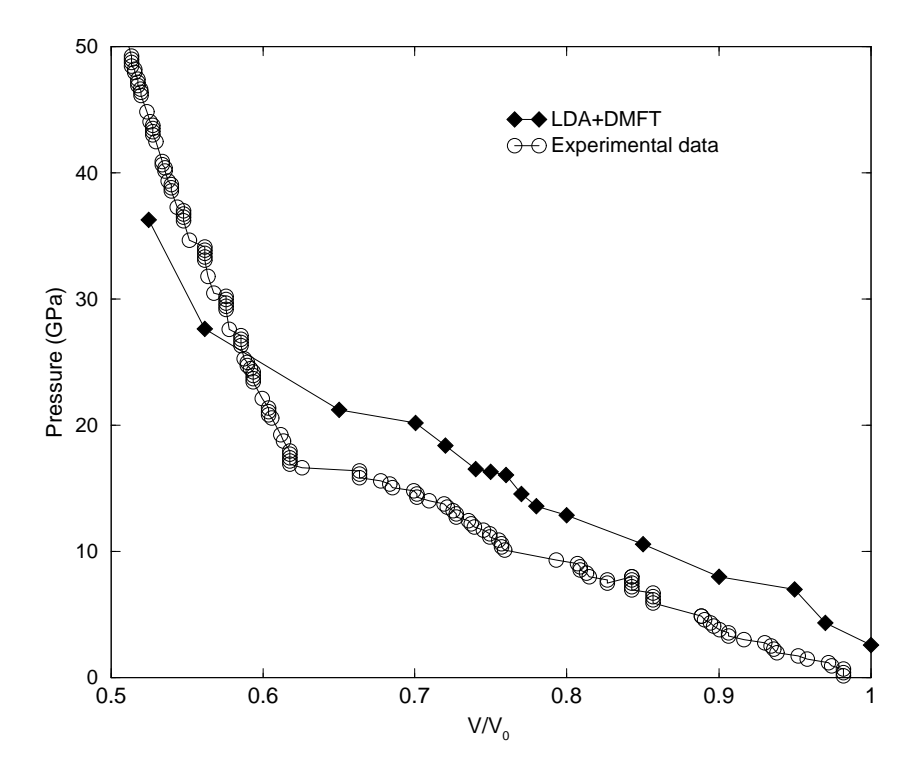


Figure 5.24: Pressure vs. relative volume

We now turn to how the Americium 5f-density of states behave as we apply pressure on the system. The DOS calculated from LDA is shown in Fig. 5.27. As we saw in sections 5.2 and 5.2.2, LDA neither correctly predicts the position of the 5f peak nor the equilibrium volume. However, as we apply pressure we see that the DOS start broadening.

We need to include the effects of U to correctly predict the 5f-peak and the equilibrium volume. At U = 4.5eV, the value of the interaction which gives the correct equilibrium volume, we find that the position of the 5f-peak is at 3.8eV below the Fermi

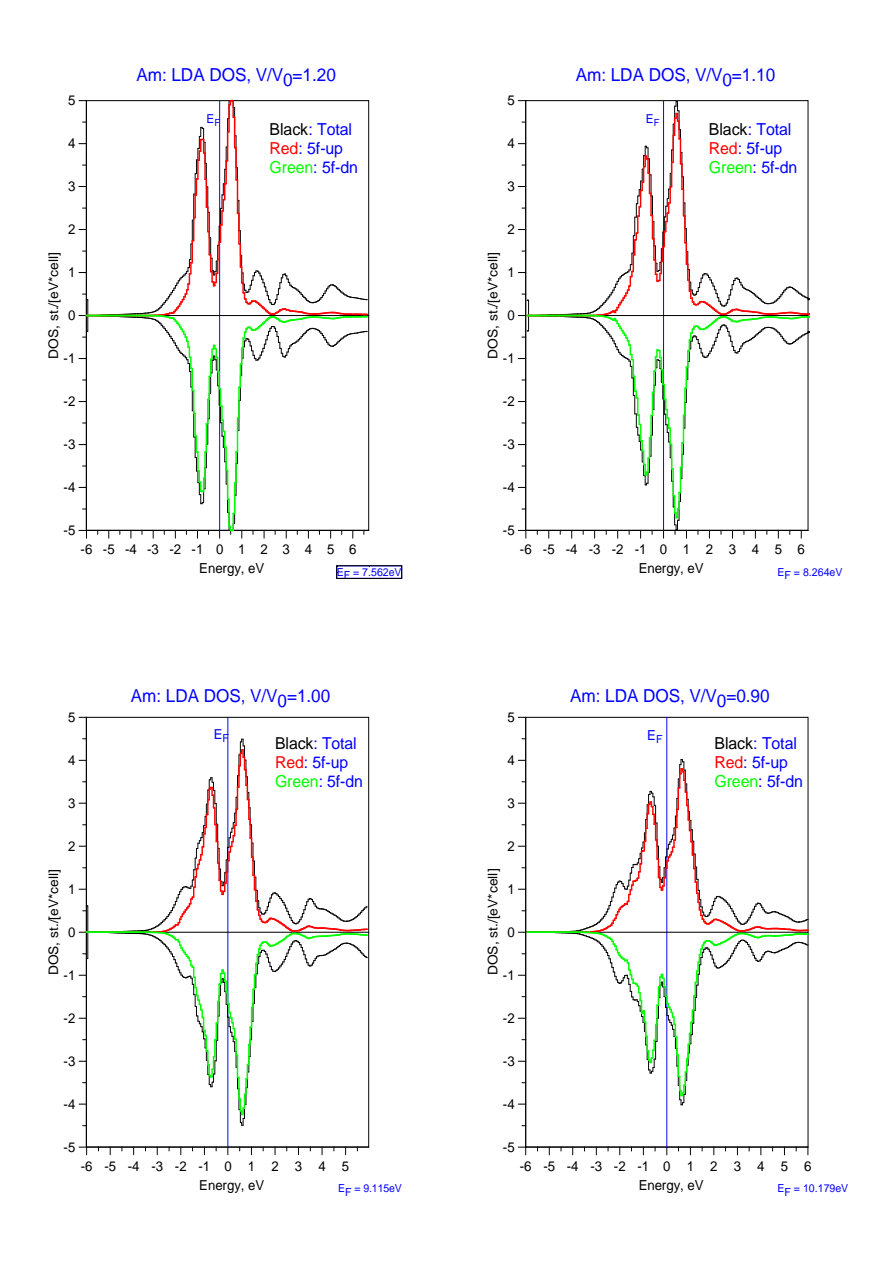


Figure 5.25: Am DOS in LDA

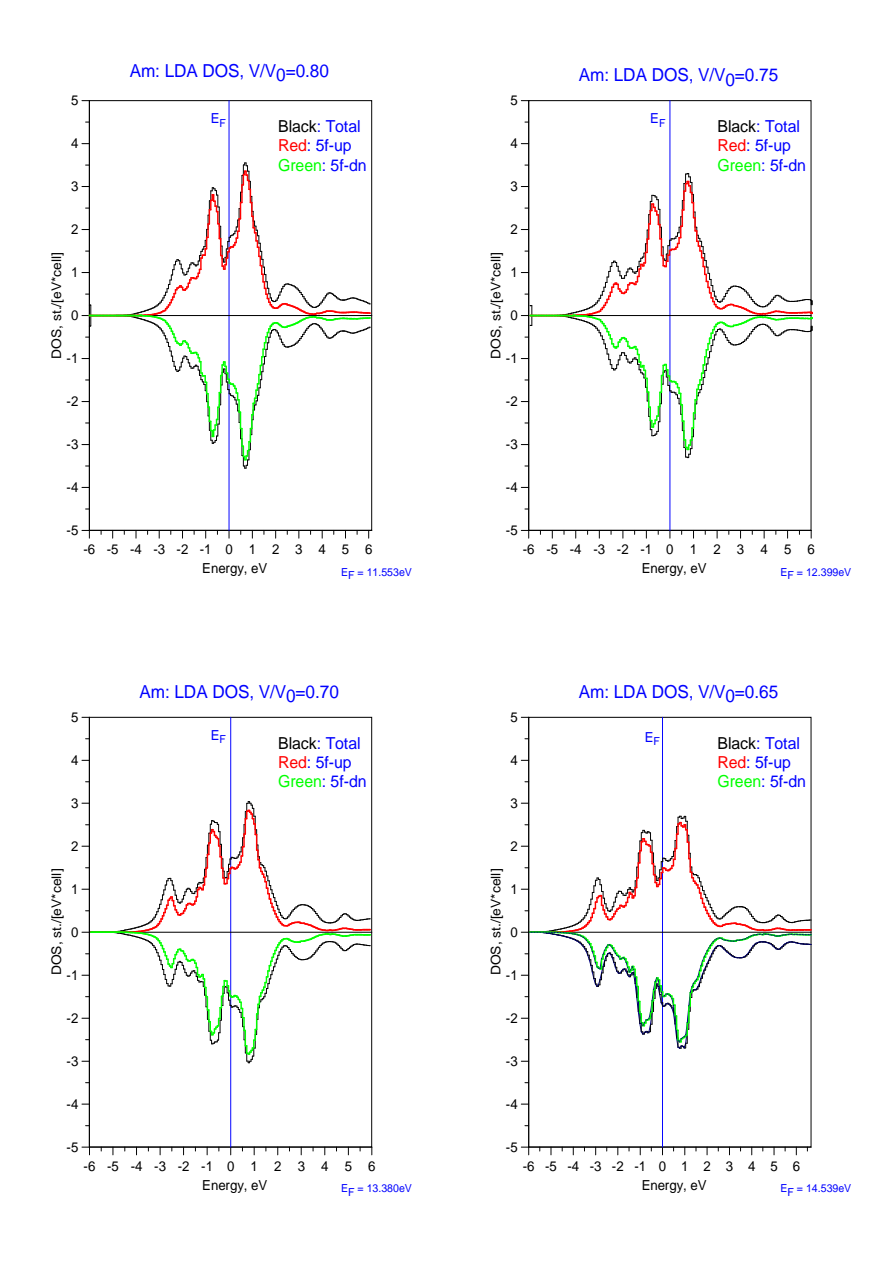


Figure 5.26: Am DOS in LDA

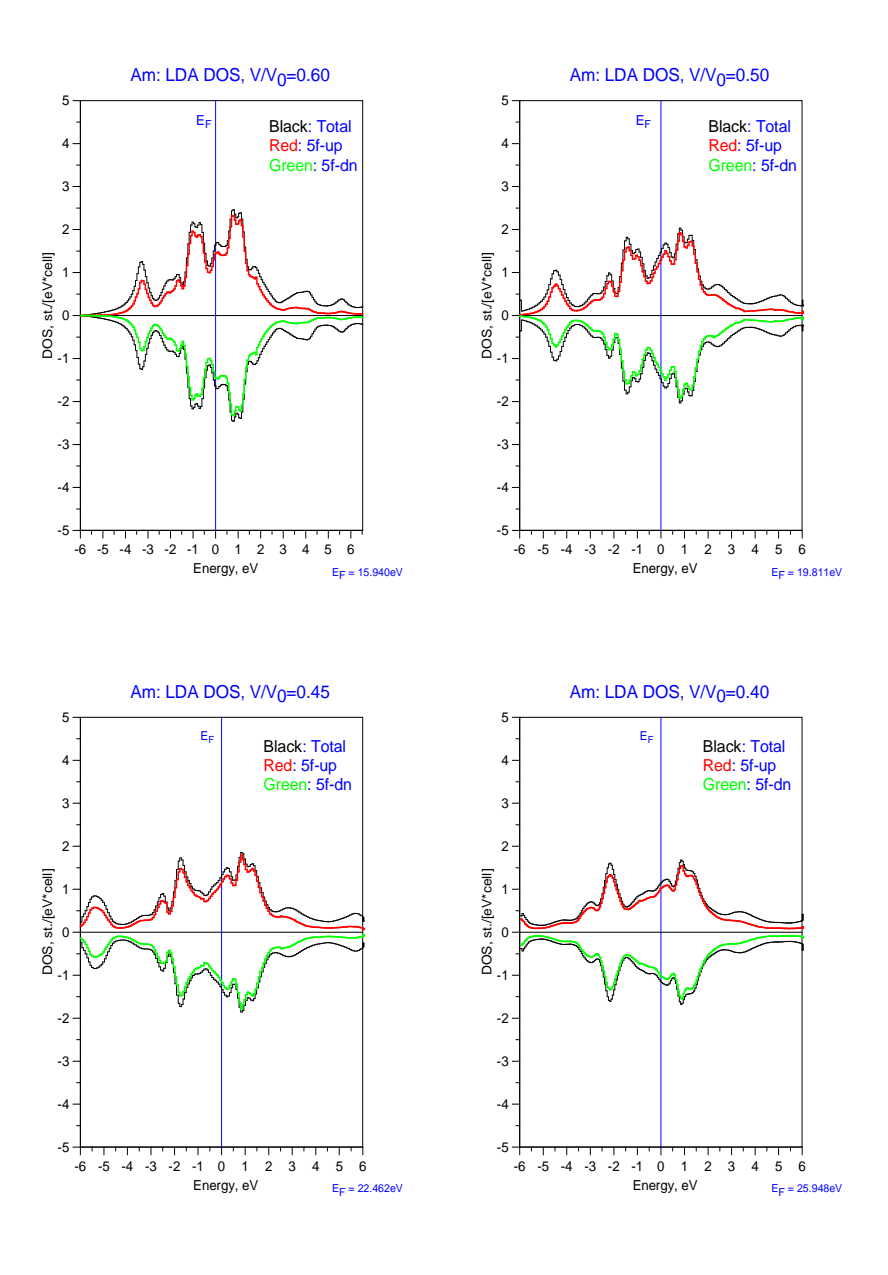


Figure 5.27: Am DOS in LDA

level. In order to fix the 5f-peak at its experimental value, we use the interaction in the double counting term \bar{U} , or U_{DC} as a parameter. Fig. 5.28 shows the evolution of the DOS with pressure at U=4.5eV when U_{DC} is kept at the same value as U. It turns out that to have the 5f-peak at its experimental value of 2.8eV below the Fermi level, we need U_{DC} to have a value slightly less than U, namely, $U_{DC}=4.1eV$. In Fig. 5.31 we see how the DOS evolves with pressure for the parameters U=4.5eV and $U_{DC}=4.1eV$.

At the equilibrium volume $V/V_0 = 1.00$, we see two Hubbard bands separated by an energy difference that accounts for U as well as spin-orbit coupling. The filled 5f-band below the Fermi level has 6 electrons and the unoccupied band above the Fermi level contains 8 electrons.

We have plotted the total density of states as well as the 5f density of states. We can see that under pressure the highly localized 5f-bands start widening and merging into each other. When $V/V_0=1.00$ we see that the 5f states do not contribute much at the Fermi level. Most of the weight at low pressures is due to the s,p and d electrons, shown in grey in the figure. As the pressure is increased, the ratio of 5f states to the total DOS near the Fermi level increases. Near $V/V_0=0.75$ we observe a spreading out of the DOS that signals a transition to a metallic state. Since the Hubbard-1 approximation essentially starts with an atomic solution, it always predicts the existence of two Hubbard bands for an arbitrarily small U. It fails to predict a sharp quasiparticle peak for a metallic state. However we do see a finite and increasing but wide distribution of states at the Fermi level as we increase pressure. In Fig. 5.34 we see the total and partial 5f-density of states at the Fermi energy, and in Fig. 5.35 we see the ratio between the 5f-DOS and the total DOS plotted as a function of the relative volume.

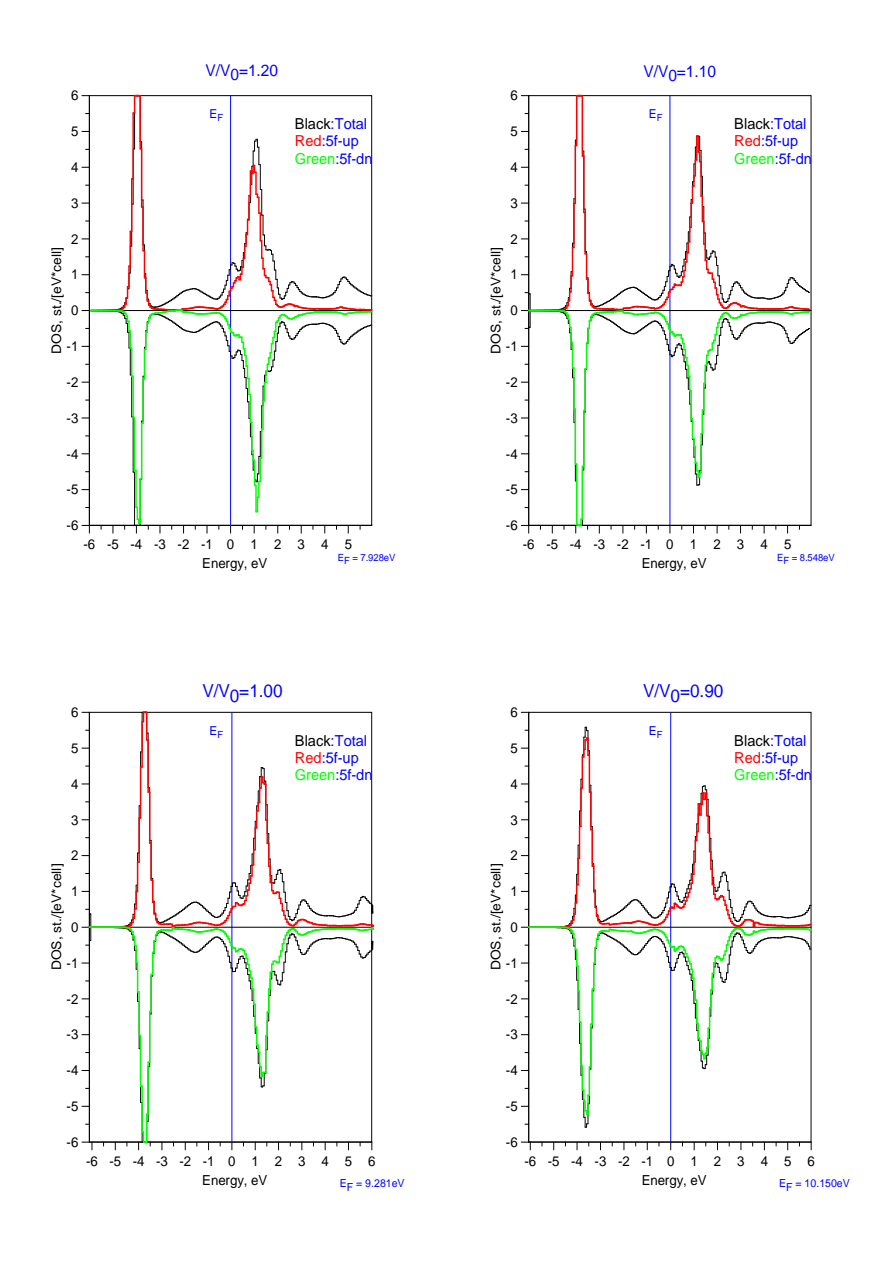


Figure 5.28: Am DOS in LDA+DMFT: $U=U_{DC}=4.5eV$

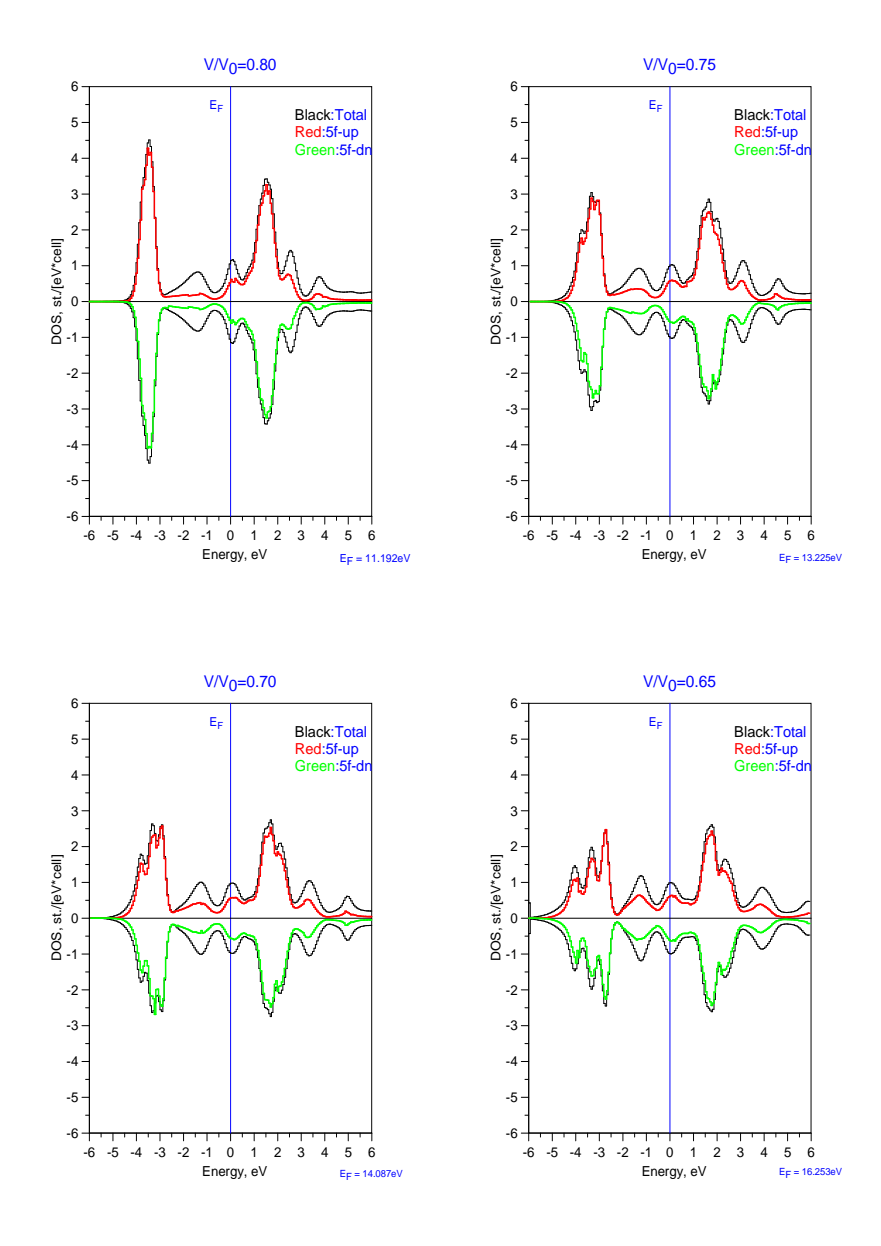


Figure 5.29: Am DOS in LDA+DMFT: $U=U_{DC}=4.5eV$

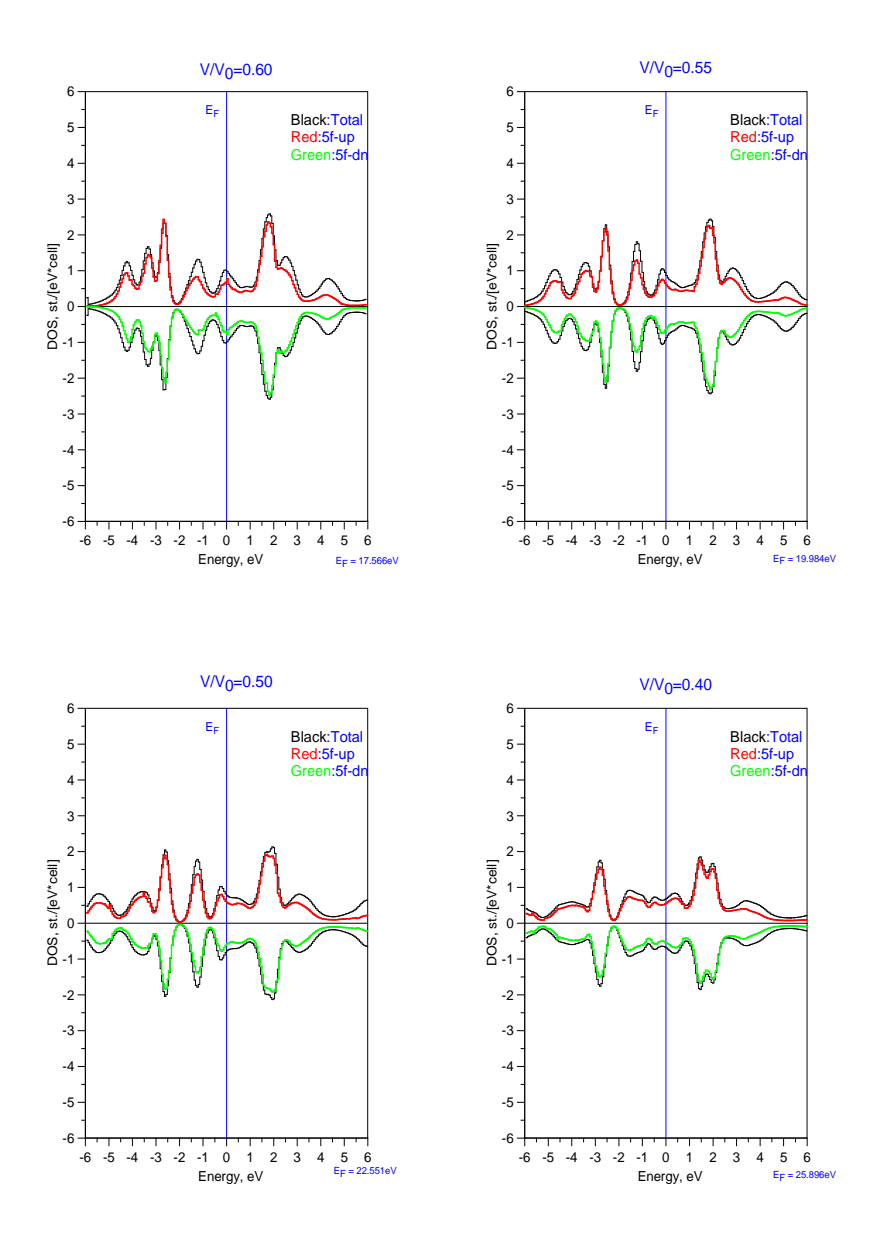


Figure 5.30: Am DOS in LDA+DMFT: $U=U_{DC}=4.5eV$

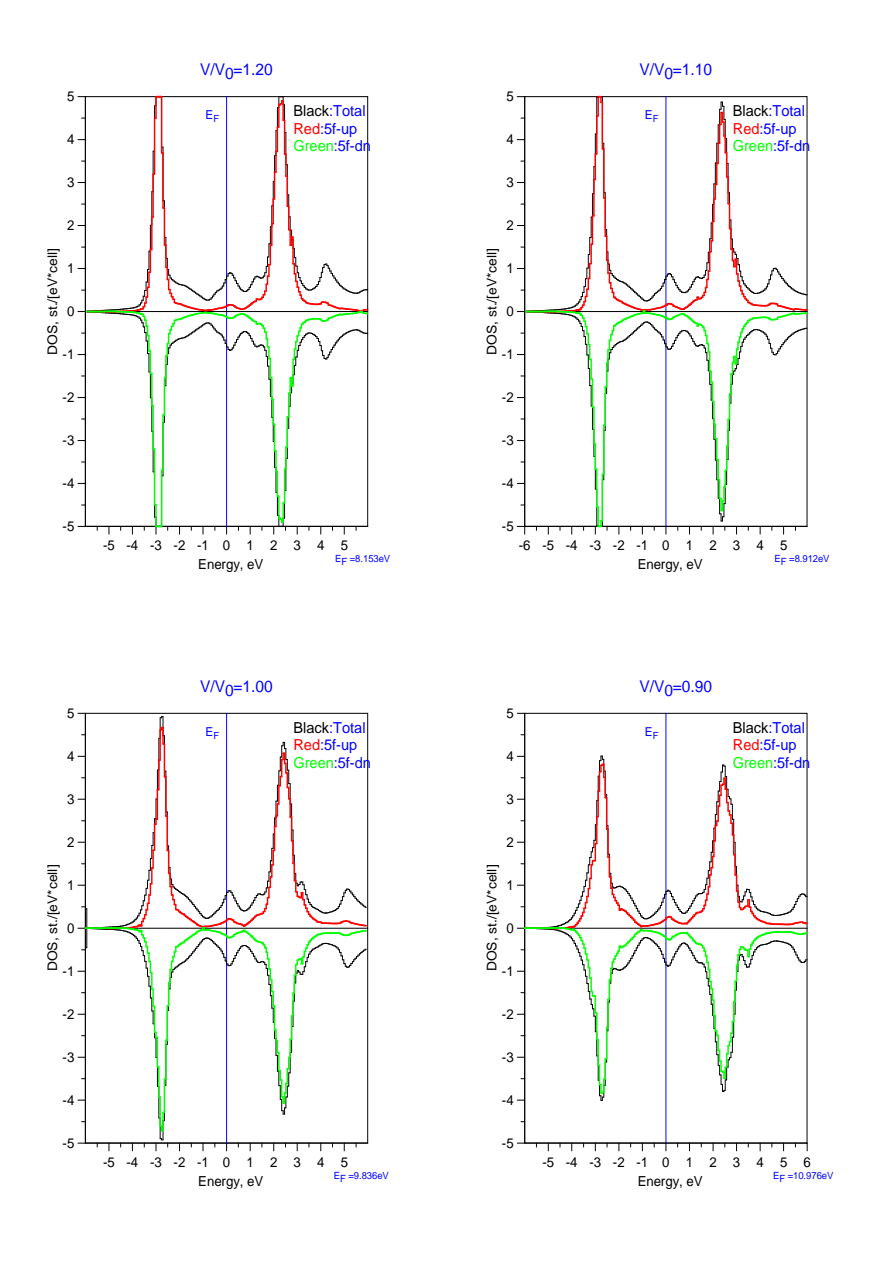


Figure 5.31: Am DOS in LDA+DMFT: $U=4.5eV, U_{DC}=4.1eV$

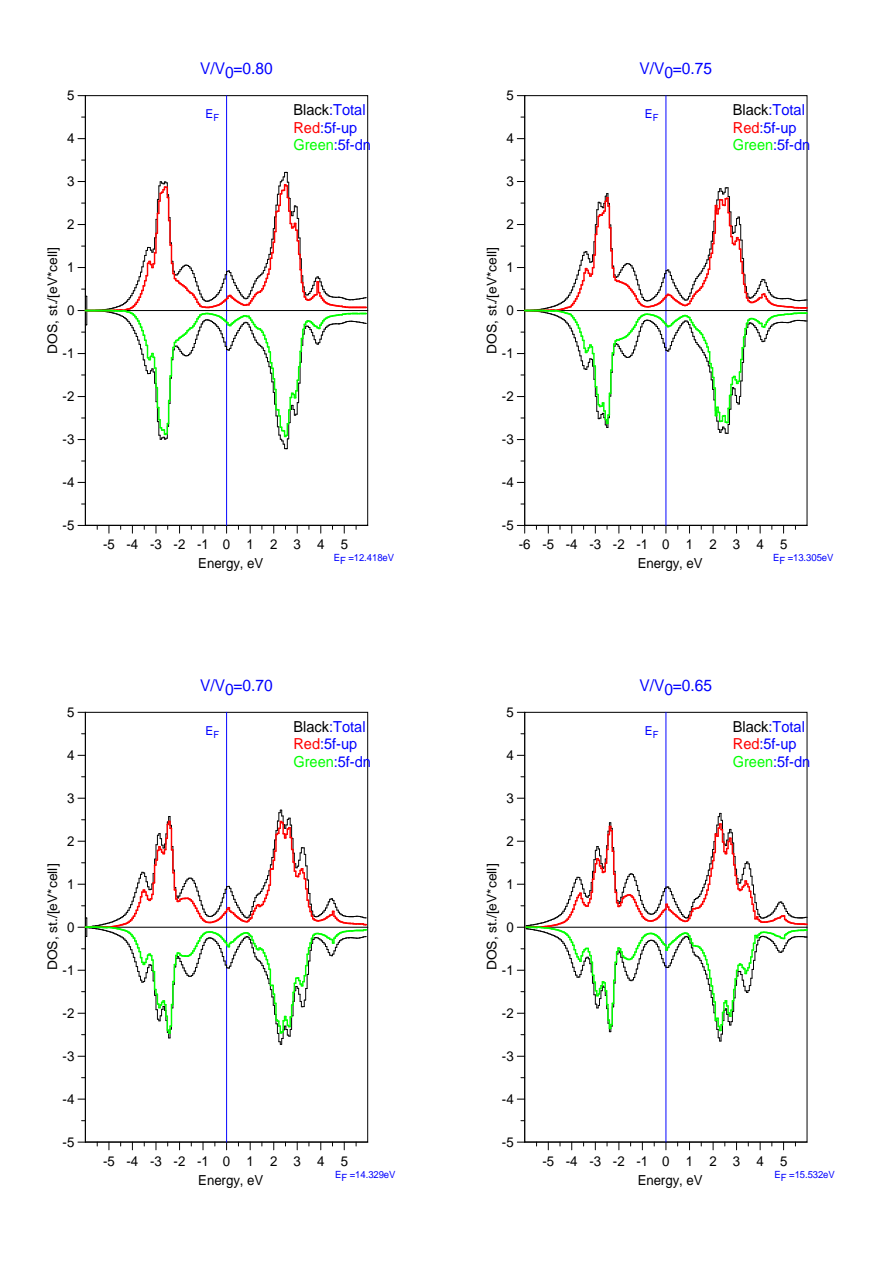


Figure 5.32: Am DOS in LDA+DMFT: $U=4.5eV, U_{DC}=4.1eV$

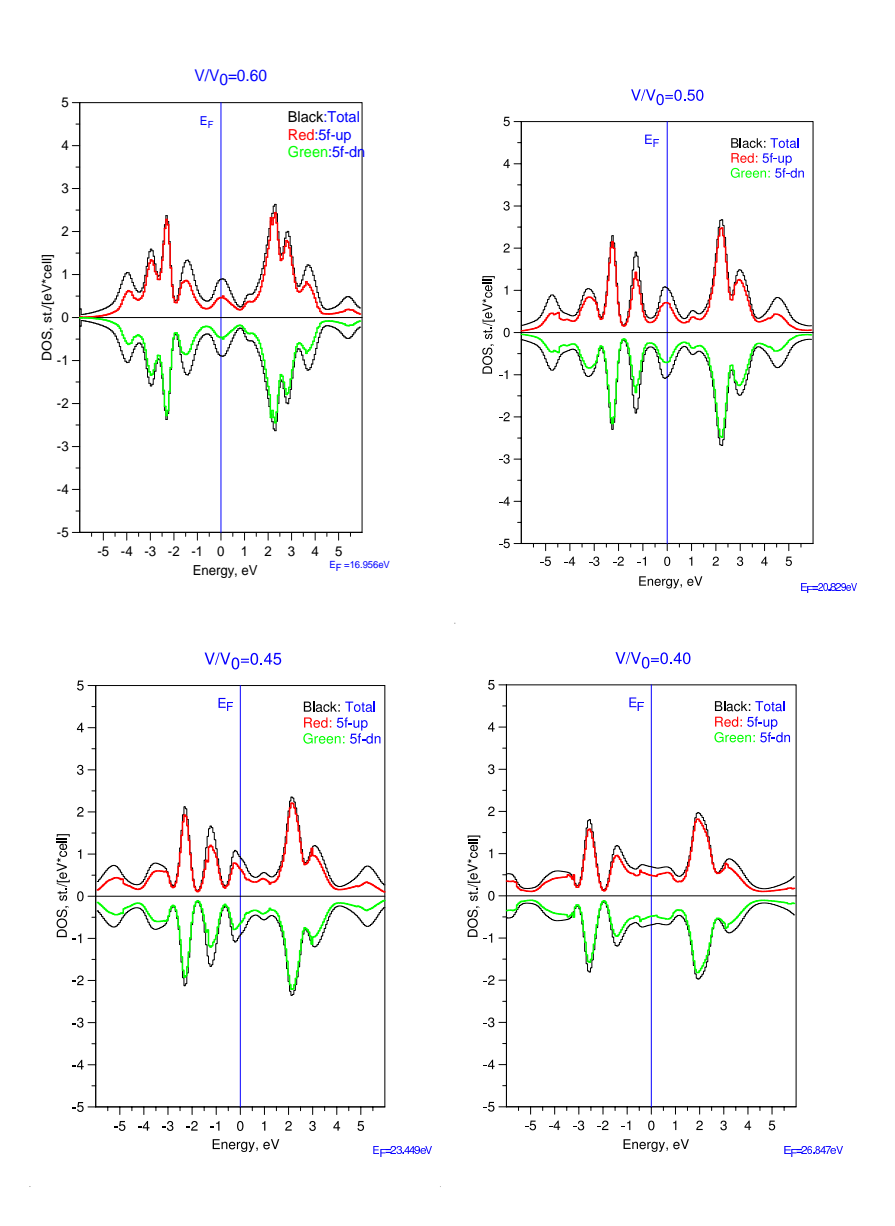


Figure 5.33: Am DOS in LDA+DMFT: $U=4.5eV, U_{DC}=4.1eV$

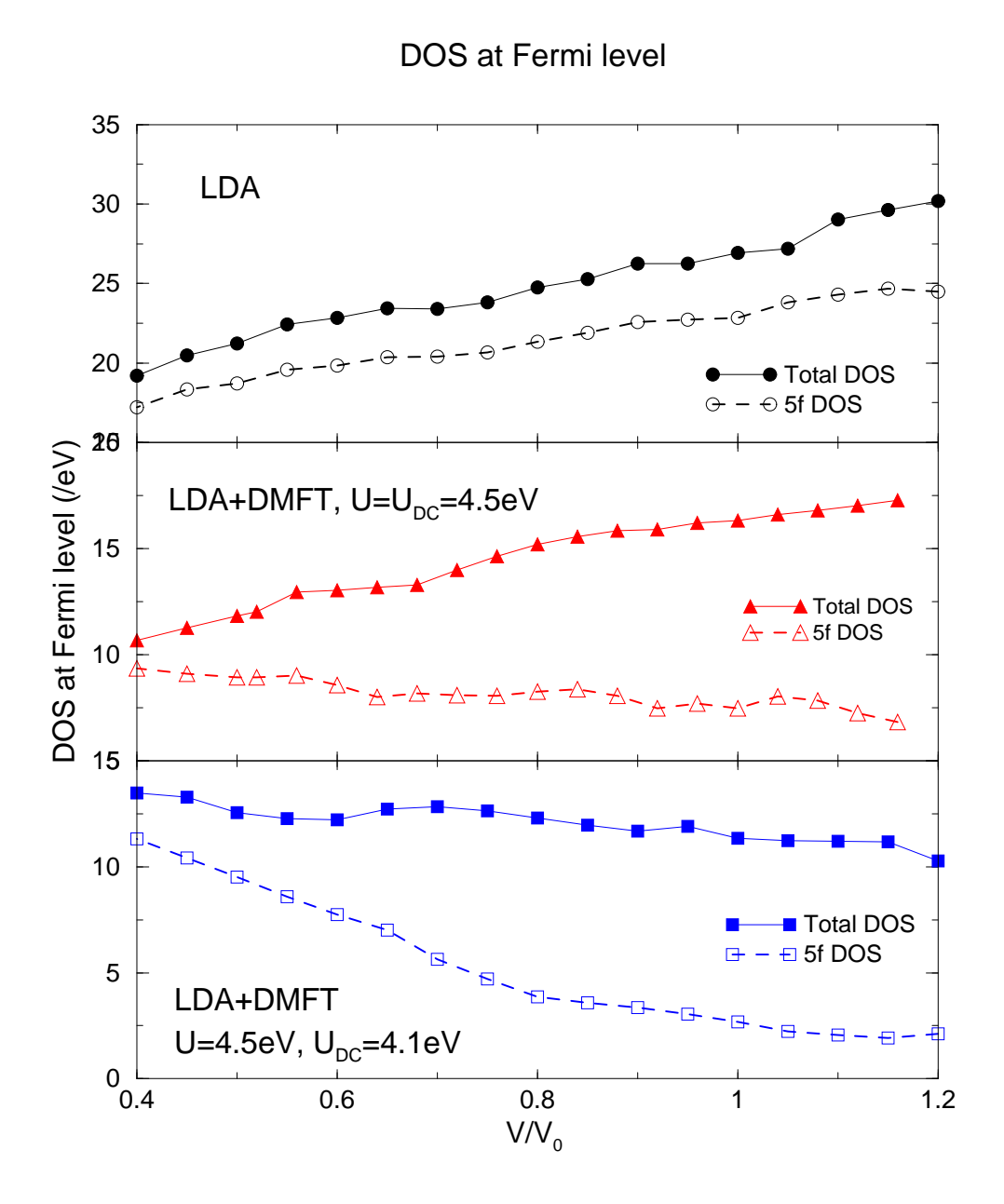


Figure 5.34: Density of states at Fermi level in LDA and LDA+DMFT

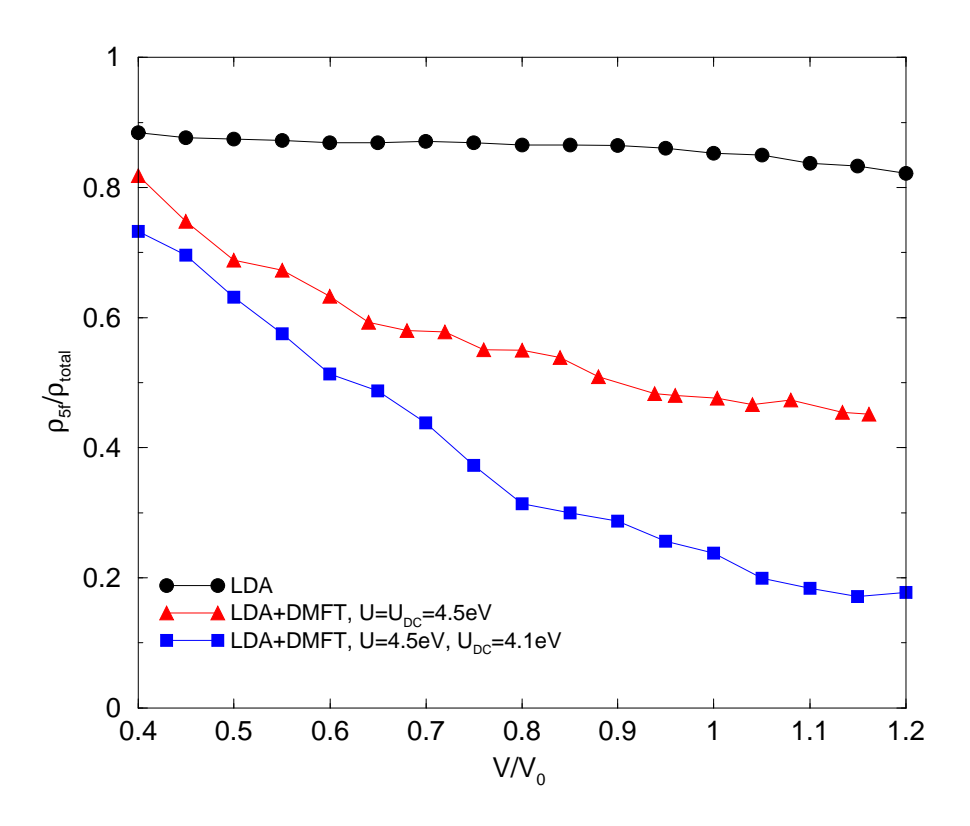


Figure 5.35: Ratio of 5f-DOS over total DOS

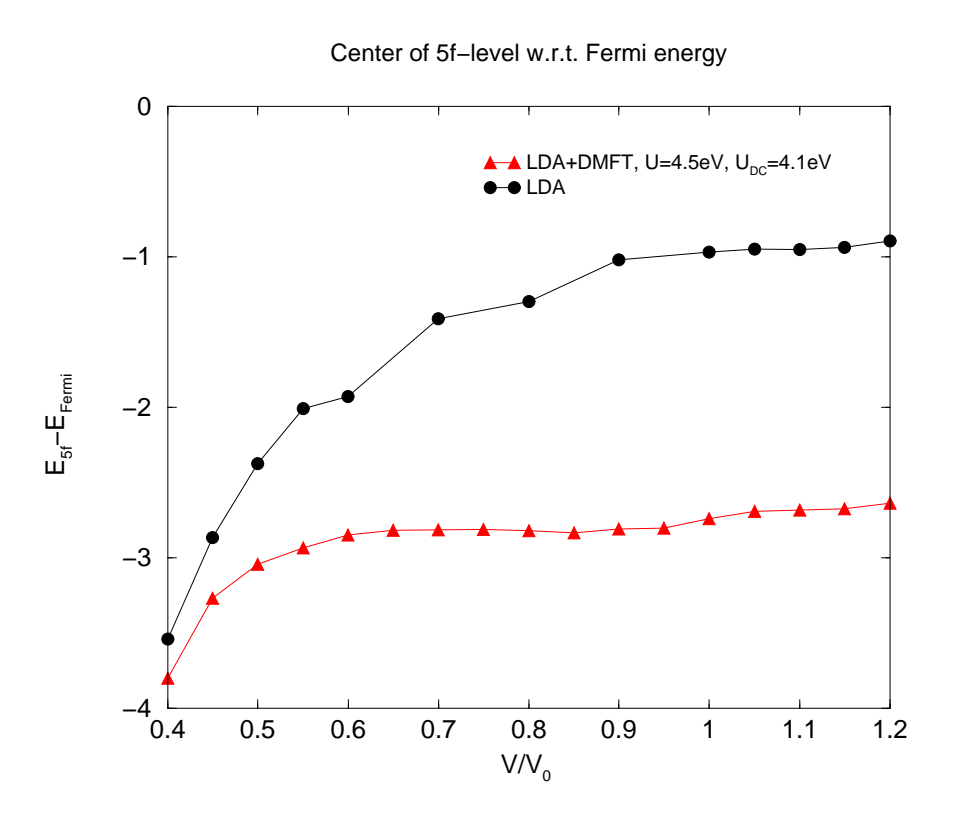


Figure 5.36: Position of center of 5f-band

5.4 Summary and Conclusions

We have calculated the electronic band structure of Americium using the LDA+U method and the LDA+DMFT methods. The LDA+U method gives consistent results with photoemission spectra and equilibrium volume of Am. However we fail to get the correct magnetic moment in Americium using LDA+U. Americium is in a J=0 non-magnetic ground state due to spin-orbit coupling. However, the LDA+U computation predicts a half-filled shell and a magnetic moment of $7 \mu_B$.

We then use the LDA+DMFT method to compute the structure and volume of Am. We can correctly predict the position of the 5f-peak as well as the correct equilibrium volume of Am. On applying pressure, we observe a hysteresis loop in the energy-volume curve which strongly indicates the proximity to a Mott transition.

Chapter 6

Summary and conclusions

In this thesis we have numerically studied aspects of the Mott transition in model Hamiltonians as well as in real materials.

In chapter 2, we introduced the idea of the Mott transition, that is, a first order metal-insulator transition driven by electron correlations. We applied the dynamical mean-field theory (DMFT) to study a simple model Hamiltonian: the degenerate Hubbard model. Based on numerical calculations of the behavior of the particle occupation number as a function of doping, we mapped out the phase diagram of the Hubbard model in the paramagnetic regime. We found a region of coexistence between metallic and insulating phases at finite temperatures. Furthermore, we showed that at small but finite doping, the compressibility diverges at the Mott endpoint. Our model calculations were found to be relevant to the α - γ transition in Ce.

We briefly shifted gears in chapter 3 and gave an overview of various density functional methods, which are first-principles methods in the sense that no empirical parameters (other than atomic charges and lattice structure) are needed to predict physical properties of materials. Density functional theory in the local density approximation (LDA) has had considerable success in understanding electronic structure of weakly interacting solids. We then moved on to describe methods that go beyond LDA, in order to deal with strongly correlated materials. We focused on two such methods: LDA+U, where U is the Coulomb interaction, and the LDA+DMFT which uses LDA to describe the light s, p (or s, p, d) electrons and DMFT to treat correlated d and f electrons.

Chapters 4 and 5 contain applications of the two theoretical approaches we discussed so far: a many body Hamiltonian approach combined with first-principles calculations.

We used these techniques to study the electronic structure and properties of two materials that have strong correlations due to f-band electrons.

In chapter 4, we investigated YbRh₂Si₂, a heavy fermion compound that exhibits many deviations from Fermi liquid behavior due to interactions between the localized 4f—electrons in the Yb³⁺ ion and the conduction band formed by the s,p and d electrons. We used the LDA+U technique to determine the electronic structure and magnetic properties of YbRh₂Si₂. In the process, we did a careful study of the so-called double-counting term, that is, the energy that needs to be subtracted from the LDA+U functional, since part of the correlation energy is already present in the LDA functional. As the double-counting term was too large in the standard LDA+U functional, we failed to obtain the correct magnetic ground state of YbRh₂Si₂. We presented a prescription to rectify the situation: we used the interaction U_{dc} in the double counting term as a different parameter compared to the interaction U in the LDA+U functional. Keeping U_{dc} slightly smaller than U predicted the correct band structure and magnetic moment of YbRh₂Si₂. We also successfully calculated the magnetic anisotropy energy in this material, which is very large.

In chapter 5, we returned to the idea of the Mott transition. We used LDA+U and LDA+DMFT methods to examine the delocalization-localization transition of 5f electrons in elemental Americium. This material, which borders Plutonium in the periodic table, has been the subject of a number of theoretical and experimental investigations. We put into practice the insights we gained from chapter 4 regarding the double counting term to correctly predict the photo-emission spectra. The LDA+U calculation predicted the correct equilibrium volume but not the correct magnetic moment. We then applied the LDA+DMFT technique, using the Hubbard-1 method as the impurity solver for the DMFT loop. We obtained strong evidence for the existence of a Mott transition without a large volume collapse.

Outlook

The Mott transition in Americium can be better understood if we use different structures for the different phases. In our calculations we used an impurity solver that is computationally fast, but the price we paid is perhaps an oversimplification of the physical picture. The Quantum Monte Carlo method, that we studied in chapter 2, is exact, but expensive in terms of computation time. A better impurity solver that is also fast is required in order to investigate complex materials. In addition, a first principles approach to determine the interaction parameters and the double-counting corrections will complete the picture of ab-inito many body calculations.

References

- [1] N. F. Mott. Metal-Insulator Transitions, Taylor and Francis (1974).
- [2] D. B. McWhan, J. P. Remeika, T. M. Rice, W. F. Brinkman, J. P. Maita and A. Menth. Phys. Rev. Lett., 27, 941 (1971).
- [3] For a review see M. Imada, A. Fujimori, and Y. Tokura. Rev. Mod. Phys. **70**, 1039 (1998).
- [4] S. Lefebvre, P. Wzietek, S. Brown, C. Bourbonnais, D. Jrome, C. Mzire, M. Fourmigu, and P. Batail. Phys. Rev. Lett., 85, 5420-5423 (2000).
- [5] For a review see A. Georges, G. Kotliar, W. Krauth, and M. J. Rozenberg. Rev. Mod. Phys. 68, 13 (1996).
- [6] G. Kotliar, E. Lange and M. J. Rozenberg. Phys. Rev. Lett. 84, 5180 (2000).
- [7] M. J. Rozenberg, G. Kotliar and H. Kajueter. Phys. Rev. B 54, 8452 (1996).
- [8] P. Hohenberg and W. Kohn. Phys. Rev. **136**, 864 (1964).
- [9] W. Kohn and L. J. Sham. Phys. Rev. **140**, 1133 (1965).
- [10] See, for example, J. P. Perdew, K. Burke and M. Ernzerhof. Phys. Rev. Lett. 77, 3865 (1996) and references therein.
- [11] For a review, see Strong Coulomb correlations in electronic structure calculations, edited by V. I. Anisimov, Advances in Condensed Material Science (Gordon and Breach, 2001).
- [12] A. I. Lichtenstein and M. Katsnelson. Phys. Rev. B 57 6884 (1998).
- [13] R. Chitra and G. Kotliar. Phys. Rev. B, 62, 12715 (2000).
- [14] For a review, see V. I. Anisimov, F. Aryasetiawan and A. I. Lichtenstein. J. Phys.:Condensed Matter 9, 767 (1997).
- [15] V. I. Anisimov, J. Zaanen and O. K. Andersen. Phys. Rev. B 44, 943 (1991).
- [16] A. I. Lichtenstein, J. Zaanen and V. I. Anisimov. Phys. Rev. B 52, R5467 (1995).
- [17] Imseok Yang, Ph.D. thesis, Rutgers University, 2001.
- [18] S. Biermann, F. Aryasetiawan and A. Georges. Phys. Rev. Lett., **90**, 086402 (2003).
- [19] P. Sun and G. Kotliar. Phys. rev. B, 66, 085120 (2002).
- [20] S. Savrasov, G. Kotliar, and E. Abrahams, Nature 410, 793 (2001).

- [21] K. Held, A. K. McMahan, and R. T. Scalettar. Phys. Rev. Lett. 87, 276404 (2001).
- [22] M. B. Zölfl, I. A. Nekrasov, Th. Pruschke, V. I. Anisimov, and J. Keller. Phys. Rev. Lett. 87, 276403 (2001).
- [23] M. B. Zölfl, Th. Pruschke, J. Keller, A. I. Poteryaev, I. A. Nekrasov, and V. I. Anisimov. Phys. Rev. B **61**, 12810 (2000).
- [24] V. Oudovenko, G.Pálsson, G. Kotliar and S. Y. Savrasov. xxx.lanl.org/abs/cond-mat/0209336.
- [25] K. Held, G. Keller, V. Eyert, D. Vollhardt, and V. I. Anisimov Phys. Rev. Lett. 86, 5345-5348 (2001)
- [26] A. Matsuura, Z. X. Shen, D. S. Dessau, C. H. Park, T. Thio, J. W. Bennet and O. Jepsen. Phys.. Rev. B, 53, R7584 (1996).
- [27] K. Kanoda. Physica (Amsterdam) **282-287C** (1997).
- [28] D. Fournier, M. Poirier, M. Castonguay and K. D. Truong. Phys. Rev. Lett., 90, 127002 (2003).
- [29] B.Johansson. Phil. Mag. **30**, 469 (1974).
- [30] R.I.Beecoft and C.A.Swenson. J. Phys. Chem. Solids, 15, 234 (1960).
- [31] J. Hubbard. Proc. Roy. Soc. London A, **276**, 238 (1963).
- [32] W. F. Brinkman and T. M. Rice. Phys. Rev. B, 2, 4302 (1970).
- [33] A.Georges and W.Krauth. Phys. Rev. B, 48, 7167 (1993).
- [34] M. J. Rozenberg, G. Kotliar, and X. Y. Zhang. Phys. Rev. B, 49, 10181 (1994).
- [35] M. J. Rozenberg, R. Chitra, and G. Kotliar. Phys. Rev. Lett., 83, 3498 (1999).
- [36] Daniel Fisher, G. Kotliar and G. Moeller. Phys. Rev. B. **52**, 17112 (1995).
- [37] N. Furukawa and M. Imada. J. Phys. Soc. Jpn. **60**, 3604 (1991).
- [38] M. Kohno. Phys. Rev. B **55**, 1435 (1997).
- [39] M. C. Gutzwiller. Phys. Rev., **137**, A1726 (1965).
- [40] W. Metzner and D. Vollhardt. Phys. Rev. Lett., **62**, 324 (1989).
- [41] J. E. Hirsch and R. M. Fye. Phys. Rev. Lett. **56**, 2521 (1986).
- [42] K. Takegahara. Journal of the Physical Society of Japan, 62, 1736 (1993).
- [43] Jaewook Joo and Viktor Oudovenko. Phys. Rev. B 64, 193102 (2001).
- [44] G. Kotliar, S. Murthy and M. J. Rozenberg. Phys. Rev. Lett., 89, 046401 (2002).
- [45] G. Moeller. Ph.D thesis, Rutgers University, 1994.
- [46] G. Kotliar. Eur. Jour. Phys. B, 11, 27 (1999).

- [47] G. Kotliar and S. Y. Savrasov. New Thoeretical Approaches to Strongly Correlated Systems, Kluwer Academic Publishers, 259 (2001).
- [48] R. Chitra and G. Kotliar. Phys. Rev. B, 63, 115110 (2001).
- [49] S. Y. Savrasov, G. Kotliar and D. Villani. unpublished.
- [50] Xi Dai. Private communication.
- [51] O. K. Andersen. Phys. Rev. B 12, 3060 (1975).
- [52] For a review, see, e.g., Theory of the Inhomogeneous Electron Gas, edited by S. Lundqvist and S. H. March. Plenum, New York (1983).
- [53] O. Trovarelli, C. Geibel, S. Mederle, C. Langhammer, F. M. Grosche, P. Gegenwart, M. Lang, G. Sparn, and F. Steglich. Phys. Rev. Lett. 85, 626 (2000).
- [54] A. G. Petukhov, I. I. Mazin, L. Chioncel, and A. I. Lichtenstein Phys. Rev. B 67, 153106 (2003).
- [55] M. T. Czyzyk and G. A. Sawatzky. Phys. Rev. B, 49, 14211 (1994).
- [56] D. Rossi, R. Marazza, R. Ferro. J. Less-Common Met., 66, 17 (1979).
- [57] Program *LmtART* developed by S. Savrasov.
- [58] O. Trovarelli, C. Geibel, C. Langhammer, S. Mederle, P. Gegenwart, F. Grosche, M. Lang, G. Sparn, F. Steglich. Physica B, 281&282, 372 (2000).
- [59] O.Trovarelli, C. Geibel, F. Steglich. Physica B, 284-288, 1507 (2000).
- [60] J. R. Naegele, L. Manes, J. C. Spirlet, and W. Muller. Phys. Rev. Lett. 52, 1834 (1984).
- [61] S. Heathman, A. Lindbaum, K. Litfin, Y. Meresse, R. G. Haire, T. Le Bihan, and H. Libotte. Phys. Rev. Lett. 85, 2961 (2000).
- [62] A. Lindbaum, S. Heathman, K. Litfin, Y. Meresse, R. G. Haire, T. Le Bihan, and H. Libotte. Phys. Rev. B 63, 214101 (2001).
- [63] U. Benedict, J. P. Itie, C. Dufour, S. Dubos and J. C. Spirlet. Americium and Curium Chemistry and Technology, published by Reidel, Dordrecht (1985), pp. 221.
- [64] O. Eriksson and J. M. Wills. Phys. Rev. B 45, 3198 (1992).
- [65] P. Soderlind, R. Ahuja, O. Eriksson, B. Johansson and J. M. Wills. Phys. Rev. B 61, 8119 (2000).
- [66] M.Pénicaud. J. Phys.:Condens. Matter 14, 3575 (2002).
- [67] Handbook of the Physics and Chemistry of Actinides, edited by A. J. Freeman and G. H. Lander. Elselvier Science Pub. Co. 1984.
- [68] Jeffrey L. Tilson, Conrad Naleway, Michael Seth, Ron Shepard, Albert F. Wagner, and Walter C. Ermler. Journal of Chem. Phys. 116, 5333 (2002).

- [69] N. Martensson, B. Johansson and J. R. Naegele. Phys. Rev. B, 35, 1437 (1987).
- [70] U. Benedict. J. Phys. Colloq. C-8, 145 (1984).
- [71] P. Wachter, M. Flizmoser, J. Rebizant. Physica B 293, 199 (2001).

Vita

Sahana Murthy

1992-1995	Bachelor of Science. University of Mumbai, Mumbai, India.
1995-1997	Master of Science, Physics. Indian Institue of Technology, Mumbai, India. Thesis advisor: Professor Dipan Ghosh.
1997-present	Graduate study, Dept. of Physics, Rutgers University, New Jersey.
2004	Ph.D. in Physics, Rutgers University, New Jersey. Thesis written under the direction of Professor Gabriel Kotliar.
1997	C. Y. Kadolkar, N. Goveas, D. K. Ghosh, S. Murthy. Haldane gap in S=2 XXZ quantum antiferromagnet. [Conference Paper] Elsevier. Journal of Magnetism and Magnetic Materials, 177-181, part 1, 638 (1998).
2002	Compressibility divergence and the finite temperature Mott transition. G. Kotliar, S. Murthy, M. J. Rozenberg. Phys. Rev. Lett. 89 , 046401 (2002).